The Impact of Peculiar Velocities on Supernova Cosmology

Bryony Martin

November 2011

A project submitted in partial fulfillment of the requirements for the degree M.Sc. in the Department of Astronomy, as part of the National Astrophysics and Space Science Programme
UNIVERSITY OF CAPE TOWN

Supervisors: Dr. Kurt van der Heyden and Prof. Bruce Bassett

Abstract

We investigate the impact of correlated peculiar velocities on the accuracy of the estimated cosmological parameters calculated using type Ia supernovae.

We use mock galaxy catalogues constructed from the Millennium Simulation, the largest dark matter N-body simulation run to date. Supernovae are assigned to the galaxies in the mock survey data according to supernova rates that define the probability of a supernova occurring in a given time. The rates are based on the physical properties of the galaxies, in particular their colour, which is linked to the rate of star formation, and their mass. The peculiar velocities of each galaxy are provided and we assume that the supernovae have the same peculiar velocities as their host galaxies. Therefore, each supernova has a true cosmological redshift, and an observed redshift which is the redshift measured by an observer and is subject to contamination by radial peculiar velocities.

We find that the correlations between the peculiar velocities can be reduced by combining observational data from different survey fields that have large angular separations.

Using CosmoMC, the cosmological parameters are estimated, with the Markov-Chain Monte Carlo technique, from the simulated supernova data, firstly using the true cosmological redshifts, and subsequently, using the observed redshifts. We compare the estimated values of the parameters Ω_m and H_0 that are obtained with the two different redshifts to get a measure of the inaccuracies caused by correlated peculiar velocities. Our results provide upper bounds on the effect.

The results suggest that a minimum redshift cut at $z = 0.05$ is the most effective at reducing the effects of the correlated peculiar velocities without compromising the accuracy of the parameter estimation.

In general, the shifts in parameter estimates due to correlations in the peculiar velocities are around 1σ or less, with H_0 slightly more biased than Ω_m. In specific cases, where only low redshift data is used (and therefore, which are not very relevant to reality) the shift can be up to 3σ. Since H_0 is determined by low redshift data, it is not surprising that it is more affected by the correlations which occur primarily at low redshift. Combining the 1σ shift with standard sample variance means that, in general, peculiar velocity correlations

can cause a shift in the recovered cosmological parameters of up to 2σ. This suggests that future surveys will have to take these correlations into account to ensure unbiased parameter estimates.

Acknowledgements

I would like to thank my supervisors Dr. Kurt van der Heyden and Prof. Bruce Bassett for their guidance and support throughout this project. Thanks, also, to the members of the University of Cape Town (UCT) Astronomy Department and the Cosmology Group at the African Institute for Mathematical Sciences Research Centre for their support.

Thanks to Dr. Andreas Faltenbacher for his assistance and to my fellow Masters students at UCT, particularly Kosma von Maltitz for the numerous afternoon tea breaks. A special thank you to Dr. Mathew Smith for his advice, assistance and encouragement.

The Millennium Simulation databases used in this work, and the web application providing online access to them, were constructed as part of the activities of the German Astrophysical Virtual Observatory.

I gratefully acknowledge the funding provided by SKA South Africa, the South African National Research Foundation (NRF) and the National Astrophysics and Space Science Programme (NASSP).

Plagiarism Declaration

I, Bryony Martin, know the meaning of plagiarism and declare that all of the work in this document, save for that which is properly acknowledged, is my own.

Contents

List of Figures

List of Tables

Chapter 1

Introduction

Cosmologists use type Ia supernovae as tools for studying the Universe. The peculiar velocities of galaxies affect the accuracy of supernovae observations and therefore impact the results determined by supernova cosmology. As we move towards precision cosmology, and with future surveys expecting to discover thousands more supernovae, understanding this effect will become increasingly important.

This chapter provides the background information necessary for investigating the effect of peculiar velocities on cosmological studies using type Ia supernovae. It includes explanations of the standard cosmological model, inhomogeneous cosmology, peculiar velocities, definitions of distance measures, supernovae and supernova cosmology.

1.1 Cosmology

The study of cosmology is concerned with understanding and explaining the properties of the Universe as a whole. We try to describe the contents, shape and behaviour of the Universe using theory, observations and a number of parameters that represent its components or states. This includes how the Universe began and how it might end. The standard model of cosmology, as described below, is an excellent description of our observations of the Universe. It is this model which underlies the data used in this work and the assumptions made during analysis.

1.1.1 The Standard Model of Cosmology

The standard model is built on Einstein's theory of General Relativity and the Cosmological Principle. General Relativity describes the dynamics of matter and radiation in the presence of gravity. The Cosmological Principle states that, on sufficiently large scales, the Universe is homogeneous and isotropic. This means that the Universe is the same everywhere and there are no special, or preferred places.

We know from observing the recession velocities of galaxies that the Universe is not

static, but is continuously expanding. Initially, the Universe was in a hot, dense state where its contents were dominated by thermal blackbody radiation and baryons (matter) were coupled to photons (radiation). The Big Bang marks the start of expansion which resulted in the contents of the Universe cooling down. Approximately 400,000 years after the Big Bang the Universe had cooled sufficiently for photons to decouple from matter at what we call the surface of last scattering. The signal from this last scattering surface is the Cosmic Microwave Background (CMB) which we detect today. The temperature of the CMB signal is the same across the entire sky to within 1 part in 10^5 which is evidence of the Universe's isotropy.

The expansion of the Universe is critical to all cosmological theories and models. We define the rate of expansion using Hubble's constant H. H is not actually constant but varies with time. We denote the value of the Hubble constant today by H_0. We can then define the rate of the increase today in the distance l between any two points to be

$$\frac{dl}{dt} = H_0 l \tag{1.1}$$

A recent estimate of the Hubble constant is $H_0 = 70.5 \pm 1.3$ which was derived using the 5 year data from the Wilkinson Microwave Anisotropy Probe (WMAP) combined with baryon acoustic oscillation and high redshift supernova data and assuming the standard model with a cosmological constant Λ and cold dark matter (see Komatsu et al. (2009) where the WMAP experiment is explained fully and the cosmological parameters are derived). H_0 is commonly expressed using the dimensionless quantity h where $h = H_0/100\text{kms}^{-1}\text{Mpc}^{-1}$.

The comoving separation between two objects takes into account the Hubble expansion. That is, the comoving separation is constant under expansion although the distance between the objects increases with time. At low redshift Hubble's Law relates this comoving separation r to the apparent recession velocity v. The recession velocity is the velocity at which an object appears to be moving away from an observer due to expansion. Hubble's Law is:

$$v = Hr \tag{1.2}$$

The scale factor $a(t)$, is a dimensionless quantity that represents the expansion of the Universe relative to the size of the Universe today (i.e. $a_0 = 1$). It comes from the Friedmann-Lemaître-Robertson-Walker (FLRW) metric, which is an exact solution of Einstein's Field Equations of General Relativity for a homogeneous and isotropic universe (Peacock 1999). The first and second derivatives of the scale factor with respect to time are denoted by $\dot{a}$ and $\ddot{a}$, and represent the rate and acceleration of expansion. The Hubble parameter, H, can be written in terms of the scale factor as:

$$H = \frac{\dot{a}}{a} \tag{1.3}$$

The Friedmann equations are derived from the FLRW metric and the Einstein Field Equations (Weinberg 1972). They describe the acceleration (Equation 1.4) and the evolution

(Equation 1.5) of the Universe. These equations are based on the assumption that the Universe is homogeneous and isotropic and that the contents of the Universe behave as a perfect fluid with density ρ and pressure p. The Friedmann equations are:

$$H^2 \equiv \left(\frac{\dot{a}}{a}\right)^2 = \frac{8\pi G\rho}{3} - \frac{\kappa}{a^2} + \frac{\Lambda}{3} \tag{1.4}$$

$$\frac{\ddot{a}}{a} = -\frac{4\pi G}{3}(\rho + 3p) + \frac{\Lambda}{3} \tag{1.5}$$

where G is Newton's gravitational constant and Λ is the cosmological constant. For simplicity Λ can be set to zero, however, a non-zero cosmological constant is currently the most popular candidate for explaining the accelerated expansion of the universe. κ indicates the curvature of spacetime. $\kappa = 0$ represents a geometrically flat, or Euclidean, universe with zero spatial curvature. A closed universe with elliptical geometry and positive spatial curvature is represented by $\kappa = +1$, and $\kappa = -1$ indicates an open universe that is geometrically hyperbolic and has negative spatial curvature. The sign of the curvature is not affected by expansion, it is governed by matter and energy density.

The density for which the Universe is flat is known as the critical density

$$\rho_{crit} = \frac{3H^2}{8\pi G} \tag{1.6}$$

The density parameter Ω represents the ratio of the density to the critical density and thus gives a measure of curvature.

$$\Omega = \frac{\rho}{\rho_{crit}} \tag{1.7}$$

$\Omega = 1$ corresponds to a flat universe. Any deviation from unity indicates curvature: $\Omega > 1$ results in a closed universe with positive curvature and $\Omega < 1$ results in an open universe with negative curvature. Current observations are consistent with a flat universe and flatness is assumed in this work.

1.1.2 The Contents of the Universe

Although we often assume so for simplicity, the Universe is not a perfect fluid. Rather, it appears to contain a number of independent components: radiation, baryonic matter, dark matter and dark energy. The overall density ρ is the sum of the densities ρ_i for each of these components and the density parameter is defined as

$$\Omega_{total} = \Omega_m + \Omega_\gamma + \Omega_\Lambda + \Omega_k \tag{1.8}$$

where Ω_m accounts for the density of both baryonic matter and dark matter. Ω_γ is the density parameter for radiation. Ω_Λ is the contribution to density from dark energy. Ω_k is the curvature density parameter; in a flat universe, as is assumed in this work, $\Omega_k = 0$ and

therefore we use the following simplified definition of the density parameter:

$$\Omega_{total} = \Omega_m + \Omega_\gamma + \Omega_\Lambda \tag{1.9}$$

The continuity equation describes the conservation of energy in cosmology and how the density of the components of the Universe expand:

$$\dot{\rho} + 3H(\rho + p) = 0 \tag{1.10}$$

When we consider the Universe as a perfect fluid, it can be represented by an equation of state $p = w\rho$. In the simplest case where w is a constant the perfect fluid density evolves as

$$\rho(t) \propto a^{-3(1+w)} \tag{1.11}$$

Applying the continuity equation to the different components individually, we find that they do not respond in the same way to expansion.

Matter

We consider matter to be collisionless and therefore pressure p is zero. Then the matter density is inversely proportional to the expanding volume:

$$\rho_m \propto a^{-3} \tag{1.12}$$

Using the Friedmann acceleration equation (Equation 1.4), for a matter dominated universe we can write:

$$a \propto t^{2/3} \tag{1.13}$$

The matter component comprises both dark matter, which accounts for about 25% of the total universe, and baryonic matter, which is less than 5%. Baryonic matter couples via the electromagnetic and strong forces, and this includes all matter that we can see. Dark matter only interacts gravitationally, not electromagnetically and, as a result, we have thus far been unable to directly detect it. Its existence is inferred from observed gravitational effects that cannot be explained by baryonic matter such as the rotation curves of spiral galaxies. A recent estimate for the matter density parameter is $\Omega_m \simeq 0.2748 \pm 0.0151$ made up of dark matter $\Omega_{dm} \simeq 0.229 \pm 0.015$ and baryonic matter $\Omega_b \simeq 0.0458 \pm 0.0016$ (Komatsu et al. 2011).

Radiation

The radiation density expands as

$$\rho_\gamma \propto a^{-4} \tag{1.14}$$

due to the increasing volume (a^{-3}) and the decrease in temperature due to the increased volume (a^{-1}). Again using Equation 1.4, for a radiation dominated universe we get:

$$a \propto t^{1/2} \tag{1.15}$$

The radiation density is related to the temperature. Observations of the CMB are well represented by a blackbody spectrum with a temperature of approximately $2.7K$. Since $\rho_\gamma \propto T^4$ this results in a value of Ω_γ of the order of 10^{-5}. As this is insignificant compared with the matter component today it is usually ignored.

Dark Energy

The dark energy component is the name given to the cause of the accelerated expansion of the Universe. One of the leading candidates for dark energy is vacuum energy or the cosmological constant, Λ. A cosmological constant has a constant density and an equation of state parameter $w = -1$. At early times the Universe is dominated by the radiation and matter components which get diluted as the Universe expands, so that at some point the dark energy, which has a constant density that is not diluted by expansion, becomes dominant. Using the acceleration equation for a cosmological constant we get

$$a \propto e^{H_0 t} \tag{1.16}$$

which indicates that a universe dominated by dark energy will experience accelerated expansion. There are other possible explanations for dark energy such as modified gravity and quintessence, however, in this work we assume the ΛCDM model with its use of a cosmological constant. The value of Ω_Λ determined by Komatsu et al. (2011) is $\Omega_\Lambda = 0.725 \pm 0.016$.

Neglecting radiation because of its relatively insignificant contribution at late times, Equation 1.9 becomes

$$\Omega_{total} = \Omega_m + \Omega_\Lambda \tag{1.17}$$

In a flat universe $\Omega_{total} = 1$ and therefore, if we assume flatness, $\Omega_\Lambda = 1 - \Omega_m$.

The Acceleration Parameter

The acceleration parameter q is a dimensionless measure of the acceleration of cosmic expansion defined as

$$q = -\frac{\ddot{a}a}{\dot{a}^2} \tag{1.18}$$

and using the Friedmann equations (Equations 1.4 and 1.5) it can also be expressed as

$$q = \frac{\Omega_m}{2} - \Omega_\Lambda \tag{1.19}$$

This parameter is sometimes called the deceleration parameter as it was thought until recently that $\ddot{a}$ was negative, indicating decelerating expansion. However, in 1998, Perlmutter

et al. (1998) and Riess et al. (1998) reported evidence from supernova observations that the expansion is currently accelerating.

1.2 Cosmological Distances

An implication of the standard model of cosmology is that the Universe has a geometry and is expanding. The expansion history of the Universe, which is key to understanding its structure today, is encoded in the parameter H. Absolute distance measurements to observed astronomical objects at a large range of redshifts are essential for measuring H. Section 1.2.1 below defines the relevant distance measures and concepts.

1.2.1 Definitions

Redshift (z) is a consequence of the radial motion of the expansion which causes a Doppler shift in the emitted light. The shift can be measured by comparing the wavelengths at which specific spectral features appear with their known restframe wavelengths. Redshift relates directly to the ratio of the scale factor at the time the light is observed and the time it was emitted, it is a relative distance measure. It is defined as

$$1 + z = \frac{\lambda_{observed}}{\lambda_{emitted}} = \frac{a_0}{a(t)} \tag{1.20}$$

Comoving distance (d_C) is measured using a coordinate system that is subject to the Hubble expansion and thereby takes expansion into account. The comoving distance between objects moving with the Hubble flow is constant.

Angular diameter distance (d_A) gives the absolute distance to an object of a known size D based on a purely geometric relationship. It is defined as

$$d_A = \frac{D}{\theta} \tag{1.21}$$

θ is the angle subtended by D from the point of view of the observer. Unfortunately, in reality, the intrinsic size of an object is seldom known.

Similarly, the **luminosity distance** (d_L) gives the distance to an object of a known luminosity L by measuring the amount of received flux F from an object where

$$d_L = \left(\frac{L}{4\pi F}\right)^{1/2} \tag{1.22}$$

As with angular diameter distance, the challenge in using this distance measure is in identifying the intrinsic luminosity of an object.

Surface brightness, and therefore flux, decreases as $(1+z)^4$ and angular size as $(1+z)^2$ as the object recedes. This creates a distance duality between the two distance measures which is expressed as

$$d_L = (1+z)d_C = (1+z)^2 d_A \tag{1.23}$$

The luminosity distance can be written as (Clarkson et al. 2008):

$$d_L(z) = (1+z)\frac{c}{H_0\sqrt{-\Omega_k}}\sin\left(\sqrt{-\Omega_k}\int_0^z dz'\frac{H_0}{H(z')}\right) \tag{1.24}$$

where, if we assume w is constant as a function of redshift, $H(z)$ is related to the cosmological parameters by (Peebles 1993):

$$H(z) = H_0\sqrt{\Omega_m(1+z)^3 + \Omega_\gamma(1+z)^4 + \Omega_k(1+z)^2 + \Omega_\Lambda(1+z)^{3(1+w)}} \tag{1.25}$$

Substituting this and assuming a negligible contribution from the radiation component and a flat universe where $\Omega_k = 0$ and $w = -1$ as in the ΛCDM standard model, the luminosity distance formula can be written in its most common form:

$$d_L = (1+z)\frac{c}{H_0}\int_0^z \frac{dz'}{[\Omega_m(1+z')^3 + \Omega_\Lambda]^{1/2}} \tag{1.26}$$

Apparent magnitude (m) is a measurement of the brightness of an astronomical object as seen by an observer on Earth in the absence of an atmosphere. The value is based on comparison with a reference source in the same passband. A lower value represents a brighter object.

$$m_i = -2.5\log_{10}(b_i/b_{ref,i}) \tag{1.27}$$

where i is a given photometric passband, b_i is the flux of the source in passband i and $b_{ref,i}$ is the flux of a reference source in the same passband. Traditionally the star Vega is used as a reference, however other systems exist such as the AB magnitude system which uses the following formula (Oke and Gunn 1983):

$$m_i = -2.5\log_{10} f_i - 48.60 \tag{1.28}$$

where f_i is the flux density of the source and the constant 48.60 sets the point of zero apparent magnitude to be where $F_v = 3631Jy$.

The **absolute magnitude** (M) of an object is defined to be equal to the apparent magnitude of the object for an observer a distance of 10 parsecs away from it.

An important quantity in supernova cosmology, is the **distance modulus** (μ) which is the difference between the apparent and absolute magnitudes of an object and is related to the

luminosity distance by

$$\mu = m - M = 5 \log \left(\frac{d_L}{1[\text{Mpc}]} \right) + 25 \tag{1.29}$$

It is this quantity, μ, that we use to plot Hubble diagrams for the constraining of cosmological parameters using supernova observations.

1.2.2 Measuring Distances

Luminosity distance is a commonly used distance measure. It requires knowledge of an object's intrinsic luminosity. The term 'standard candle' refers to a fictitious object that has constant luminosity throughout the Universe so that its apparent magnitude is a direct measure of distance.

For Cepheid variable stars there is a tightly constrained relationship between the period of the variations and the luminosity. This makes it possible to calibrate them for use as standard candles. The luminosity L is approximately proportional to the period P raised to the power of 1.3, i.e. $L \propto P^{1.3}$. The period of these stars can be measured from their light curves and used to infer their luminosities and ultimately their distance. The distance to the Large Magellanic Cloud (LMC), which forms the first rung in the distance ladder, is measured using Cepheids (Peacock 1999). This method is only possible within our local environment since in more distant galaxies it is not possible to resolve individual objects and thereby detect a population of Cepheid variable stars.

Relations between observable galaxy properties and galaxy luminosity can be used in a similar way to estimate relative distances. One such relation is between the surface brightness I_0 and central dispersion velocity σ_v of elliptical galaxies which suggests that these objects have a roughly constant mass-to-light ratio. The Faber-Jackson relation for elliptical galaxies and the Tully-Fisher relation for spiral galaxies relate luminosity to the central velocity dispersion in ellipticals and rotational velocity in spirals which are observable quantities. These methods cannot provide absolute distances due to the large scatter in galaxy properties.

At cosmological distances, we use type Ia supernovae to measure distances. Their properties make them very good standard candles and allow us to calculate absolute distances at significant redshifts. Section 1.4 explains the physics of type Ia supernovae as well as how they are used in cosmology and some of the discoveries they have enabled.

1.3 Perturbations and Peculiar Velocities

The standard model and the associated equations presented in Section 1.1.1 are useful and appear to be a good approximation to our observed reality. We find that on the largest scales the assumptions of homogeneity and isotropy appear to hold true. However, on smaller scales this is not the case; we observe distinct structure and density variation all around us in the form of planets, galaxies and clusters.

An important challenge for cosmologists is explaining how the uniformity of the CMB could give rise to the richness of structure that we see on a wide range of scales. A generally accepted explanation is that very small density fluctuations in the CMB ($< 10^{-5}$) are amplified into deep potential wells and through gravitational interaction these trigger the hierarchical formation of structure. To study this we use perturbation theory, assuming a very small density perturbation ρ on top of a uniform mass density equal to the mean mass density ρ_0. We can then define a dimensionless density perturbation as

$$\delta \equiv \frac{\rho - \rho_0}{\rho_0} \tag{1.30}$$

This represents the fractional departure or density contrast of the local density at a point from the mean density.

Gravitational forces act to enhance the density contrasts in the distribution of matter as areas of higher density attract more matter into their surrounds. All particles are subject to the Hubble expansion and thus possess a recession velocity which is governed by Hubble's Law (Equation 1.2). Gravitational interaction in an environment of non-uniform matter distribution induces an additional velocity in the direction of local overdensities which we call peculiar velocity. Peculiar velocity is related to the density perturbation as follows:

$$\bigtriangledown \cdot \mathbf{v} = -a\frac{\partial \delta}{\partial t} = a\delta\frac{\dot{D}}{D} \tag{1.31}$$

In Equation 1.31, D is the growing mode of the perturbations which is one of two solutions to a second-order differential equation (Equation A.6). A derivation of the growing mode and the above relation, using linear perturbation theory, is given in Appendix A.

Consequences of Peculiar Velocities

Peculiar velocities are caused by the inhomogeneities in the distribution of matter in the Universe and, therefore, are not explained by Hubble expansion. They affect our observations of the universe: our own peculiar velocity is visible in the CMB dipole which is the Doppler effect of our movement relative to the comoving background of CMB radiation. They also have other observational consequences which affect the accuracy of supernova cosmology (Section 1.5).

From an observer's point of view, a peculiar velocity can be decomposed into a transverse component which is perpendicular to the line of sight and a radial component along the line of sight.

The transverse component affects the position of an object on the sky. This is similar to the proper motion of a star although we generally consider peculiar velocities as relating to extragalactic objects. Proper motions of stars in the Milky Way can feasibly be measured because they are nearby. However, due to the distances to most galaxies, measuring the effect of transverse peculiar velocities requires extremely precise measurements of positions which are currently impossible. This may change in the near future with telescopes such

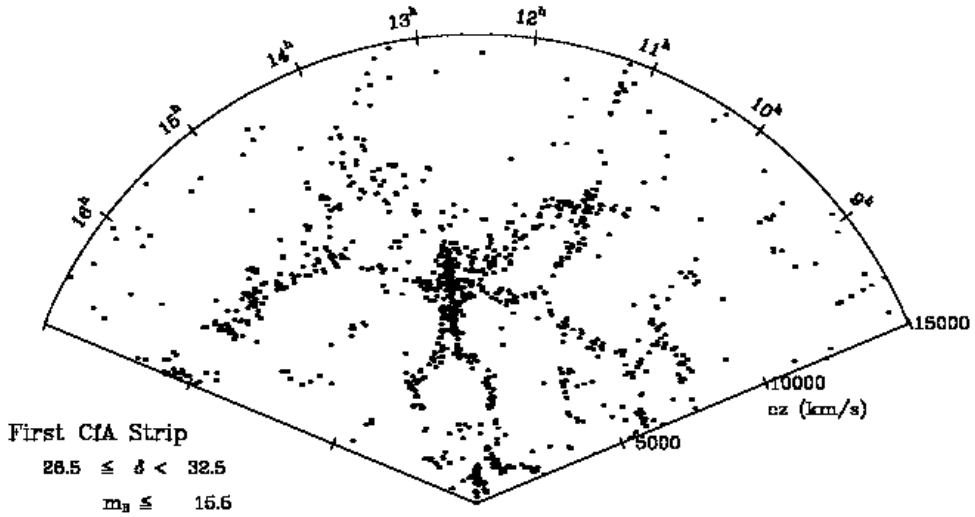

Figure 1.1: The Coma cluster, observed in 1985 as part of the CfA Redshift Survey and displaying the typical 'fingers of God' elongation in redshift space caused by peculiar velocities (Thorstensen et al. 1989).

as GAIA and SKA which aim to reach resolutions of the order of microarcseconds. These instruments may make it possible to measure the change in position of galaxies over a period of ten to twenty years. Quercellini et al. (2010) propose this new approach and call it real-time cosmology.

The radial component alters the apparent redshift of an object due to Doppler effects. Where the radial peculiar velocity is directed towards the observer the photons are blueshifted and the object appears less redshifted than expected if the redshift is related only to Hubble expansion. Conversely, where the radial component of the peculiar velocity is directed away from the observer the object appears more redshifted than expected. The 'fingers of God' observed in galaxy clusters are caused by this. The Doppler shifting causes galaxies falling in to the cluster from the far side to be blueshifted and those falling in from the near side to be redshifted. As a result the cluster appears elongated (into 'fingers of God') in redshift space along the line of sight as seen in Figure 1.1. In future, another branch of real-time cosmology proposed by Quercellini et al. (2010) may be able to use very high resolution spectrographs such as the CODEX instrument for the European Extremely Large Telescope (E-ELT), to measure the change in redshift due to peculiar velocities over a ten to twenty year period.

It is the radial component of the peculiar velocity and its effect on redshift that is of interest in this work. For the remainder of this thesis the use of the term peculiar velocity will refer specifically to the radial component of the peculiar velocity unless clearly stated otherwise.

We can get some estimate of peculiar velocities from studying large numbers of galaxies in redshift surveys and averaging over their properties. This technique can provide some insight into large bulk flows. However, our current inability to accurately specify these velocities means that there is uncertainty in all redshift measurements. The impact of this uncertainty on supernova cosmology is investigated in this work.

1.4 Type Ia Supernovae

A supernova is the name given to the explosion of a star at the end of its life. Supernovae can be of various types. In cosmology we are interested in those of type Ia which are discussed in detail in Sections 1.4.2, 1.4.3 and 1.4.4. Sections 1.4.1 discusses the classification of supernovae into each of the four types.

1.4.1 Supernova Classification

Supernovae are classified based on features in their spectra into types. Type I supernovae are hydrogen deficient and therefore the spectra show no hydrogen emission. There are three subtypes of hydrogen deficient supernovae: type Ia, type Ib and type Ic. Type Ia spectra display a characteristic feature of blueshifted silicon (SiII) in deep absorption. They also usually show absorption of intermediate elements calcium and sulphur. Type Ib spectra are distinct due to the presence of strong helium lines. Type Ic spectra are deficient in helium as well as hydrogen and do not show the characteristic silicon features of type Ia. Supernova spectra that show hydrogen emission are classified as type II. Figure 1.2 shows typical spectra for supernovae of types Ia, Ib, Ic and II.

The focus of this work in on type Ia supernovae (hereafter, SNIa) because of their importance in cosmology and the details of the physics behind them and how they are used in cosmological studies are discussed in the following sections.

Unlike SNIa, the physical mechanism behind the explosion of type Ib/c and type II supernovae is core-collapse of the progenitor star. There have been proposals for using core-collapse supernovae as distance indicators. In particular, for type II supernovae there is a correlation between the expansion velocity and luminosity during the plateau phase of the explosion which is linked to the atmosphere of the supernova. Calculated values for the Hubble constant using type II supernovae are between 65 and 70 $\mathrm{kms}^{-1}\mathrm{Mpc}^{-1}$ (Leibundgut 2008). This method could possibly provide another independent probe into the Universe's expansion history which could be compared with the results derived from SNIa.

1.4.2 Type Ia Supernova Data

As mentioned previously, we use spectroscopy to identify supernovae of type Ia based on a lack of hydrogen and the presence of silicon (SiII) and sometimes also intermediate elements Calcium (CaII) and Sulphur (SII). Figure 1.3 shows three typical type Ia spectra showing the characteristic silicon feature at 6150 Å.

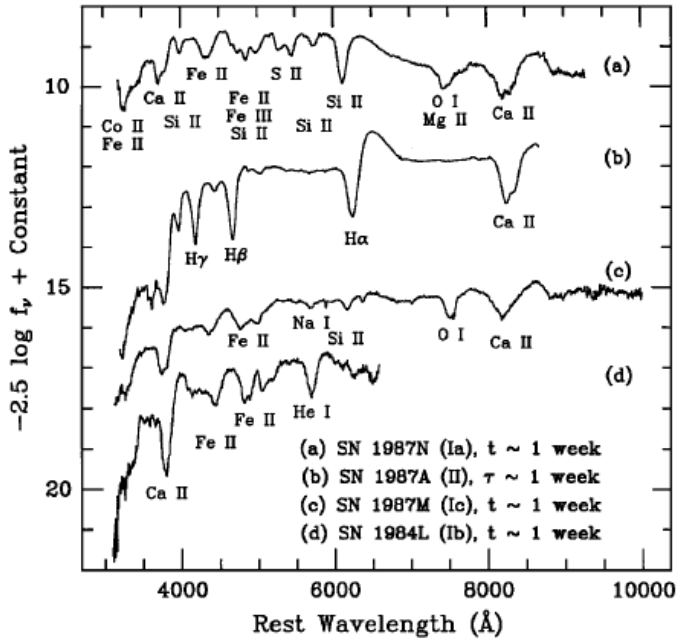

Figure 1.2: Typical spectra for supernovae of types Ia, II, Ic and Ib (Filippenko 1997). The Ia spectrum is identified by the deep silicon absorption, Ib by helium features and the type II spectrum has clear hydrogen lines.

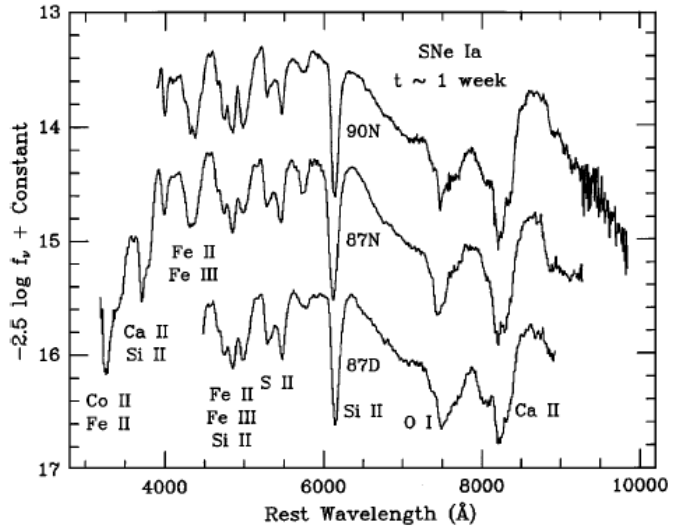

Figure 1.3: Spectra of three different SNIa taken approximately one week after maximum brightness (Filippenko 1997). The supernovae shown here are SN 1990N, SN 1987N and SN 1987D.

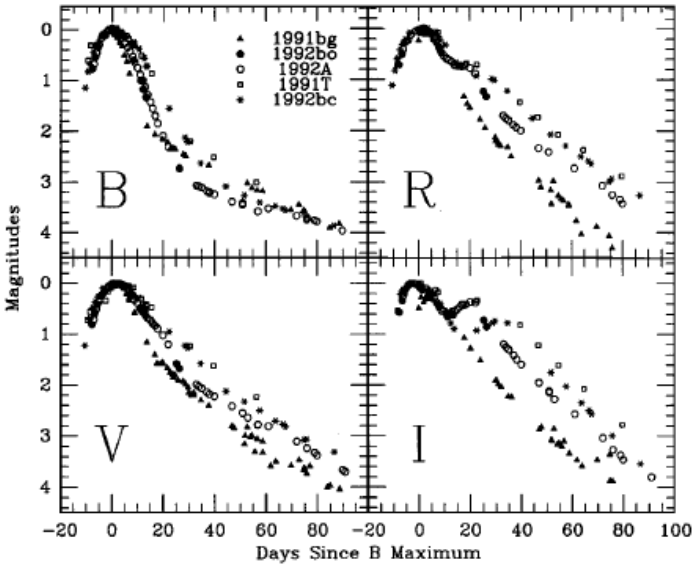

Figure 1.4: Lightcurve evolution in B, V, R and I bands for a number of bright SNIa, from Filippenko (1997).

Photometric data, or light curves, of SNIa are also important. Light curves measure the magnitude of the SNIa as a function of time. There is a remarkable homogeneity in the time evolution of the light curves of SNIa which is central to their usefulness in cosmology. Figure 1.4 shows the light curve data for a number of SNIa in four different filters.

1.4.3 Physics of Type Ia Supernovae

Unlike other types of supernovae which are attributed to core-collapse in massive stars, SNIa are caused by thermonuclear explosions of compact white dwarf stars (Leibundgut 2008), however, there is still debate about some details of the model. We believe that the progenitors for SNIa are binary systems which involve an electron-degenerate white dwarf accreting material from a companion star. When the mass of a (non-rotating) white dwarf approaches the Chandrasekhar limit of 1.4 solar masses ($M_{\odot}$) the gravity can no longer be supported by the electron degeneracy pressure and the increases in temperature and pressure set off explosive burning of carbon and oxygen. This process creates a large instability and convection in the star which can continue for several hundred years (Goobar and Leibundgut 2011). Eventually, the growing convective region triggers a runaway process causing the entire star to be destroyed in a matter of seconds. The explosion is powered by the radioactive nickel ^{56}Ni as it decays to ^{56}Co and then ^{56}Fe (Goobar and Leibundgut 2011). The ^{56}Ni is formed during the centuries of convection. Silicon, calcium and sulphur are intermediate elements in the formation of ^{56}Ni. These are likely to be present at the time of explosion and are generally prominent features in the SNIa spectra.

The homogeneity of SNIa stems from the fact that the disruption of the progenitors

occurs at the Chandrasekhar limit and therefore at a common mass. This suggests that the progenitors will contain similar levels of heavy elements. The peak brightness of the event depends on the amount of ^{56}Ni. Different amounts of ^{56}Ni result in the scatter of the peak magnitudes as seen in the top panel of Figure 1.5. The relationship between peak magnitude and decay time that allows us to standardise SNIa for use as standard candles can also be explained using this model. SNIa with brighter peak magnitudes result from progenitors with larger quantities of ^{56}Ni, possibly due to longer periods of convection. This results in explosions with higher temperatures and greater opacity which increases the photon diffusion time and causes a slower decline in the lightcurve.

SNIa occur in a variety of environments. The local SNIa rate is approximately 3×10^{-5} SNIa per cubic Mpc per year (Goobar and Leibundgut 2011) which makes these very rare events. The rate in galaxies with active star formation is higher which suggests that a significant fraction of SNIa occur in young stellar populations (Mannucci et al. 2005). However, SNIa are observed across a wide range of environments including red elliptical galaxies which have no star formation, which implies that it is also possible for their progenitors to have very long lifespans of the order of a few billion years.

1.4.4 Type Ia Supernovae as Standard Candles

SNIa are ideal standard candles for two reasons:

Firstly, their light curves are remarkably similar as seen in the top panel in Figure 1.5, which shows the lightcurves of SNIa from the Calan/Tololo survey (Hamuy et al. 1996). The lightcurves can be made even more homogeneous by normalising them according to a relation between the peak magnitude and the rate of decay in luminosity after the peak discovered by Phillips (1993). Using this relationship to apply a second order correction to the SNIa data results in the lightcurves appearing almost indistinguishable from one another as shown in the lower panel of Figure 1.5. The scatter in the peak magnitude after the correction is reduced to ~ 0.15 magnitudes. This normalisation gives a peak magnitude in the B-band of $M_B \sim -19.5$. This is the reference magnitude used in the luminosity distance formula (Equation 1.22) to calculate the absolute distance to each SNIa.

Secondly, SNIa are very luminous. Their brightness often exceeds that of the host galaxy in which they occur. The luminosity makes SNIa perfect for use as cosmological standard candles because they can be seen out to cosmological distances.

1.4.5 Supernova Cosmology

The central theme in supernova cosmology is the measurement of the expansion history of the Universe and determining quantities like the matter density Ω_m and the equation of state parameter for dark energy w, to test against cosmological models. Using Hubble diagrams which plot SNIa redshift against their distance modulus we calculate estimates and constraints for these and other parameters. The best fit line to the supernova data points defines the best fit cosmology and this is used to constrain the values of cosmological

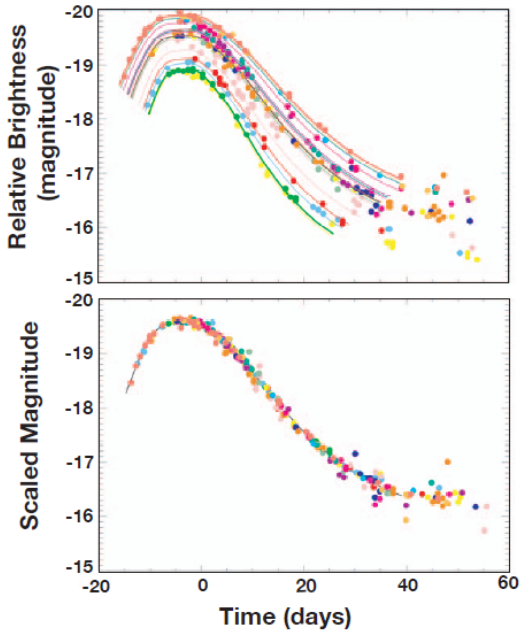

Figure 1.5: *Top*: Lightcurves for SNIa with no correction applied. *Bottom*: The same SNIa lightcurves normalised using the relationship between maximum brightness and decay time. After the correction is applied the scatter in the peak magnitudes is reduced to 0.15. This figure is taken from Kim (1997) and uses supernova data from the Calan/Tololo Survey (Hamuy et al. 1996).

parameters. Figure 1.6 shows a Hubble diagram from Kessler et al. (2009) which includes a number of different SNIa datasets. In working towards the best possible constraints, we combine the results from supernovae with estimates from other types of data. Figure 1.7 shows the parameter space for Ω_m and Ω_Λ with the constraints imposed by SNIa, baryon acoustic oscillations and the CMB and also showing the line representing a flat universe (i.e. $\Omega_m + \Omega_\Lambda = 1$).

SNIa provide key evidence for the accelerated expansion of the Universe which is one of the most important cosmological discoveries of the last twenty years. In 1998, using results from the High-Z Supernova Survey and the Supernova Cosmology Project, both Riess et al. (1998) and Perlmutter et al. (1998) presented evidence that the expansion of the Universe is accelerating. The findings were based on observations of distant SNIa that appeared fainter than they should in a massless, empty universe. The acceleration of expansion is now widely accepted (Leibundgut 2008), and the 2011 Nobel Prize in Physics was awarded jointly to Saul Perlmutter (Supernova Cosmology Project) and Brain Schmidt and Adam Riess (High-Z Supernova Survey) for their discovery. Figure 1.8 shows the results of the High-Z Supernova Survey in the $\Omega_m - \Omega_\Lambda$ plane.

Several projects including the Supernova Legacy Survey (SNLS), ESSENCE and Sloane Digital Sky Survey (SDSS) are using distant SNIa for measuring the value of w, the equation

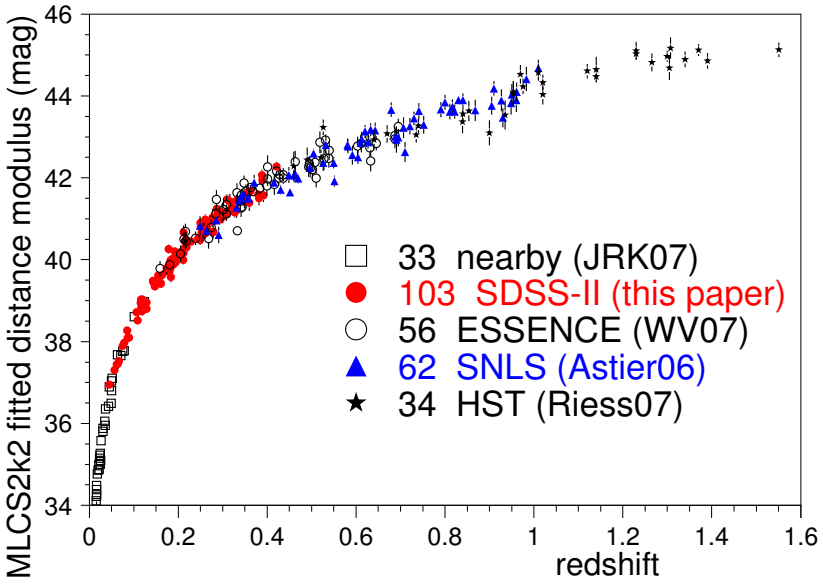

Figure 1.6: Hubble diagram by Kessler et al. (2009) showing 288 SNIa from the samples listed on the plot.

of state parameter for dark energy. Other projects are gathering supernova data for various purposes including to better understand the environments in which these events occur and to attempt to reduce their observed scatter on the Hubble diagram.

1.5 Supernova Cosmology and Peculiar Velocities

As explained in Section 1.4.5, the key observables in supernova cosmology studies are redshifts and the magnitudes from which we calculate luminosity distances. However, as discussed in Section 1.3, the quality of the redshift data is compromised by the peculiar velocities that exist as a result of structure in the Universe.

The peculiar velocities cause a scatter in the redshift (x-axis of the Hubble diagram). The cosmological redshift is the redshift of an object if it were to have zero peculiar velocity, that is the redshift due only to expansion. The redshift that is measured by an observer, and is therefore altered by the peculiar velocity of the object itself, is called the observed or apparent redshift. The central aim of supernova cosmology is determining a best-fit cosmology for the data and thereby constraining the values of the cosmological parameters. The scatter in redshift may result in a different, and inaccurate, best-fit cosmology and therefore lead to inaccurate parameter constraints.

In a random density and velocity field, the random directions of the peculiar velocities in a supernova sample should result in a random scatter in the Hubble diagram around the true cosmology. In this case, the effect can be accounted for by inflating the errors on the distance modulus to include an additional error due to the velocities (this is explained in detail in

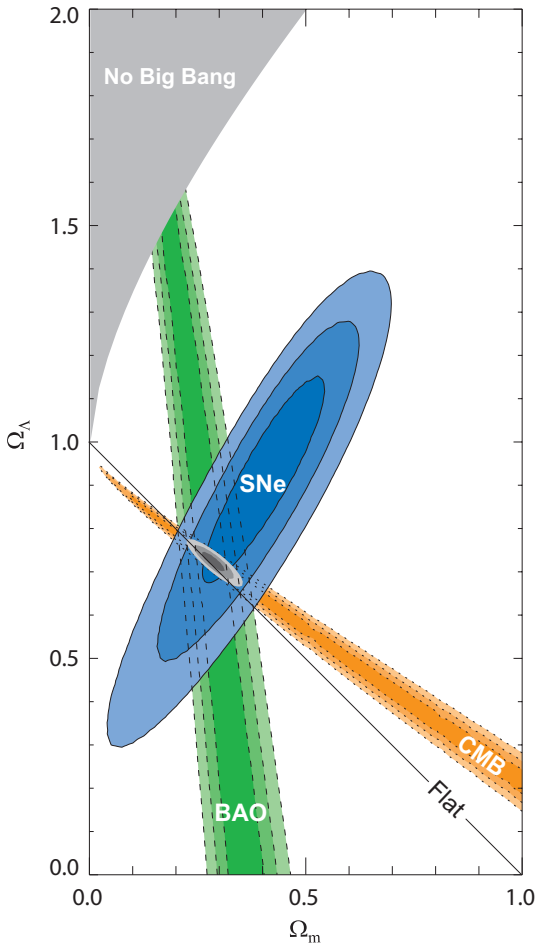

Figure 1.7: Constraints in the $\Omega_m - \Omega_\Lambda$ plane from the CMB, baryon acoustic oscillations and SNIa (Kowalski et al. 2008).

Section 4.1.1). On the other hand, where there are correlations in the peculiar velocities, there may be a coherent shift in the data which could bias the resultant cosmology. Such correlations could be the result of large scale bulk flows.

The correlations due to peculiar velocities should be modeled using a data correlation matrix. However, historically, this is translated into the velocity error added to the distance modulus errors instead. This is done for ease of computation and is justified by the fact that the errors on measured magnitudes are significantly larger than those on spectroscopically confirmed redshifts. The velocity error σ_{pec} is added in quadrature to the errors caused by the scatter in the peak magnitudes of SNIa and the fitting of the supernovae light curves. The mathematical details of the errors are explained in more detail in Section 4.1.1.

The effect of peculiar velocities on SNIa is predominantly a low redshift effect. This is because more distant objects with higher redshifts have larger recession velocities and so the contribution to redshift from the peculiar velocity is proportionally much smaller, and also because the correlations due to peculiar velocities decay rapidly with increased separation

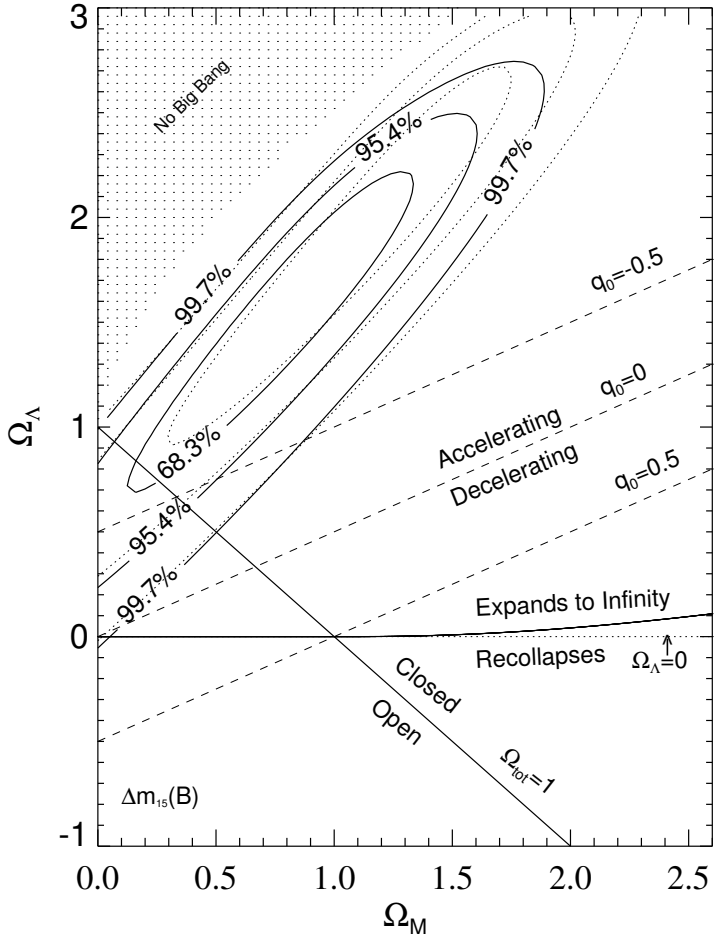

Figure 1.8: Cosmological constraints from the High-Z Supernova Survey with the region corresponding to accelerated expansion indicated by the dashed lines (Riess et al. 1998). The dotted contours are the constraints calculated when the unclassified supernova SN 1997ck is excluded from the dataset.

and redshift as seen in Figure 1.9. Some supernova cosmologists reduce the impact of peculiar velocities on their results by implementing a low redshift cut and ignoring all supernova data below a redshift of, for example, $z = 0.02$ (Davis et al. 2010).

1.6 In This Work

Future supernova surveys expect to discover many thousands of SNIa. This may result in the reduction of the magnitude errors to the point where they are comparable to the redshift errors and therefore increase the importance of understanding peculiar velocities. The new surveys are also likely to obtain large amounts of low redshift data, which may need to be

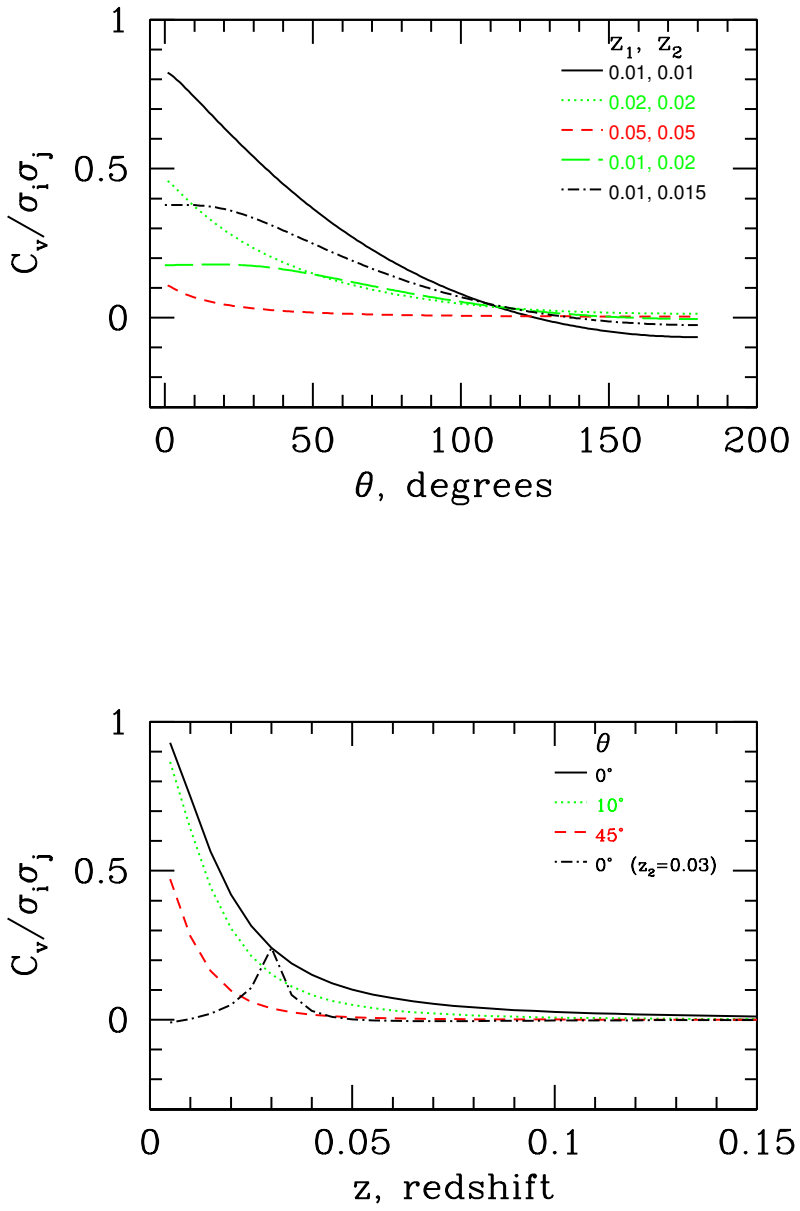

Figure 1.9: Figure taken from Gordon et al. (2007). The ratio of covariance from peculiar velocities C_v, to the random errors σ, for a pair of supernovae, over a range of angular separations, computed by Gordon et al. (2007) using 300 nearby supernovae. *Top:* The separation on the sky, θ, is varied. *Bottom:* The redshift is varied, with both supernovae at the same z or with one fixed at $z = 0.03$ (dash-dot).

disregarded if the peculiar velocity effect is not better understood.

The purpose of this work is to create a simulated SNIa dataset and use it to quantify the effects of peculiar velocities in various scenarios. The aim is to evaluate the significance of the effect and the importance of addressing it in future supernova cosmology studies.

Chapter 2 explains the simulation and resulting galaxy catalogues used in this work and Chapter 3 explains the analysis methodology. The results of simulating SNIa data, and the parameter estimation are discussed in Chapter 4 and the conclusions are summarised in Chapter 5.

Chapter 2

Data

In this study we build simulated supernova catalogues using the mock galaxy surveys constructed by Kitzbichler and White (2007), which are in turn built from the De Lucia and Blaizot (2007) galaxy catalogues based on the output of the Millennium (N-body) Simulation. Simulated data provides us with explicit information about the peculiar velocities of the galaxies and thus enables us to quantitatively analyse their effect on parameter constraints. The concepts of N-body simulations, galaxy catalogues, mock surveys and supernova rates are explained in this chapter.

2.1 N-body Simulations

We need to test our current theoretical understanding against the observable universe in order to advance our knowledge of cosmology. Surveys like SDSS (Castander 1998) and the 2 degree Field Galaxy Redshift Survey (2dFGRS, Colless et al. (2001)) have improved our knowledge about the structure of the Universe by characterising the properties and spatial distribution of galaxies. The aim of gathering such data is to investigate of the formation of galaxies, the growth of cosmic structure and to search for possible characteristics that would shed light on such mysteries as dark matter and dark energy. These investigations rely on the comparison of observed data with precise predictions based on our theoretical models, testing the correctness of our models to enable us to identify ways of refining and improving them.

N-body simulations have become an essential probe of theoretical predictions to compare with observations. The growth of density perturbations that drive the hierarchical formation of structure is based on gravitational dynamics and hydrodynamics that quickly enter highly non-linear regimes and involve inherently complex three-dimensional geometry as the system develops (Springel 2005). This complexity makes analytical solutions impossible and the only way that the theoretical cosmological predictions can be calculated is through direct numerical simulation.

Most cosmological N-body simulations are focused on dark matter, the dominant matter

component in the Universe. Assuming dark matter only interacts gravitationally, it can be approximated by a collisionless fluid and represented by discrete particles or bodies (hence the name N-body simulations) that evolve under self-gravity. The evolution of structure is governed by the physics and phenomenological models of various processes that are included in the simulation code equations and parameters. These inputs represent our best understanding of the physics of structure formation at the time of running the simulation.

The validity of the N-body representation and the accuracy of the simulation results increases as the number of particles in the system increases. For predictions of structure formation the dynamic range of the simulation needs to be very large (Springel et al. 2005) which is a challenge due to finite computational resources such as CPU time and processing power. There is a trade-off between the benefit of having a higher density of particles in the simulation box in order to resolve low luminosity galaxies and the benefit of having a larger simulation volume to ensure the presence of rarer objects like quasars and rich clusters in the simulated universe.

Springel (2005) lists and references some of the important results in theoretical cosmology that can be largely attributed to simulation work. The list includes: density profiles of dark matter halos, the non-linear clustering properties of dark matter, profiles of temperature and gas in galaxy clusters and the detailed properties of Lyman-α absorption in the interstellar medium (ISM). While structure formation has been the focus of much of the simulation work to date, many unanswered astrophysical questions involve the interactions of complex processes for which simulations may be the only way to compute predictions. This, coupled with the continued improvements and innovations in computational technology, suggests an increased dependence on simulations in the future.

2.2 The Millennium Simulation

The Millennium Simulation is the largest N-body simulation carried out to date. It incorporates over ten billion particles. It was performed at the Max-Planck Institute for Astrophysics in Garching, Germany by the Virgo consortium using a specially customised version of the GADGET2 code (Springel 2005). The running of the simulation required improvements in the simulation algorithms, significant parallelisation, 1 TB of memory and 350 000 hours of CPU time and it produced nearly 20 TB of raw data. The gravitational interactions were computed using a combination of a hierarchical multipole expansion algorithm (also called a tree algorithm) and a Fourier transform particle-mesh method.

The simulation traces the trajectories of dark matter particles through the development of hierarchical structure from redshift 127 to the present epoch according to a ΛCDM cosmological model with the following parameters: $\Omega_m = \Omega_{dm} + \Omega_b = 0.25$, $\Omega_b = 0.045$, $h = 0.73$, $\Omega_\Lambda = 0.75$, $n = 1$ and $\sigma_8 = 0.9$.

The Hubble constant is parameterised as $H_0 = 100h\text{km s}^{-1}\text{Mpc}^{-1}$. Ω_b and Ω_Λ represent the densities of baryons and dark energy respectively at the present day. The above parameter values are consistent with the first year WMAP data combined with the results

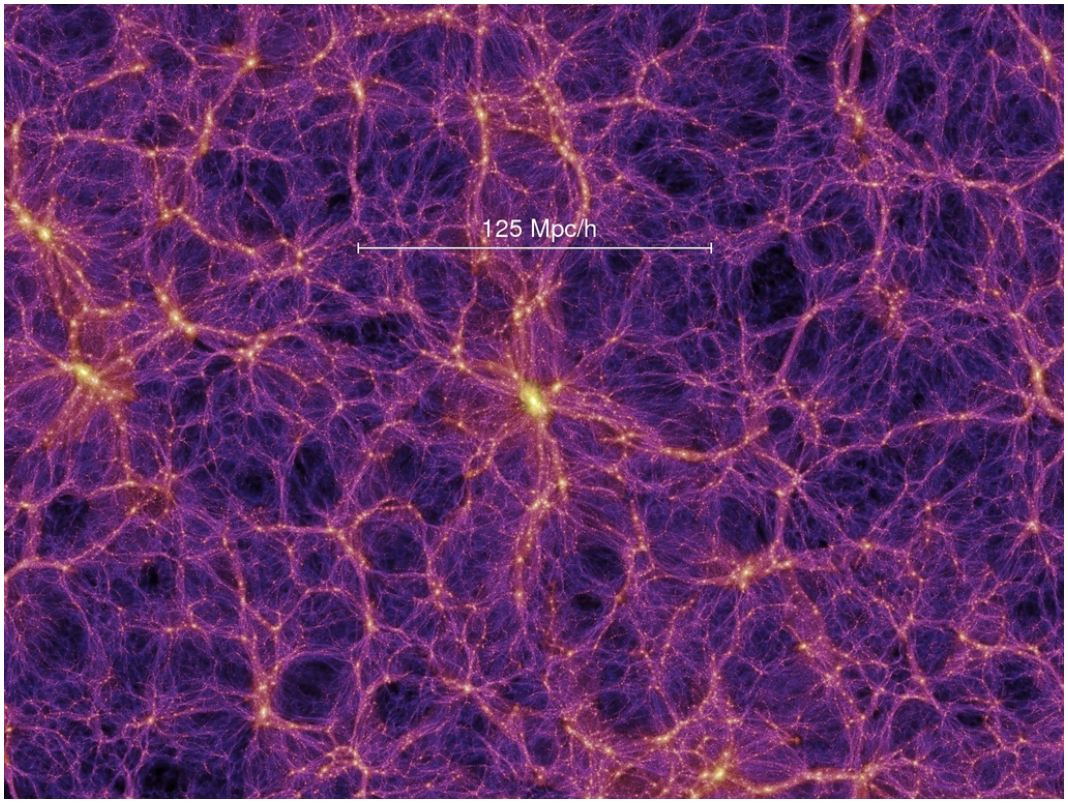

Figure 2.1: The dark matter distribution at redshift zero from the Millennium Simulation for a slice of thickness $15h^{-1}$Mpc. The colour relates to the local velocity dispersion and the intensity to the surface density. The image is available for downloading from the Millennium Simulation website maintained by Virgo consortium and hosted by the Max-Planck Institute for Astrophysics in Garching, Germany (http://www.mpa-garching.mpg.de/galform/virgo/millennium/).

of the 2dFGRS. In Guo et al. (2011) it is noted that these parameters are not consistent with more recent analyses of the CMB using the 7 year WMAP data which is presented in detail in Komatsu et al. (2011). However, the effect is not overly significant in the galaxy population work presented in Guo et al. (2011) and the Millennium Simulation is still, at this point in time, the most comprehensive simulation data available. Figure 2.1 shows a slice of thickness $15h^{-1}$Mpc through the dark matter density field of the simulation output at redshift $z = 0$.

Mass Resolution

The mass resolution of an N-body simulation is governed by the number of particles and the simulation volume. In the case of the Millennium Simulation there are $2160^3 \simeq 1.0078 \times 10^{10}$ particles in a volume that is a periodic cube with sides of $500h^{-1}$Mpc. This yields a mass of $8.6 \times 10^8 h^{-1}$ solar masses (hereafter, $M_\odot$) for each individual particle. The mass resolution achieves a dynamic range of 10^5, sufficient for representing a wide range of objects including:

rich galaxy clusters with several million particles, Milky Way type galaxies with about a thousand particles and dwarf galaxies as faint as $0.1L_\star$ with about a hundred particles (Kitzbichler and White 2007). The simulated universe is spatially resolved to $5h^{-1}$kpc throughout the volume and contains dark matter halos of all sizes connected with filamentary structure that has become known as the cosmic web. At $z = 0$ there are approximately 18 million dark matter halos above the 20 particle detection limit.

Simulation Output

The simulation output consists of 64 snapshots: the complete set of particle data is stored at 60 different epochs between redshift $z = 0$ and $z = 20$ and additional snapshots are added at $z = 30, 50, 80, 127$ (Croton et al. 2006). Also available from the simulation run are finely resolved merging trees for millions of halos and their surviving subhalos. The halos are identified by a standard friends-of-friends group-finder which is part of the simulation code. Subhalos are identified in post-processing using an optimised version of the Springel et al. (2001) SUBFIND algorithm. The threshold for what is considered a substructure is 20 particles; groups of particles of less that this number are considered to be below the detection limit and not catalogued as self-bound halos. In the hierarchical development of structure in a ΛCDM universe, a dark matter halo at a given time can have multiple progenitors but will produce a unique descendant in subsequent mergers. Using this concept a merging tree is constructed for each halo at redshift zero. This incorporates the full set of progenitors going back through all the generations in the simulation.

While the simulation itself includes no baryonic matter, the merging trees can be used along with any semi-analytic galaxy formation model to build galaxy catalogues containing around 2×10^6 galaxies at the present day. The galaxy catalogues will include the full histories of each galaxy as gathered from the merging information provided by the simulation.

The semi-analytic model described briefly in Springel et al. (2005) and in detail in Croton et al. (2006) was the basis of the model adopted by De Lucia and Blaizot (2007). The galaxy catalogues produced by De Lucia and Blaizot (2007) underly the mock surveys of Kitzbichler and White (2007) that are used in this peculiar velocity study. The semi-analytic model and the process of creating the mock surveys are discussed in Section 2.3.

2.3 Millennium galaxies

Kitzbichler and White (2007) compare the galaxy population at high redshift as predicted by the hierarchical galaxy formation model of De Lucia and Blaizot (2007) with the observed high redshift galaxy population. The implementation of various baryonic processes in the (De Lucia and Blaizot 2007) model produces good results locally when compared with observations but had not previously been evaluated at high redshifts. In order to make a comparison with the observed high redshift galaxy population, mock results are constructed for deep observations of the simulated Millennium universe from the De Lucia and Blaizot (2007) galaxy catalogues.

The mock survey results contain the details of all the galaxies within a defined observer's backwards light cone for a specific 2 degree field in the simulated Millennium sky. The galaxy properties provided in the catalogues include their apparent magnitudes and observed redshifts according to the observer.

2.3.1 Semi-analytic model

The baryonic processes that are simplified into various differential equations in the galaxy formation models include star formation, galaxy mergers, gas cooling, the effects of reionisation, the feedback from supernovae and the evolution of supermassive black holes.

The handling of gas cooling, reionisation and supernovae feedback effects follow the methods used in Springel et al. (2001) and De Lucia et al. (2004). The gas cooling model assumes that the fraction of mass comprised of baryons after the collapse of a dark matter halo is 17% in all cases which is consistent with first year WMAP data. Reionisation is modeled as in Kravtsov et al. (2004) where the reionisation process is divided into three epochs: $z > z_0$ where there are no overlapping HII regions, $z_0 < z < z_r$ where there are multiple overlapping HII regions and $z < z_r$ where the intergalactic medium is almost completely ionised. The values $z_0 = 8$ and $z_r = 7$ are adopted as in Kravtsov et al. (2004). Supernovae feedback is the release of metals, gas and energy into the interstellar medium as a result of supernovae occurring in galaxies. The feedback can result in an ejection of gas from the halo in a wind which may be reincorporated into the halo as it enlarges. The model used allows for all of the ejected gas to return to the halo over a few dynamical halo times.

Galaxy mergers are an important component of galaxy evolution as they impact star formation and galaxy morphology. The merging model allows for two different types of merger. A minor merger is where one of the progenitors has a significantly larger baryonic mass than the other, in which case the stars of the smaller galaxy end up in the bulge of the larger galaxy and the cold gas and stars newly formed as a result of the merger end up in the disk. A major merger occurs when the progenitors are of a similar baryonic mass, in particular when the mass ratio T_{merger} between the progenitors is larger than 0.3. In this case there is more starburst activity and the disks of both galaxies are destroyed and incorporated into a single spheroidal structure containing all the stars. The starburst resulting from the collision is generated according to the 'collisional starburst' model of Somerville et al. (2001).

The model of Springel et al. (2005) and Croton et al. (2006) introduces a new approach to the growth of supermassive black holes. They define two distinct modes of gas accretion onto the black hole. Firstly, the quasar mode which is dominated by the accretion of cold gas from galaxy disks during major mergers and is an extension of existing black hole growth models such as that of Kauffmann and Haehnelt (2000). The new, second mode is explained in detail in Croton et al. (2006). It is called the radio mode and represents feedback at radio wavelengths as a result of the accretion of hot gas onto the black hole once a stable hot halo forms around the host galaxy. The radio mode, which only has an impact a late times,

causes heating in the surrounding medium and suppresses the cooling flow at late times which is successful in producing the observed properties of bright low redshift galaxies.

While the majority of the semi-analytic model from Croton et al. (2006) is used, there are a couple of changes made by De Lucia and Blaizot (2007). One of these is that the time taken for the galaxies at the centres of subhalos disrupted to below the resolution limit of the simulation (20 particles) to attach to the central galaxy in the surrounding halo is doubled. The increased time creates a better fit at the bright end of the luminosity function. Another deviation from the Croton et al. (2006) model is the use of the Bruzual and Charlot (2003) stellar population synthesis model with the Chabrier (2003) initial mass function for star formation.

2.3.2 Constructing mock surveys

Each mock survey created by Kitzbichler and White (2007) is a wedge that is cut from the full simulated sky that is specific to an observer defined within the simulated Millennium universe. The dimensions of the wedge are set to mimic the field of view of a survey for which mock observations are being developed. The observer's full sky is populated by those galaxies with world lines that intersect with the observer at the present day (redshift $z = 0$). That is, all galaxies that lie on the observer's backward light cone. Figure 2.2 shows an example of one of these mock surveys.

A major challenge in the creation of mock surveys is managing the limited size of the simulation volume. The $500h^{-1}$Mpc side of the simulation is equivalent to the comoving distance to a redshift of $z = 0.17$. The boundaries of the simulation are periodic and therefore in principle it is reasonable to replicate the simulation box over and over to create larger comoving distances. However, if an observer views such an extended simulation along one of the principle axes of the volume, there is a kaleidoscope effect which makes the resulting mock survey unrealistic. The kaleidoscope effect can be avoided by choosing a line of sight that is not aligned to any of the principle axes of the simulation volume. The optimal line of sight depends on the survey to be simulated. Kitzbichler and White (2007) restrict themselves to solving the problem for deep, narrow surveys and do not attempt to find a general solution to the problem. Using a line of sight that passes through the origin and the point $(L/m, L/n, L)$, where m and n are integers with no common factors and L is the length of the sides of the cube, results in the first periodic image appearing at the point (nL, mL, nmL). The observational field is defined by the four points $((n \pm 0.5/m)L, (m \pm 0.5/n)L, nmL)$ which results in a field of view of $1/m^2n \times 1/n^2m$ square radians where the first duplicated point occurs at approximately mnL. Applying this model to the Millennium Simulation which has $L = 500h^{-1}$Mpc the maximum redshift before duplication and the size of the survey field are defined by the choice of m and n. For example, for $m = 2$ and $n = 3$ the resulting mock survey is free of duplication out to $z = 1.37$ with a field of view of 4.8×3.2 square degrees. Similarly, $m = 3$ and $n = 4$ yields a survey of 1.6×1.2 square degrees out to $z = 5.6$ with no duplication. The cutting out of wedges from the observer's virtual sky using simple Euclidean geometry is only possible for comoving distances in a flat universe.

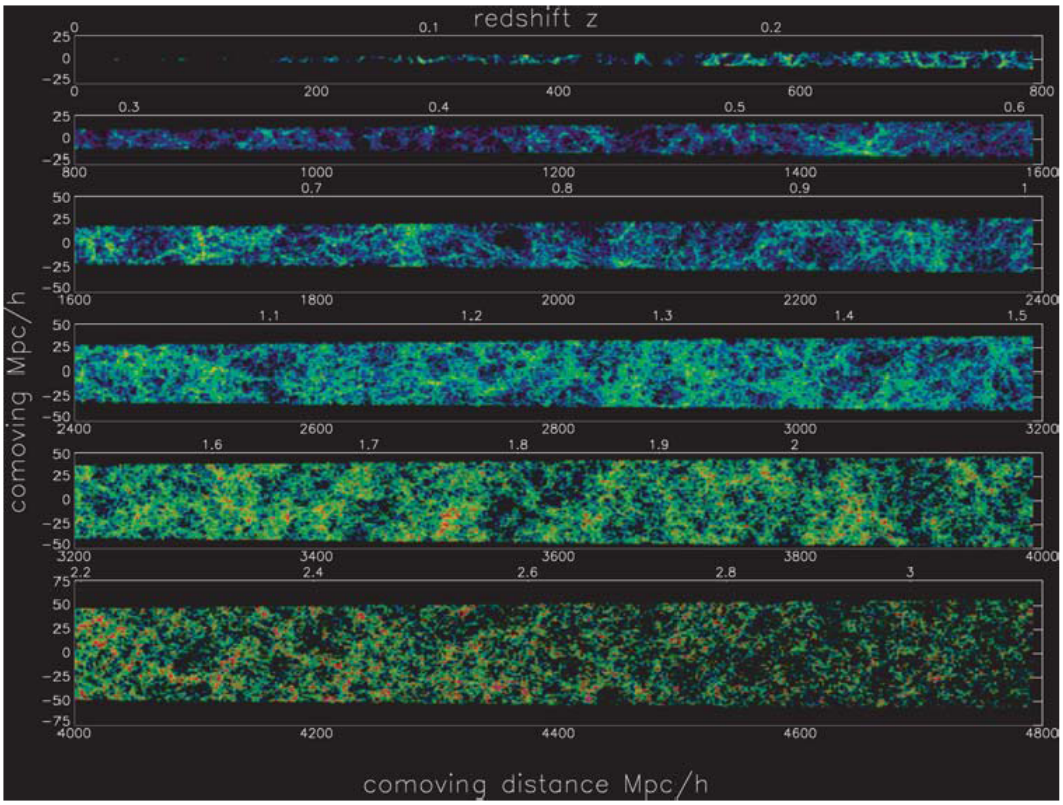

Figure 2.2: A mock survey with a field of view of 1.4×1.4 square degrees out to redshift $z = 3.2$ from Kitzbichler and White (2007). Galaxies brighter than an apparent magnitude of 24 in the K band are shown. The intensity relates to the logarithmic density and the colour to the offset from the evolving sequence.

The general case allowing for expansion and curvature would be significantly more complex to realise.

The data from the Millennium Simulation is stored at a number of discrete redshifts. The corresponding comoving distances between these data snapshots ranges from 80 to $240h^{-1}$Mpc which is equivalent to 100 to 380Myr. This means that the physical properties of the galaxies such as positions and velocities are only explicitly provided at the snapshot redshifts. Instead of interpolating these properties between snapshots Kitzbichler and White (2007) choose to use the properties defined at z_i for all galaxies that fall within the region spanning half the distance between the adjacent snapshots defined by the range $(D_i + D_{i+1})/2 > D > (D_i + D_{i-1})/2$ where D_i is the comoving distance to z_i. The reasoning behind this approach is that it preserves dynamically correct galaxy distribution which would be compromised by the interpolation technique due to the relative scales of orbital times and the spacing between snapshots. The physical properties of the galaxies are not offset by more than half of the time spacing between snapshots. A challenge with the method is that during the time between snapshots a single galaxy near to $(D_i + D_{i+1})/2$ or $(D_i + D_{i-1})/2$ may move across the boundary and therefore be accounted for twice or

not at all depending on the direction of its peculiar motion. To address this problem, linear interpolation is used to estimate the positions of galaxies near the boundaries at the redshift associated with $(D_i + D_{i+1})/2$.

The apparent magnitudes of the galaxies depend on both their physical properties and the redshifts at which they are observed. The magnitudes to be included in the galaxy catalogue, in this case Johnson B, V, R, I and K, are decided before running the semi-analytic code so that while the code is running, the magnitudes are stored for z_i as well as $z_i + 1$ and $z_i - 1$. The magnitudes are then linearly interpolated from the magnitudes at z_i and $z_i + 1$ or z_i and $z_i - 1$ according to the redshift at which the galaxy is observed in the mock survey which is only known after its construction. By storing the additional magnitude information during the semi-analytic simulation and then only later defining the mock surveys, Kitzbichler and White (2007) are able to produce multiple independent mock surveys (the number of which depends on the size of the field) for a single semi-analytic run.

Six different mock surveys are produced by Kitzbichler and White (2007) and made available on the Millennium Simulation database. Each mock survey represents a high redshift survey with a field of view of 1.4×1.4 square degrees. The effect of peculiar velocities that is being studied in this work is seen mainly at low redshifts and thus, only data out to a redshift of $z = 1$ is used. Figure 2.3 shows the galaxies up to redshift $z = 1$ for the six mock surveys labeled A to F.

The Kitzbichler and White (2007) mock surveys have data for the cosmological redshift of each galaxy. This is calculated using its distance from the observer which is provided in h^{-1}Mpc. In addition there is the redshift of the Millennium Simulation snapshot in which the galaxy appears, and the redshift from the observer's point of view which is affected by the peculiar velocities of the galaxies. The magnitude and direction of the radial component of the peculiar velocity is represented by the difference between the cosmological and observed redshifts. The left panel of Figure 2.4 shows the relationship between the snapshot and cosmological redshifts. The snapshots are taken at discrete predetermined redshifts as the simulation progresses with increasingly large gaps in between them. Within a snapshot the distance to the observer varies and that results in cosmological redshifts in between the snapshot redshifts. The right panel shows the percentage change in the observed redshifts compared with the cosmological redshifts for the galaxies in mock survey F.

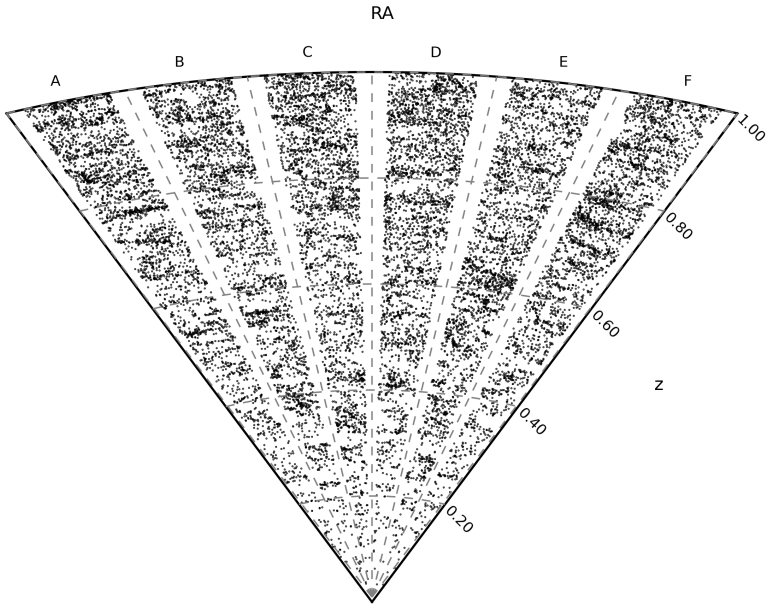

Figure 2.3: The six different mock surveys produced by Kitzbichler and White (2007) for the redshift range $z = 0 - 1$. 3000 galaxies are randomly selected from each mock survey to show the density variations and structure in the catalogues. The apparent elongation of some structures is an artefact of the scaling of the plot.

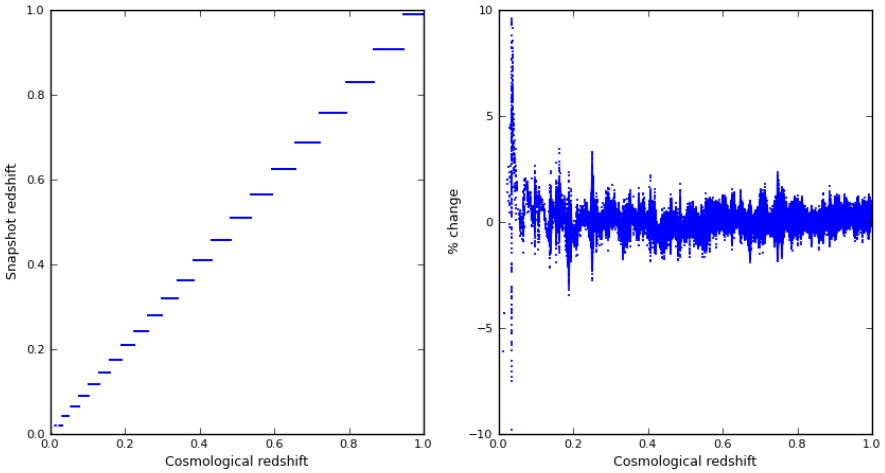

Figure 2.4: Relationships between the redshift data provided for mock survey F (Kitzbichler and White 2007). *Left:* The relationship between the calculated cosmological redshifts and the discrete snapshot redshifts associated with the Millennium Simulation. *Right:* The percentage change in cosmological redshift caused by peculiar velocities. The change decreases with increasing redshift as the peculiar velocities become much smaller relative to the recession velocities. A negative change indicates that the direction of the radial component of the peculiar velocity is away from the observer.

Table 2.1: Supernova rates by host galaxy colour in units of SNIa per century per 10^{10} $M_{\odot}$ (SNuM) from Mannucci et al. (2005).

B-K	SNuM
< 2.6	$0.86^{+0.45}_{-0.35}$
$2.6 - 3.3$	$0.19^{+0.08}_{-0.07}$
$3.3 - 4.1$	$0.084^{+0.026}_{-0.025}$
> 4.1	$0.027^{+0.017}_{-0.013}$

2.4 Supernova Rates

Supernova rates define the probability of a galaxy containing a supernova in a given time period. We use them to assign supernovae to objects in galaxy catalogues such as those of Kitzbichler and White (2007). The rates computed by Mannucci et al. (2005) take into account the physical properties of the galaxies, in particular their $B - K$ colour and stellar mass. They are given in units of SNuM which represents the number of SNIa per century per $10^{10}M_{\odot}$.

Mannucci et al. (2005) calculated their SNIa rates using 136 observed SNIa collected from the SNIa catalogues of five different groups. The original dataset was larger but they retained only those SNIa where the luminosity, colour, morphology, inclination and distance of the host galaxy could be identified. These selection criteria resulted in more than 100 objects being discarded. The galaxy properties were collected by cross correlating the 2MASS Extended Source Catalog, which gives the K-band near infrared magnitudes, with optical galaxy catalogues.

The colour of a galaxy is related to its star formation rate (SFR). Young stars appear bluer and therefore galaxies with active star formation appear bluer than those without star formation. In analysing the host galaxies of the 136 SNIa Mannucci et al. (2005) found that the rate of SNIa was noticeably different for galaxies of different colours. They define SNIa rates for four different bands of $B - K$ colour based on their findings as shown in Table 2.1.

In this work we use the rates of Mannucci et al. (2005) to generate simulated SNIa datasets for studying the impact of peculiar velocities on cosmological parameter estimation. Using the SNIa rates, and taking into consideration the colour and mass of each galaxy, we assign a probability that the galaxy will contain a SNIa. We then generate a random number and compare this to the probability in order to determine whether a galaxy has a SNIa allocated to it or not. The details of the generated SNIa catalogues are explained in Chapter 4.

Chapter 3

Analysis Methodology

With our simulated set of SNIa it is now possible to estimate the cosmological parameters, such as Ω_m and H_0, and quantitatively evaluate the effect of peculiar velocities on the results. The important quantities in the Hubble diagram are redshift and distance; sky position (RA and Dec) is not taken into account because of isotropy. As a result, combining SNIa from the six mock surveys is relatively simple. We simulate both a deep, narrow and a shallow, wide SNIa survey and combine them into a single dataset. This mimics the set up for modern SNIa surveys like the SN Legacy Survey combined with low redshift surveys such as the SN Factory.

Using the simulated SNIa data, parameter estimation was performed using CosmoMC* which is a Markov-Chain Monte Carlo engine designed specifically for exploring cosmological parameter space. The CosmoMC runs took approximately 24 weeks (4000 hours) of CPU time. The remainder of this chapter describes parameter estimation, the Markov-Chain Monte Carlo method, CosmoMC and the analysis undertaken in this work.

3.1 Parameter Estimation

Equations such as Equation 1.26 allow us to parameterise our model of cosmology so that it can be described using a number of parameters (Ω_m, Ω_k, H_0 etc). Parameter estimation is the process whereby we attempt to constrain the range of possible values for each parameter using observations of the Universe. This involves finding the values of each parameter that result in the best possible fit of the parameterised equation to observed data. A widely used test to evaluate the goodness of fit of a set of parameter values to uncorrelated data is the χ^2, or Chi Squared, test. The χ^2 test statistic is:

$$\chi^2(\theta_j) = \sum_{i=1}^{N} \frac{(D_i - f_i(\theta_j))^2}{\sigma_i^2} \tag{3.1}$$

*http://cosmologist.info/cosmomc/

where N is the number of data points, D_i is the data, σ_i is the uncertainty on the data, and f_i is the theoretical prediction of the model as a function of the parameters, θ_j, that we want to estimate. The statistic effectively sums the number of standard deviations σ_i between the theoretical model and the data at each point. The best fit parameter values are found by minimising the χ^2 statistic while varying the values of the parameters (Heavens 2009).

The likelihood, usually written as $\mathcal{L}(D|\theta)$, can also be used to evaluate goodness of fit and identify best fit parameter values through maximisation. In the case of uncorrelated data, $\mathcal{L}$ is related to χ^2 as:

$$\mathcal{L}(D|\theta) \propto \exp\left(\frac{-\chi^2(\theta)}{2}\right) \tag{3.2}$$

Where we have some idea about the feasible ranges for parameters it can reduce the computation time required for fitting by limiting the parameter space to be investigated. This prior knowledge about parameters can be folded into the calculation of a posterior probability using Bayes' Theorem. Bayes' Theorem defines the posterior in terms of the likelihood and priors which are probability distribution functions for the parameters based on our existing knowledge of a situation. Bayes' Theorem is:

$$P(\theta|D) = \frac{P(D|\theta)P(\theta)}{P(D)} \tag{3.3}$$

Here $P(\theta|D)$ is the posterior probability that we are looking to calculate, the probability of the theoretical model given the data. $P(D|\theta)$ is the likelihood, the probability of the data given the theory and we maximise this to estimate parameters. $P(\theta)$ includes the information about the priors and $P(D)$ is the Bayesian evidence which normalises the expression. The evidence is dependent only on the data so when maximising the posterior to estimate parameters it is constant and therefore does not play a role (Heavens 2009). The prior distributions, $P(\theta)$, are chosen based on existing knowledge about the parameters. In this work we use top-hat priors which define an allowable range for parameter values over which they have equal probability of occurring and outside of which there is a zero probability. The priors on parameters in this work are given in Section 3.2.2.

3.2 Markov-Chain Monte Carlo

Markov-Chain Monte Carlo (MCMC) is a sampling technique for exploring parameter spaces, particularly where they are multidimensional. This parameter estimation technique has been applied in astrophysics to analysis problems including estimating cosmologies from the CMB power spectrum (Dunkley et al. 2004, Resolution et al. 2007) and the detection of Sunyaev-Zel'dovich clusters in the primordial CMB (Slosar and Hobson 2003). MCMC has also been used for the reconstruction of the real-space power spectrum from 2dFGRS (Percival 2005) and investigations of primordial non-Gaussianity (Kim 2010).

The simplest and most common algorithm for constructing an MCMC sampler is the

Metropolis-Hastings algorithm. The algorithm generates a chain of steps known as a Markov chain. At step n, which corresponds to a state x_n, a candidate for the next state x' is selected according to proposal distributions for each parameter. The posterior is calculated for both x_n and x'. If the posterior at x' is greater than the current posterior then the step is accepted and $x_{n+1} = x'$. Otherwise, the probability of the step being accepted is equal to the ratio of the current and candidate posteriors. If the step is rejected then the chain remains at the same place such that $x_{n+1} = x_n$. Consequently, any step yielding a greater posterior probability is accepted. Where a step yields a lower posterior, the probability of the step being accepted is defined by how much worse a solution it represents than the current position. Allowing the chain to 'move uphill' helps to avoid becoming stuck in a local minimum.

The Markov chain records the state at the completion of each step or iteration, including when it remains unchanged (i.e. when $x_{n+1} = x_n$). This record of steps is called a Markov chain. After sufficient iterations the chain converges on a stationary or equilibrium distribution. This represents the posterior distribution of the quantity of interest. An infinite chain will always converge on the true posterior. In practice, convergence criteria are set to define the point at which to stop the chain. The distribution of the final chain indicates the best fit solution by the position of its peak and the uncertainty of this result by the spread around the peak.

In addition to the length of the chain, the proposal distributions for the parameters that are set by the user impact the speed and efficiency of convergence. If the proposal distributions are very wide then there will be a low rate of acceptance and the chain may remain at a single point for a long period of time. Conversely, narrow proposal distributions means that although acceptance rates are high, the movement around the parameter space is slow. Despite these apparent shortcomings, MCMC remains a powerful tool in cosmology. The CosmoMC tool (see Section 3.2.1) is a highly developed MCMC algorithm designed to explore cosmological parameter space. It has a number of optimisations beyond the standard Metropolis-Hastings algorithm which help to overcome the issues decribed above.

3.2.1 CosmoMC

CosmoMC is an MCMC sampler developed by Lewis and Bridle (2002) for cosmological parameter estimation. By default, it uses CAMB* which is a code for computing anisotropies in the microwave background (Lewis et al. 2000) and calculates theoretical CMB power spectra. However, CosmoMC can also be set up as a generic MCMC sampler without using CAMB. It also includes code for analysing the output chains to calculate result statistics and create plots of the estimated parameters.

It is recommended to use the MPI option in CosmoMC so that multiple MCMC chains can be run simultaneously until a stopping criterion is met. MPI, or Message Passing Interface, is a platform that enables parallel computing using a distributed memory model

*http://camb.info/

where communication is managed through the passing of messages between CPUs which are running different processes in parallel. The stopping criterion used in CosmoMC is the Gelman and Rubin R statistic; once this statistic reaches a user-defined value the chains are halted. The R statistic is defined as:

$$R = \frac{\text{variance of chain means}}{\text{mean of chain variances}} \tag{3.4}$$

The default convergence criterion is $R < 0.03$.

The specifics of a CosmoMC run are defined in the params.ini file. In particular we set:

- Parameter ranges: For each parameter it is necessary to specify the proposal distribution which defines the prior discussed in Section 3.1. This proposal distribution is defined by setting the centre of the distribution, the minimum and maximum of the allowed range, the starting width and the estimated standard deviation of the parameter. To fix a parameter the min, max and centre values are set to the desired value and the starting width and standard deviation are set to zero.

- Input data and priors: There are a number of flags indicating which input data to use in the parameter estimation. The available input data include CMB data, baryon acoustic oscillation data, SNIa data as well as data from clusters, Lyman-α results and HST results. There is also a flag to indicate whether or not to use a top-hat prior for the age of the Universe which forces it to be between 10 and 20 gigayears.

3.2.2 Configuration

Since our focus is solely on constraints from SNIa, we set up CosmoMC without CAMB. In the parameter estimation we adopt the age prior (10 Gyr $<$ age $<$ 20 Gyr as explained previously), and exclude all of the available input data except for SNIa, for which we use our own simulated SNIa results. By configuring CosmoMC like this, we compute the cosmological parameters using only the SNIa data that we generate, containing information on the redshift, distance modulus and its associated error for each SNIa.

In order to find the 'best-fit' normalisation of the Hubble diagram, and estimate the offsets caused by the simulated SNIa datasets, we configure CosmoMC so that it does not marginalise over H_0 during the parameter estimation.

We use the following parameter ranges (top-hat priors) for the varied parameters:

- $0.005 < \Omega_b h^2 < 0.1$
- $0.01 < \Omega_{dm} h^2 < 0.99$
- $-2 < w < 0$
- $0.5 < \theta < 10$

$\Omega_b h^2$ and $\Omega_{dm} h^2$ are the baryon and dark matter densities expressed in terms of h^2. w is the equation of state for dark energy. θ is the ratio of the sound horizon to the angular diameter

distance multiplied by 100; the default range is used for this parameter. We assume that the Universe has a flat geometry, and therefore Ω_k is set to zero.

The CosmoMC output includes a file containing the best fit values for the parameters and the standard deviation or error on the results. These values are given for the varied parameters and also for additional inferred parameters. The inferred parameters included in the output are the dark energy density parameter Ω_Λ, the Hubble constant today H_0, age in gigayears and Ω_m.

We use MPI to run parallel MCMC chains and check for convergence. Each CosmoMC run consists of three chains and the convergence criterion we set to the default setting of 0.03.

3.3 Approach

We use the results from the CosmoMC runs to calculate the effect of peculiar velocities on each of the parameters we are interested in. This is achieved by running two supernova datasets through the sampling engine. The redshift data in the first of these runs is the observed redshift while in the second it is the true cosmological redshift with the peculiar velocities removed. The two datasets use identical distance modulus information which has error and scatter added as explained in section 4.1.1. Then the resulting parameter estimates for the two CosmoMC runs are compared. The quantity of interest is the shift in the parameter values as a result of peculiar velocities. This is measured by the difference between the best fit estimate for a parameter using observed redshift and the estimate using cosmological redshift. Also of interest is the comparison of the estimated parameter values for both observed and cosmological redshifts with the fiducial values that underly in the Millennium Simulation.

Chapter 4

Results

This chapter presents the simulated SNIa data that were generated from the mock galaxy catalogues of Kitzbichler and White (2007) and the Hubble diagrams constructed from these data for the purpose of parameter estimation (Section 4.1). Also presented here are the results for evaluating the correlation in the data using the Durbin-Watson statistic (Section 4.2), and the comparison of estimated parameter values calculated with and without peculiar velocities (Section 4.3).

4.1 Simulated SNIa Data

We generate SNIa data by simulating a deep SNIa survey taking place over 5 years with six different pointings of a 2 square degree field of view. This is done by applying the SNIa rates described in Section 2.4 to the mock galaxy surveys constructed by Kitzbichler and White (2007).

As explained in Section 2.4 the SNIa rates are based on the colour of the host galaxy which is an indicator of the star formation rate. Mannucci et al. (2005) provide a rate of SNIa in each of four bands of $B-K$ colour ($B-K < 2.6$, $2.6 < B-K < 3.3$, $3.3 < B-K < 4.1$, $B-K > 4.1$). Figure 4.1 shows the colour-magnitude diagram of the galaxies in mock survey A and with the colour bands shown, and with stars indicating a random realisation of SNIa host galaxies generated using the Mannucci et al. (2005) SNIa rates. The bluer galaxies in the colour band $B-K < 2.6$ which have higher rates of star formation have the largest proportion of SNIa.

Figure 4.2 shows the simulated SNIa in the six mock galaxy surveys (A-F). The colours denote the direction of the peculiar velocity of the host galaxy for each SNIa. The overall motion of all the galaxies is away from the observer. However, the direction of the radial component of the peculiar velocity may be towards the observer, in which case the galaxy appears less redshifted than it should considering its distance, and is shown in the figure as a blue point. Conversely, if the radial component of the peculiar velocity is pointing away from the observer the galaxy appears more redshifted and is plotted in the figure as a red

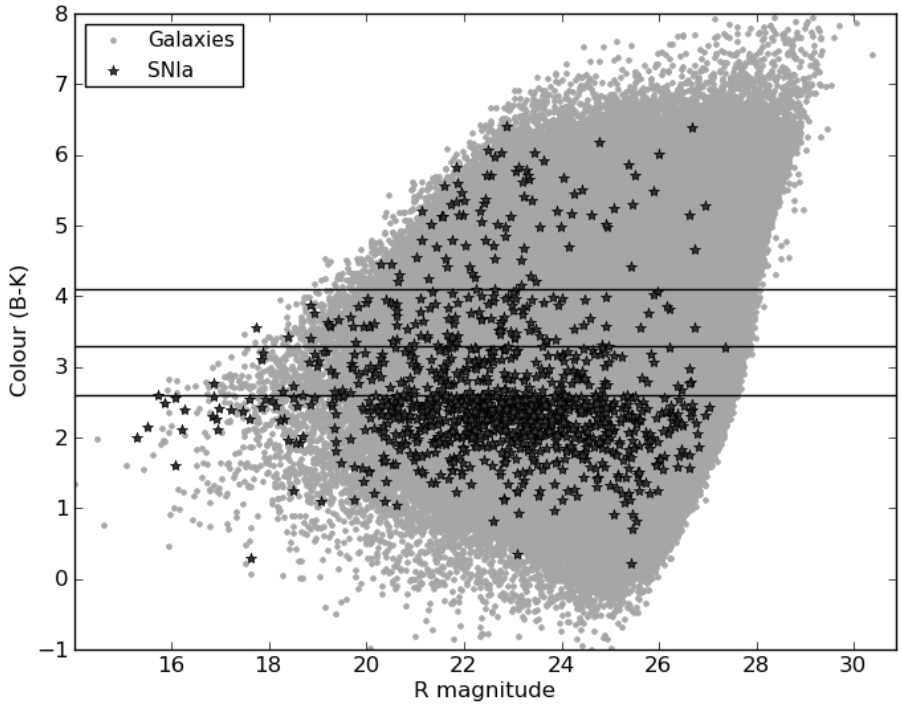

Figure 4.1: Colour-magnitude diagram of galaxies in mock survey A (Kitzbichler and White 2007) with those hosting SNIa indicated by stars. The SNIa host galaxies are determined by the application of the SNIa rates by Mannucci et al. (2005) and the horizontal lines mark the colour bands in which the rates are defined.

point.

In deep SNIa surveys, such as the SN Legacy Survey (Sullivan and Balland 2008), the time and equipment necessary to achieve the high redshift observations restricts the size of the field that can be observed. The narrow field of view and the cone shape of the observing beam mean that at low redshift a very small physical volume is covered and therefore few are SNIa observed.

In order to improve the coverage at low redshift, survey teams may conduct a wide shallow survey, like the SNFactory (Aldering et al. 2002), in conjunction with the narrow deep surveys. Observations out to redshift $z = 0.1$ can be undertaken by much smaller telescopes with larger fields of view and in shorter times and therefore can cover a significant area of the sky. We adopt this same approach since objects at low redshift, where peculiar velocities are more significant and correlations between them are more likely, are important in the study. We simulate an additional 5 year wide field survey out to redshift $z = 0.1$ by extracting the low redshift galaxies and adding SNIa to them using the rates from Mannucci et al. (2005) multiplied by 100. As in the deep survey, the SNIa come from the six mock galaxy surveys. Based on the assumption that the Universe is isotropic, we translate the

increase in the SNIa rates to an increase of the total field of view to 1200 square degrees (due to multiplication by 100). The wide survey contributes approximately 1000 additional SNIa which are shown in Figure 4.3. As in Figure 4.2, the colours of the datapoints indicate the effect of the peculiar velocities on the observed redshifts.

In a typical wide and shallow survey, a large area of the sky is observed and therefore the SNIa are spread out over large physical distances making their peculiar velocities less correlated. Our wide SNIa survey was simulated from the mock galaxy catalogues of Kitzbichler and White (2007) which comprise six pointings of a 2 square degree field. To simulate a larger survey covering $\sim$ 1200 square degrees we artificially increased the SNIa rates by a factor of 100 based on the assumption that the universe is isotropic. This assumption is reasonable in terms of the numbers of SNIa. However, although the six mock surveys can be considered independent from each other, the SNIa from each one are all within the same 2 square degrees instead of being distributed over hundreds of degrees as they would be in an actual wide survey. This means that the peculiar velocities will be more strongly correlated than in actual wide survey SNIa observations. Whilst the effect of this has minimal impact on our studies, the results should nevertheless be taken strictly as an upper bound on the effect of peculiar velocities.

The top panel of Figure 4.4 shows the change in redshift due to peculiar velocities computed as (z obs - z cos). A change of 0.01 in a nearby object may have a significant effect on the observed redshift. On the other hand, observations of more distant objects, such as those with a redshift close to $z = 1$ are less significantly affected by such a change in their redshift. The bottom panel shows the percentage changes in redshifts. The histogram of the percentage changes is much narrower due to the larger number of SNIa at high redshifts and has longer tails due to the few low redshift SNIa that are affected more dramatically. Although, in the plot, the range is restricted to $\pm$7%, there are objects where the change in redshift is as much as 18%.

The simulated SNIa from the deep survey (Figure 4.2) are shown again in Figure 4.5 but here, where the change in redshift is less that 5%, the SNIa are shown as small black points. As before, the colours denote the direction of the peculiar velocities. We see that the impact of peculiar velocities is more significant at low redshift as expected.

Multiple SNIa Realisations

We created three different realisations of SNIa by applying the SNIa rates to the galaxy catalogues three times, to simulate both deep and wide surveys. This means that there are three different sets of simulated SNIa taken from the same set of galaxies for studying the peculiar velocity effect. There are roughly the same number of SNIa in each realisation ($\sim$ 8800) and while there are some repeats, most of the galaxies associated with the SNIa vary across the realisations. Table 4.1 shows the number of SNIa from the deep and wide surveys for each of the three realisations. Table 4.2 provides a breakdown of the number of overlapping host galaxies in the three realisations. We expect many of the repeating galaxies to be at low redshift where the SNIa rates are artificially inflated by a factor of 100.

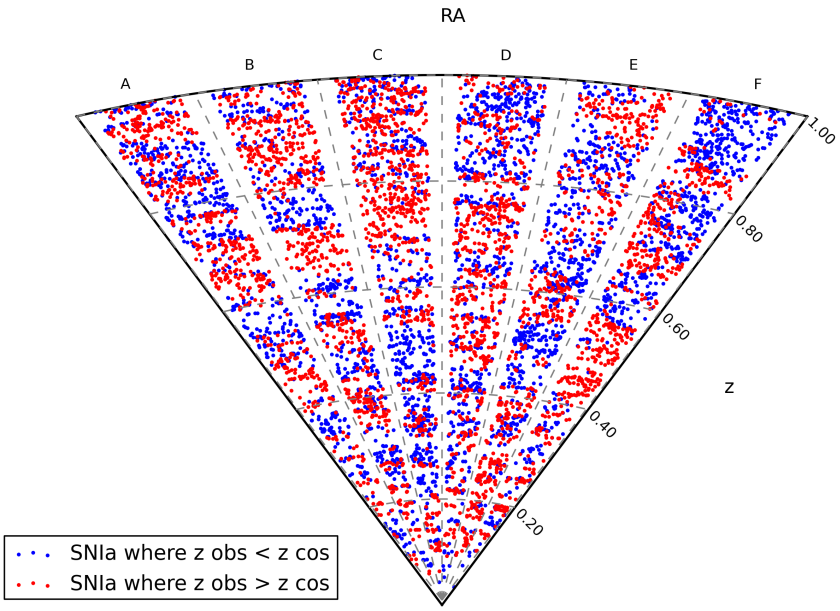

Figure 4.2: Simulated SNIa generated from the mock galaxy surveys of Kitzbichler and White (2007). The colours indicate the direction of the radial component of the host galaxy's peculiar velocity. The red points indicated reddened SNIa where the radial peculiar velocity is directed away from the observer so that the observed redshift is larger than the true redshift and similarly the blue points indicate blued SNIa.

Table 4.1: SNIa counts for the deep survey, wide survey and for the two surveys combined, for each of the three realisations.

Realisation	Number of SNIa		
	Deep survey	Wide survey	Combined
1	7382	1351	8733
2	7496	1368	8864
3	7512	1346	8858

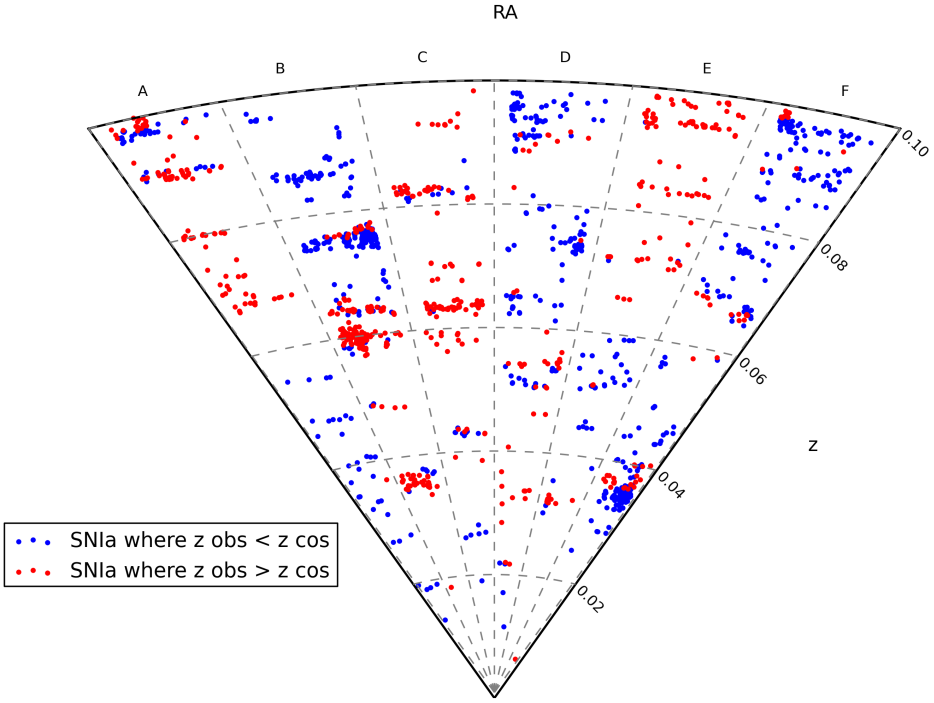

Figure 4.3: Simulated SNIa for a shallow, wide survey in the redshift range $z = 0 - 0.1$ and simulating an observed area of 1200 square degrees. As in Figure 4.2 the colours indicate the direction of the radial component of the host galaxy's peculiar velocity and thereby the effect on the observed redshift.

Table 4.2: Number of unique and overlapping SNIa in each realisation. The bold numbers in the diagonal represent the total number of SNIa in that realisation while the off-diagonal numbers give the amount of SNIa that appear in the two corresponding realisations. The unique row provides a count of SNIa that appear in only one realisation. (Note that the unique count is not simply a subtraction of the numbers of overlapping SNIa in the other two realisations since SNIa that appear in all three realisations need not be subtracted twice.)

Realisation	1	2	3
1	**8733**		
2	1232	**8864**	
3	1216	1226	**8858**
Unique	7186	7311	7280

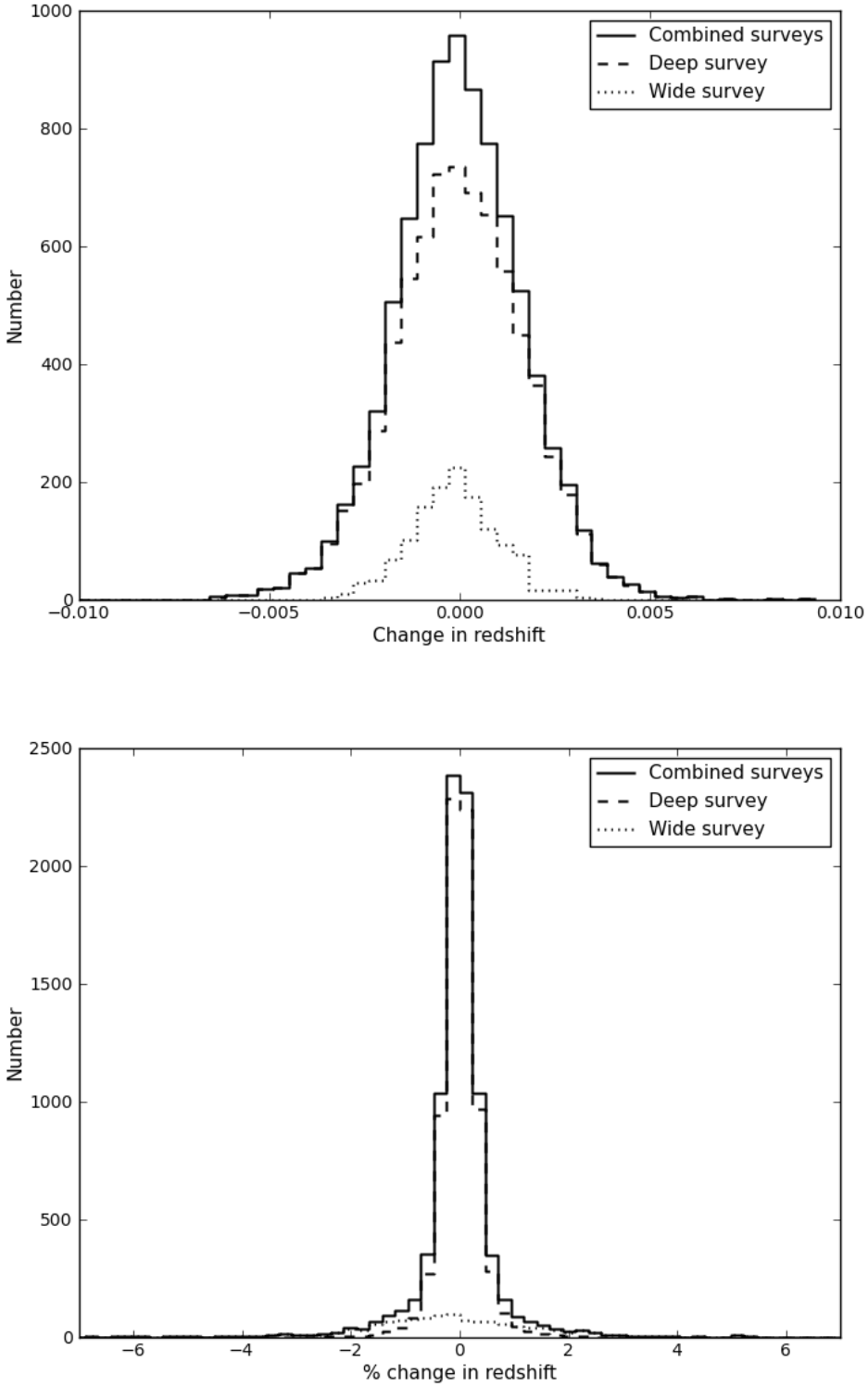

Figure 4.4: Histograms of the effects on redshift, from peculiar velocities, for SNIa from the simulated deep survey. A positive change indicates that the object appears more redshifted than it truly is and the peculiar velocity is directed away from the observer. *Top:* Change in redshift, which is computed as (z obs - z cos). *Bottom:* Percentage change in redshift, computed (z obs - z cos)/z cos.

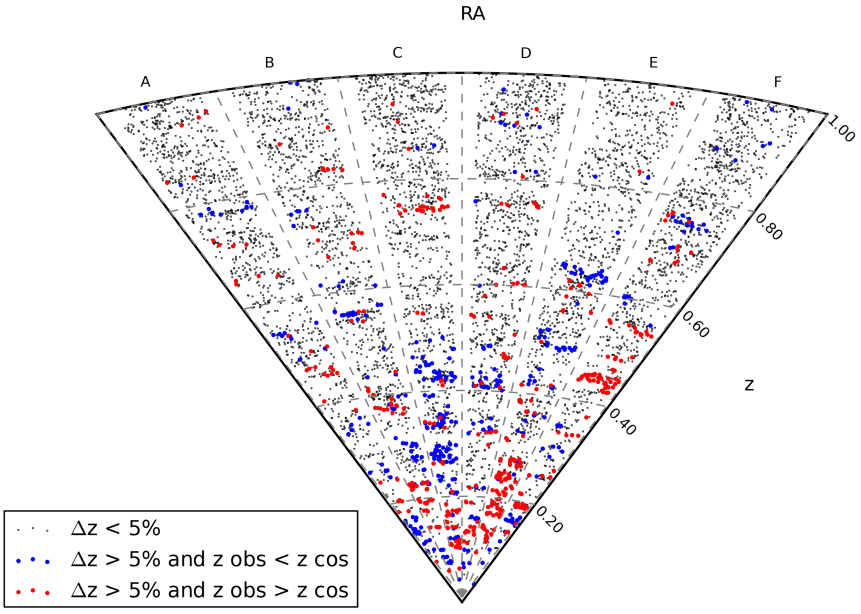

Figure 4.5: SNIa from the simulated deep survey (see Figure 4.2). Where the percentage change in redshift is greater than 5% the SNIa are shown in red and blue as in Figure 4.2, SNIa where the change in redshift is less than 5% are shown as small black points.

4.1.1 Constructing Hubble diagrams

SNIa data are used to construct Hubble diagrams from which we can calculate estimates of cosmological parameters. A Hubble diagram plots the redshifts of SNIa against their distance modulus which is calculated as:

$$\mu = 5\log(d_L) + 25 \tag{4.1}$$

where d_L is the luminosity distance as defined in Section 1.2, Equation 1.22. The luminosity distance is calculated using CosmoloPy*, a cosmology package for Python (Kramer 2011), which takes in the redshift and values for h, Ω_m, Ω_Λ and Ω_k. To calculate the distance modulus, we use the cosmological redshift and the parameter values corresponding to the Millennium Simulation for the other input variables (i.e. $h = 0.73$, $\Omega_m = 0.25$, $\Omega_\Lambda = 0.75$ and $\Omega_k = 0$).

Figure 4.6 zooms in on the low redshift region of the Hubble diagram plotted using the

*http://roban.github.com/CosmoloPy/

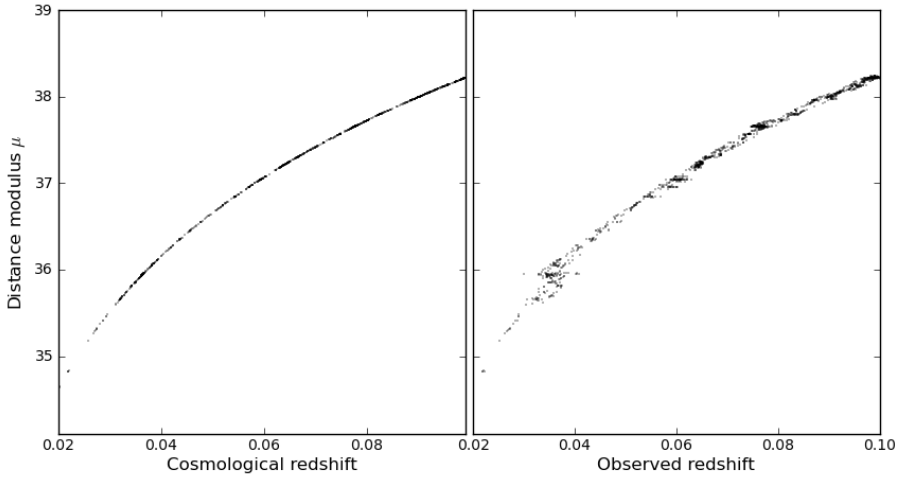

Figure 4.6: Hubble diagram in the range $z = 0.02 - 0.1$ for simulated SNIa data using cosmological redshift (*left*) and observed redshift (*right*). In this range the smudging of the redshift data as a result of peculiar velocities is evident in the observed redshift plot.

simulated SNIa with exact distance modulus data. In the left panel, where μ is plotted against cosmological redshift, we see a perfect representation of the relationship we used to calculate the distance modulus. In the right panel, we see the smudging of the observed redshifts as a result of peculiar velocities.

Since our galaxy data are simulated, the data is exact and, therefore, so are the calculated distance modulus values. However, in reality, SNIa observations have uncertainties associated with them. To make our Hubble diagrams more representative of observations we add typical error bars to the distance modulus and then scatter the calculated values within the range defined by these error bars.

We expect that SNIa peculiar velocity correlations will only be significant for future surveys. To consider the most extreme case, which maximises the effect of the correlations, we consider perfect photometric data and hence only consider errors corresponding to intrinsic scatter, uncorrelated peculiar velocities and redshift errors from spectroscopy. As such, we define the error on the distance modulus as:

$$\sigma_\mu^2 = (\sigma_\mu^{int})^2 + (\sigma_\mu^z)^2 \tag{4.2}$$

The intrinsic error, σ_μ^{int}, is due to the scatter in the peak magnitudes of SNIa that remains after the second order correction is applied as discussed in Section 1.4. This error is taken to be $\sigma_\mu^{int} = 0.16$ as in Kessler et al. (2009). The redshift error, σ_μ^z, is made up of a spectroscopic component and a peculiar velocity component. For the spectroscopic error Kessler et al. (2009) use $\sigma_{spec} = 0.0005$ where redshifts are based on host galaxy spectra and $\sigma_{spec} = 0.005$ for redshifts based on SNIa spectra. The peculiar velocity error is set to

$\sigma_{pec} = 0.0012$. This value is calculated by assuming typical peculiar velocities of 300km/s and typical internal motions of 200km/s. The redshift error should technically be an error in the x direction of the Hubble diagram, but it is generally projected onto the y axis as a distance modulus error using

$$\sigma_\mu^z = \sigma_z \left(\frac{5}{\ln 10} \right) \frac{1+z}{z(1+z/2)} \tag{4.3}$$

Kessler et al. (2009) include an additional error component, σ_μ^{fit}, to account for the statistical uncertainty of the fitting software MLCS2K2 used to calculate their distance modulus. This component is not included in this work since we assume perfect photometric data.

Figure 4.7 shows the SNIa data plotted with both the cosmological redshifts and the observed redshifts. The distance modulus data is scattered around the true values according to the error bars, and the error bars are shown. The shift in the Hubble diagram between the two redshifts is visible in places where the red points (observed) can be seen from behind the blue points (cosmological). The Hubble diagram bears a strong resemblance to that of Kessler et al. (2009) (Figure 1.6). The similarity of the shapes indicates that the cosmology underlying the Millennium Simulation is a good description of observations. More importantly, the similarity in the scatter on the data suggests that the simulated SNIa data is realistic when compared with actual observations. Appendix B shows a Hubble diagram of the simulated SNIa plotted over the same range as the one from Kessler et al. (2009) for comparison purposes.

Figure 4.8 shows the simulated SNIa on a Hubble diagram with arrows representing proportional change in redshift as a result of the peculiar velocities of the host galaxies. The scale of the arrows is vastly increased relative to the redshift axis, so they do not indicate numerical change in redshift, but rather give a qualitative indication of the peculiar velocity impact.

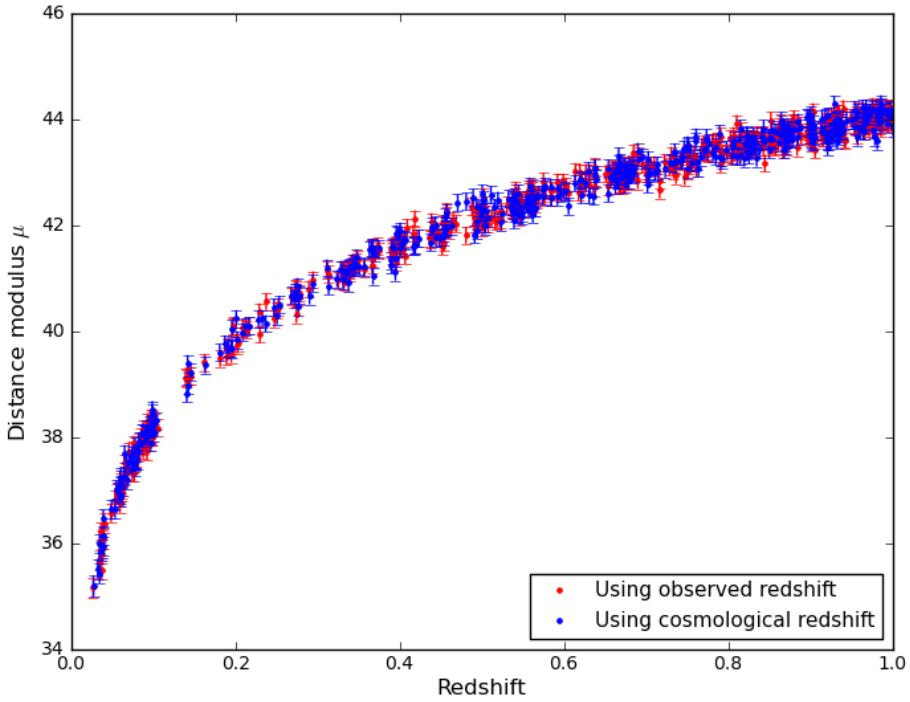

Figure 4.7: Hubble diagram constructed using simulated SNIa data with error bars and scattered distance modulus data. Each SNIa is plotted using its cosmological redshift (blue) and observed redshift (red) which is affected by the host galaxy's peculiar velocity. A random sample of the full SNIa dataset is shown here.

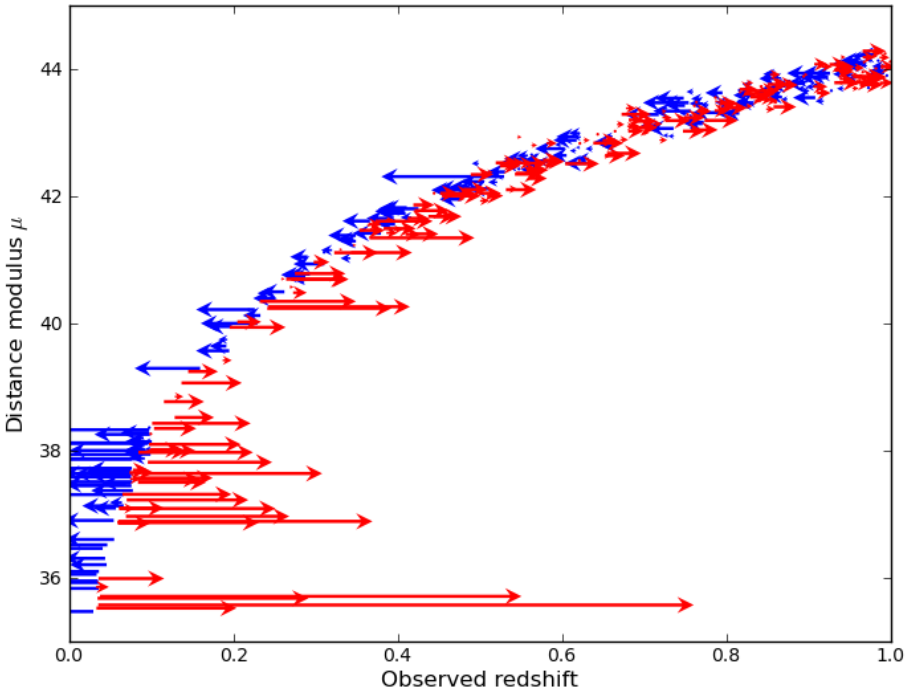

Figure 4.8: Hubble diagram of a random sample of SNIa, with arrows representing the proportional change in redshift as a result of peculiar velocities. Blue arrows are used where the SNIa appears less redshifted than expected and the red arrows where it appears more redshifted. The lengths of the arrows correspond to an arbitrary scale and only indicate the relative significance of the effects of the peculiar velocities. Their scale is not related to that of the redshift axis and they do not represent numerical changes in redshift.

4.2 Correlation

As discussed in Section 1.5, it is the correlations between peculiar velocities that determine their impact on cosmological calculations. The Durbin-Watson (DW) statistic provides a measure of autocorrelation in residuals of time series data (Durbin and Watson 1950a;b; 1971). The test statistic d is defined as:

$$d = \frac{\Sigma_{t=2}^{T}(e_t - e_{t-1})^2}{\Sigma_{t=1}^{T} e_t^2} \tag{4.4}$$

where T is the number of data points, and e represents the residuals. In general, a residual is the difference between the data value and the estimated value. In the case of our SNIa data, this is the difference between the distance modulus calculated using the true cosmological redshift, μ_{cos}, and the distance modulus calculated using the redshift measured by an observer, μ_{obs}, which is subject to error due to peculiar velocities:

$$e = \mu_{obs} - \mu_{cos} \tag{4.5}$$

The galaxy and SNIa catalogues are not time series data, therefore, we order the residuals in ascending order by their observed redshift for the computation of the DW statistic.

The DW statistic is always between 0 and 4. It is approximately equal to $2(1-r)$ where r is the autocorrelation between residuals. Therefore, a value of $d = 2$ indicates no correlation, $d < 2$ represents positive correlation and $d > 2$ represents anticorrelation.

The correlation for each of the six mock galaxy surveys is computed and shown in Figure 4.9 along with the correlation statistic for a sample of 5000 galaxies randomly drawn from all six mock surveys. Each mock survey A-F represents the observed galaxies from one pointing in the sky. Each pointing shows a high degree of correlation in peculiar velocities which is due to the relatively small volume probed by an observing beam of 2 square degrees, particularly at low redshift. By contrast, the peculiar velocities in the random galaxy sample are much less correlated. By combining observations taken in different parts of the sky, the correlation of the peculiar velocities is reduced.

In Figure 4.10, we compare the correlation of the three realisations of simulated SNIa from the deep survey with three random samples of galaxies containing approximately the same number of objects (7500). The simulated SNIa come from all six mock surveys combined and therefore they have a similar correlation to random samples of galaxies. We can use this result to reduce the effect of peculiar velocities on SNIa by combining data from observations in different parts of the sky.

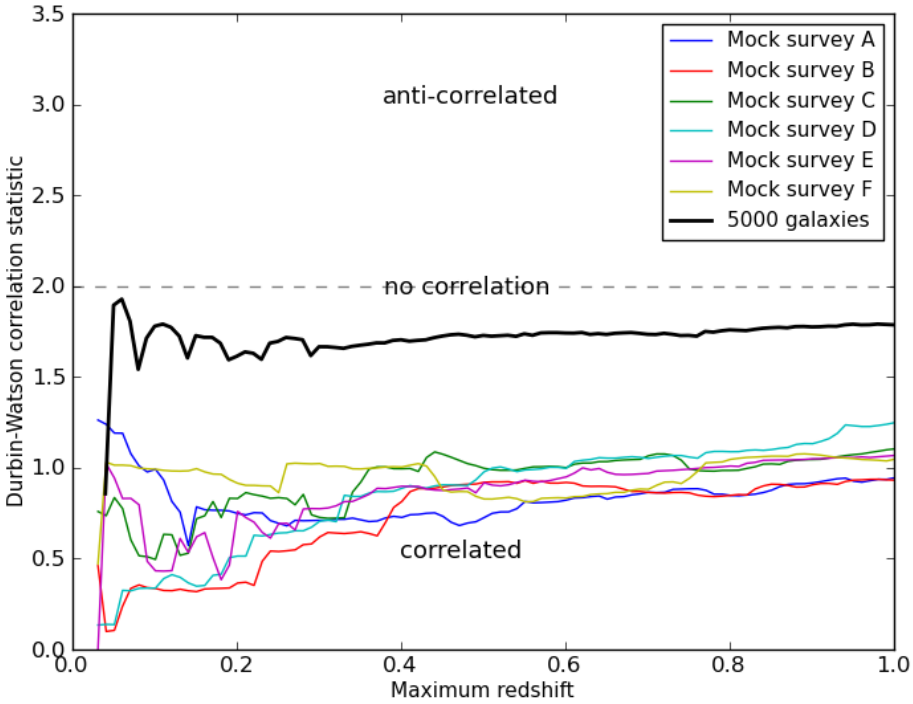

Figure 4.9: Correlation results for the full set of galaxies from each of the six mock surveys (A-F), and for a sample of 5000 galaxies drawn randomly from all six mock surveys. By combining the six different pointings and extracting a random sample the correlation of the peculiar velocities is significantly reduced.

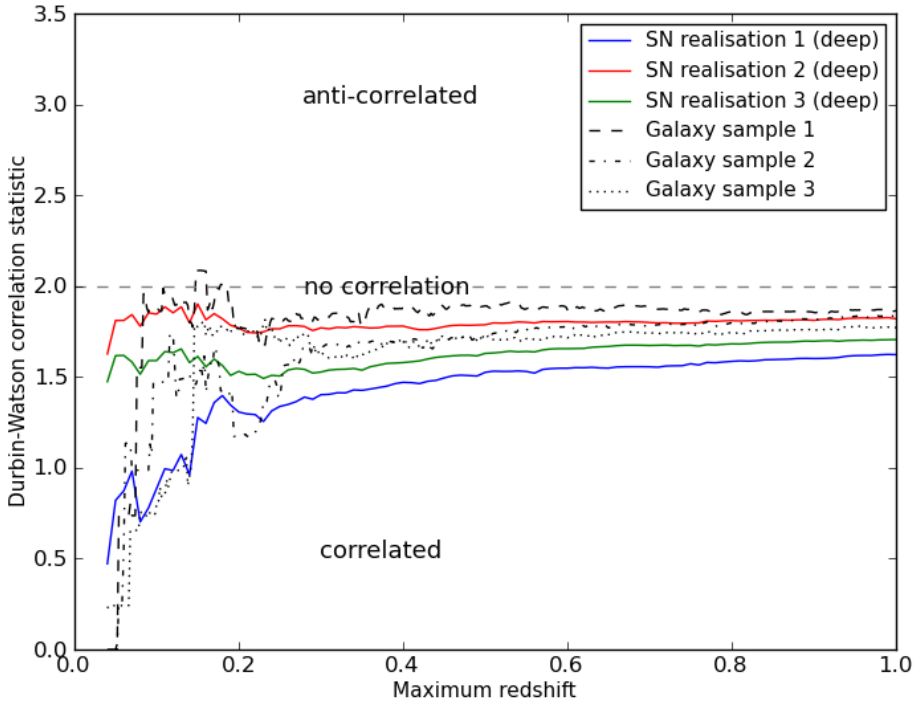

Figure 4.10: Durbin-Watson correlation statistic for the three realisations of simulated SNIa from the deep survey compared with the correlation of three random galaxy samples containing roughly the same numbers of objects. The SNIa show a similar level of correlation to the random galaxy samples.

When the SNIa from the simulated wide survey are added the correlation increases as seen in Figure 4.11, which shows the correlation of the combined deep and wide surveys for each of the three SNIa realisations and of three random samples of galaxies containing roughly the same numbers of objects and with a similar redshift distribution (i.e. 7500 from the full redshift range and an additional 1300 from redshifts $z = 0 - 0.1$). The increased correlation is solely due to the addition of SNIa from the simulated wide, shallow survey. At low redshift SNIa are more likely to be correlated since they are physically closer together. However, as explained in detail in Section 4.1, the simulated SNIa from the wide survey are overcorrelated because the galaxies used in generating them are from narrow mock survey catalogues. We see the effect of this overcorrelation if we compare the DW statistic in the range $z = 0$ to $z = 0.1$ in Figures 4.10 and 4.11. As a result of this overcorrelation, the subsequent results should be considered as an upper bound on the significance of the contamination effect of peculiar velocities.

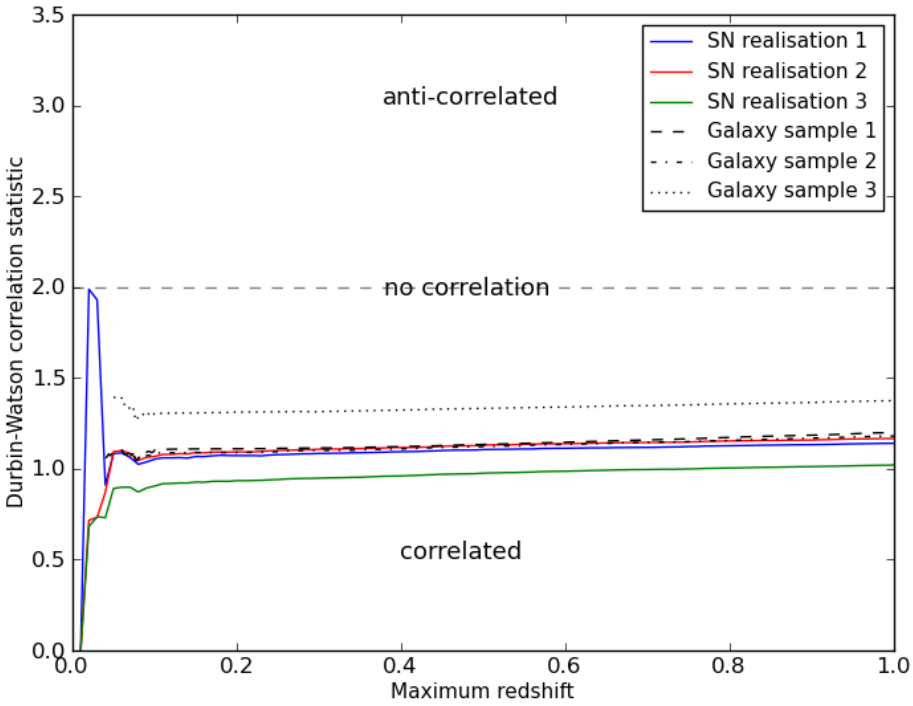

Figure 4.11: Durbin-Watson correlation statistic for simulated SNIa data from the combined deep and wide surveys, and compared with the correlation of three random galaxy samples containing the same numbers of objects. The addition of the low redshift SNIa increases the correlation substantially and since the correlation is computed cumulatively, this affects the DW statistic of the full SNIa sample.

4.3 Inaccuracies in Estimated Parameters

The peculiar velocity effect is measured by comparing the parameter estimates obtained using cosmological redshifts with those obtained using observed redshifts of the SNIa. The estimated parameters are also compared with the fiducial parameter values that underly the Millennium Simulation. We vary the maximum allowed redshift in the SNIa data to see the effect it has on the impact of peculiar velocities. We impose redshift cuts at $z = 0.05$, 0.08, 0.1, 0.2, 0.3, 0.4, 0.5, 0.6, 0.7, 0.8, 0.9 and 1. A redshift cut of 1 corresponds to using the full SNIa dataset since that is the limit of the mock galaxy surveys.

For each scenario, we use the three realisations of simulated SNIa and apply two different random scatters to the distance modulus data to create six different datasets. The distance modulus data is scattered around the true value based on the (Gaussian) error bars on the points. We estimate the cosmological parameters for all six datasets and, therefore, we get an indication of the range of outcomes. The computation involves running CosmoMC parameter estimation using cosmological redshifts and again using observed redshifts for each dataset so that the resulting parameter values can be compared. The comparison gives the shift in the parameter values due solely to the correlated peculiar velocities of SNIa host galaxies. The uncorrelated peculiar velocity effects are already folded into the SNIa error bars.

In the top panels of Figures 4.12 to 4.18 (and both panels of Figure 4.16), we show the average shift due to peculiar velocities, which is the average shift for the CosmoMC runs of the six different versions of the dataset (two scatters for each of the three SNIa realisations). The shaded bars do not represent individual error bars, they simply indicate the range of shifts computed for the six CosmoMC runs. The top and bottom of the shaded bar coincide with the maximum and minimum of the calculated shifts and the shifts calculated from the rest of the six runs lie inside the bar. Zero corresponds to the situation where the estimated parameter value calculated using observed redshifts is exactly equal to the estimated value calculated using cosmological redshifts.

In the bottom panels of Figures 4.12 to 4.18 (excluding Figure 4.16, the actual calculated values of the parameters are shown. The shaded and hatched bars represent the range of values computed for the six runs. The average estimated parameter values are shown as right or left pointing triangles, and the fiducial parameter value underlying the Millennium Simulation is indicated by the solid line. The difference between the average parameter estimates (left and right pointing triangles) corresponds to the average shifts plotted in the shift plots.

In order to assess the significance of the shifts and the accuracy of the calculated values, we compare them to the errors on the parameters given in the CosmoMC output. To make this comparison, the average size of the 1σ errors on the estimated parameters is indicated by the stepped contours. The average errors are shown around the zero line (shift plots, e.g. top panel of Figure 4.12) or the fiducial value (estimated value plots, e.g. bottom panel of Figure 4.12) to provide context to the results. The errors should strictly be shown individually

around each data point, however, this would make the figures extremely cluttered.

4.3.1 The Peculiar Velocity Effect on Ω_m

The top panel of Figure 4.12 shows the shifts in Ω_m for the different maximum redshift cuts. The shifts represent the change in the value of the parameter because of peculiar velocities, however, the accuracy of the parameter estimates compared to the fiducial value is not considered. In the bottom panel of Figure 4.12 the estimated Ω_m values are compared with the fiducial value of $\Omega_m = 0.25$.

The shift in Ω_m caused by peculiar velocities is almost exclusively less than the 1σ error on the estimated value. This makes the shifts statistically insignificant.

The ranges of estimated Ω_m values (bottom panel of Figure 4.12) for the two different redshifts are very similar. In some cases the average parameter estimate using observed redshifts is nearer to the fiducial value than when cosmological redshifts are used.

In general it appears that for samples with lower maximum redshifts, the observed redshifts result in a higher value for Ω_m than the cosmological redshifts. Conversely, for those that contain SNIa to higher redshifts, the observed redshifts produce a lower Ω_m than the cosmological redshifts. When we exclude SNIa above $z = 0.4$, the estimated value for Ω_m is higher than the fiducial value, in some cases of the order of 1σ. In contrast, once SNIa above $z = 0.4$ are included the calculated values tend to underestimate the fiducial value of Ω_m, which may be the result of CosmoMC overcompensating for the low redshift effect by changing the shape of the Hubble diagram at higher redshifts.

4.3.2 The Peculiar Velocity Effect on H_0

The top panel of Figure 4.13 displays the shifts in H_0 due to correlated peculiar velocities, and the bottom panel shows the estimated H_0 values compared with the fiducial value of $H_0 = 73$ that underlies the Millennium Simulation.

The sizes of the shifts in H_0 are approximately equal to the 1σ error bars on the parameter estimation. The value of H_0 is determined by low redshift SNIa and therefore it is more sensitive to the effect of correlated peculiar velocities, and adding large numbers of (uncorrelated) high redshift SNIa will have little impact on correcting for the low redshift inaccuracies. We see this in the top panel of Figure 4.13 where, for a maximum redshift cut of $z = 0.5$ and above the shift in H_0 is constant.

The calculations using observed redshifts consistently underestimate the value of H_0. The values computed using the cosmological redshifts fall just inside the 1σ error bars from the parameter estimation, while those computed using observed redshifts are generally about 2σ away from the fiducial H_0 value.

The effect on H_0 is greater than it is on Ω_m. This is expected, since H_0 estimates are based on low redshift SNIa data and, therefore, are more sensitive to correlations at low redshifts. The 2σ impact on the accuracy of H_0 is strictly an upper bound.

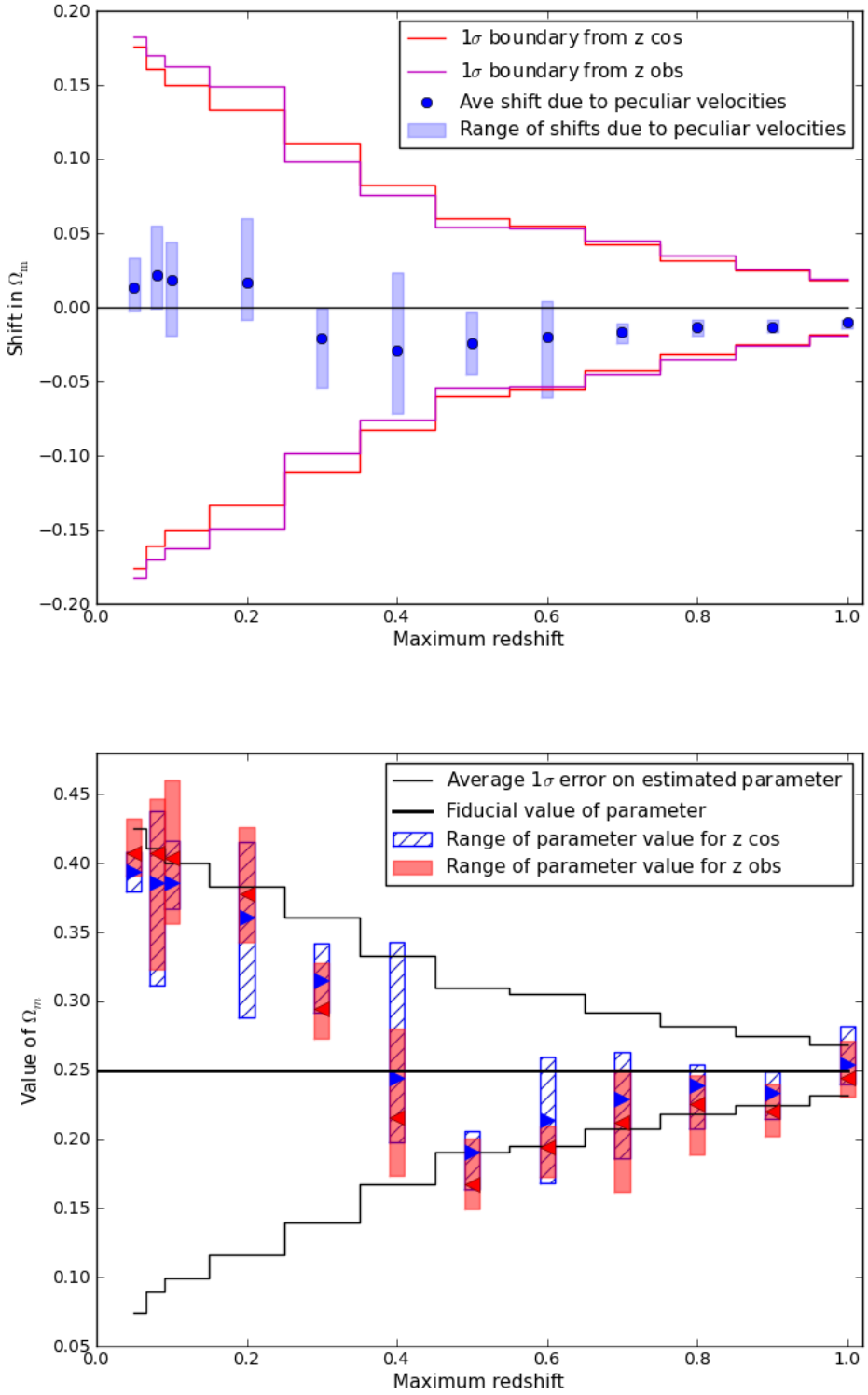

Figure 4.12: *Top:* Shifts in values of Ω_m calculated using observed and cosmological redshifts for various maximum redshift cuts. The change in Ω_m due to correlated peculiar velocities is not statistically significant as it is generally less than the 1σ error from the CosmoMC parameter estimation. *Bottom:* The ranges of estimated values for Ω_m calculated using observed redshifts (red, shaded bars) and cosmological redshifts (blue, hatched bars). The estimated values are, on average, within 1σ of the fiducial value. In some cases the estimates differ by up to 2σ from $\Omega_m = 0.25$, however, this is consistent with the expected rate from sample variance and hence not significant.

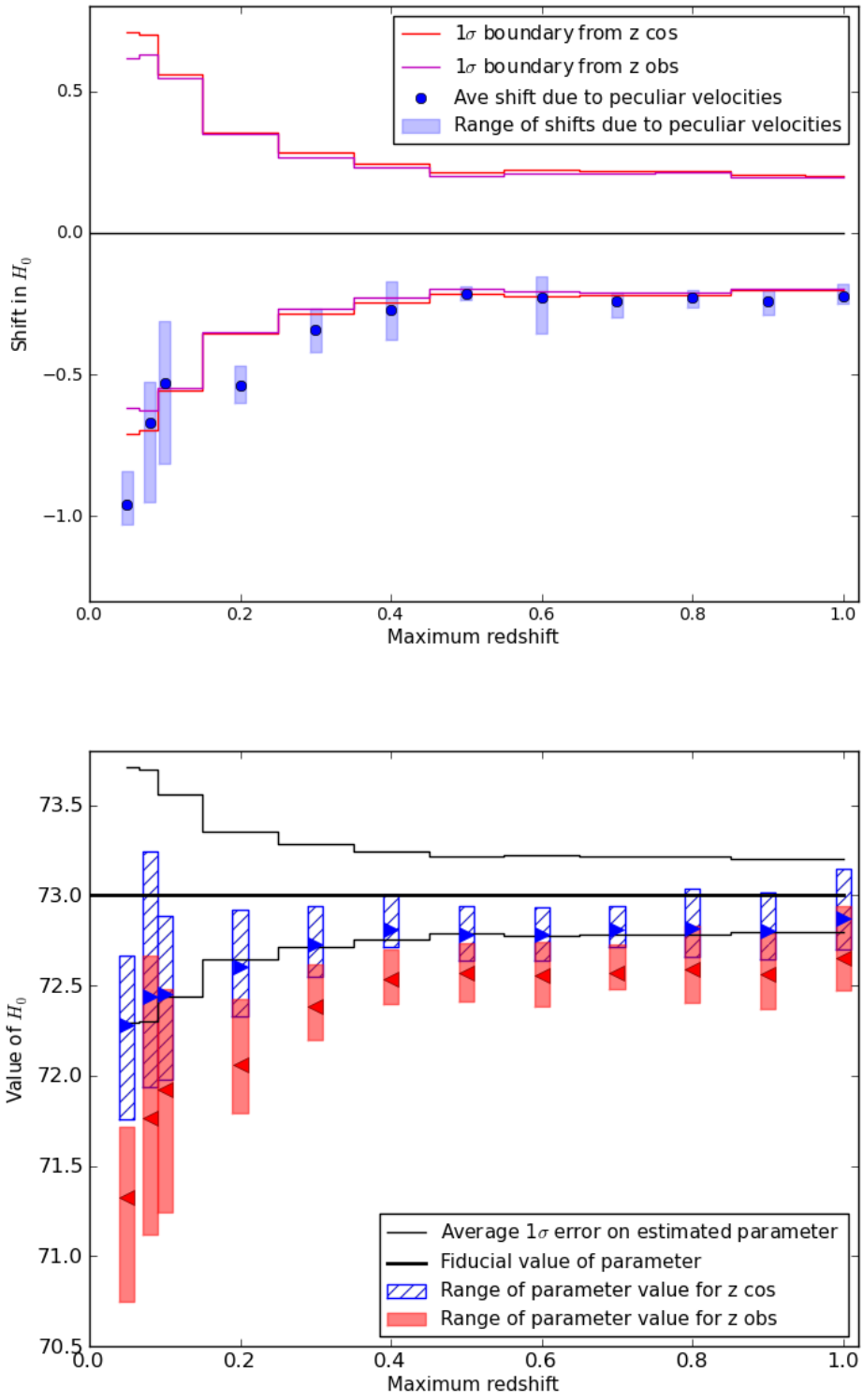

Figure 4.13: *Top:* Shifts in values of H_0 calculated using observed and cosmological redshifts for various maximum redshift cuts. The correlated peculiar velocities result in shifts of $\sim 1\sigma$ when using observed redshifts compared with cosmological redshifts. *Bottom:* The ranges of estimated values for H_0 calculated using observed redshifts (red, shaded bars) and cosmological redshifts (blue, hatched bars). Using the observed redshifts the calculated H_0 consistently underestimates the fiducial value ($H_0 = 73$) by $\sim 2\sigma$.

4.3.3 The Effect of Imposing a Minimum Redshift Cut

Since we know that the effect of peculiar velocities is most significant at low redshifts, we can try to reduce the effect by excluding low redshift SNIa from our analysis. As previously mentioned, it is common to exclude SNIa below $z = 0.02$ with this in mind (Davis et al. 2010). There is a trade off in this because we lose data at low redshifts which will affect the fitting of the low redshift end of the Hubble diagram.

To investigate how much this technique actually improves our parameter estimates and the appropriate minimum redshift cut to impose, we calculate the effect of the peculiar velocities on Ω_m and H_0 using minimum redshift cuts at $z = 0.02$, 0.05, 0.08, 0.1 and 0.2. Parameter estimation with the full SNIa datasets, which corresponds to a minimum redshift cut at $z = 0$ is also included for comparison, and this corresponds to a maximum redshift of $z = 1$ in Figure 4.12 and 4.13.

Figures 4.14 and 4.15 show the shifts in the estimates and the actual parameter estimates compared to the fiducial values for Ω_m and H_0 respectively.

Most of the shifts and parameter estimates in these results are within the 1σ errors. At worst, there are some parameter estimates that are out by 2σ. Statistically we expect variations of this nature, therefore, the relationships observed may simply be the result of intrinsic uncertainties in the parameter estimation process.

It is nevertheless interesting to note that, with the exception of the cut at $z = 0.02$ which seems to have little effect, the minimum redshift cuts noticeably reduce the shifts of both parameters to lie comfortably within the 1σ range (top panels of Figures 4.14 and 4.15). The lower panels of the figures suggest that minimum redshifts cuts at $z = 0.1$ and higher will compromise the accuracy of the parameter estimation, and therefore should be avoided. Comparing the shifts and the estimated values of the two parameters, we see possible evidence of the trade off between reducing the peculiar velocity effect and losing valuable input data. Based on these data and results, a cut of $z = 0.05$ appears to be the best choice for a minimum redshift cut. At this minimum redshift the effect of the correlated peculiar velocities are is very small without causing a loss of accuracy in the parameter estimation.

4.3.4 Investigating a Possible Bias in the Observed Redshift Data

We would expect the average shift in a parameter to approach zero as the number of SNIa increases. However, this is not what we see in the top panels of Figures 4.12 and 4.13, where the average shifts in both Ω_m and H_0 appear to stabilise at a constant negative value (i.e. where the parameter calculated using observed redshifts is less than when using cosmological redshifts).

A possible explanation is the presence of a global bias in the observed redshift data. We investigate this possibility by calculating the average difference between observed and cosmological redshifts and subtracting this from the observed redshift. Figure 4.16 shows the shifts in Ω_m and H_0 when these normalised observed redshifts are used.

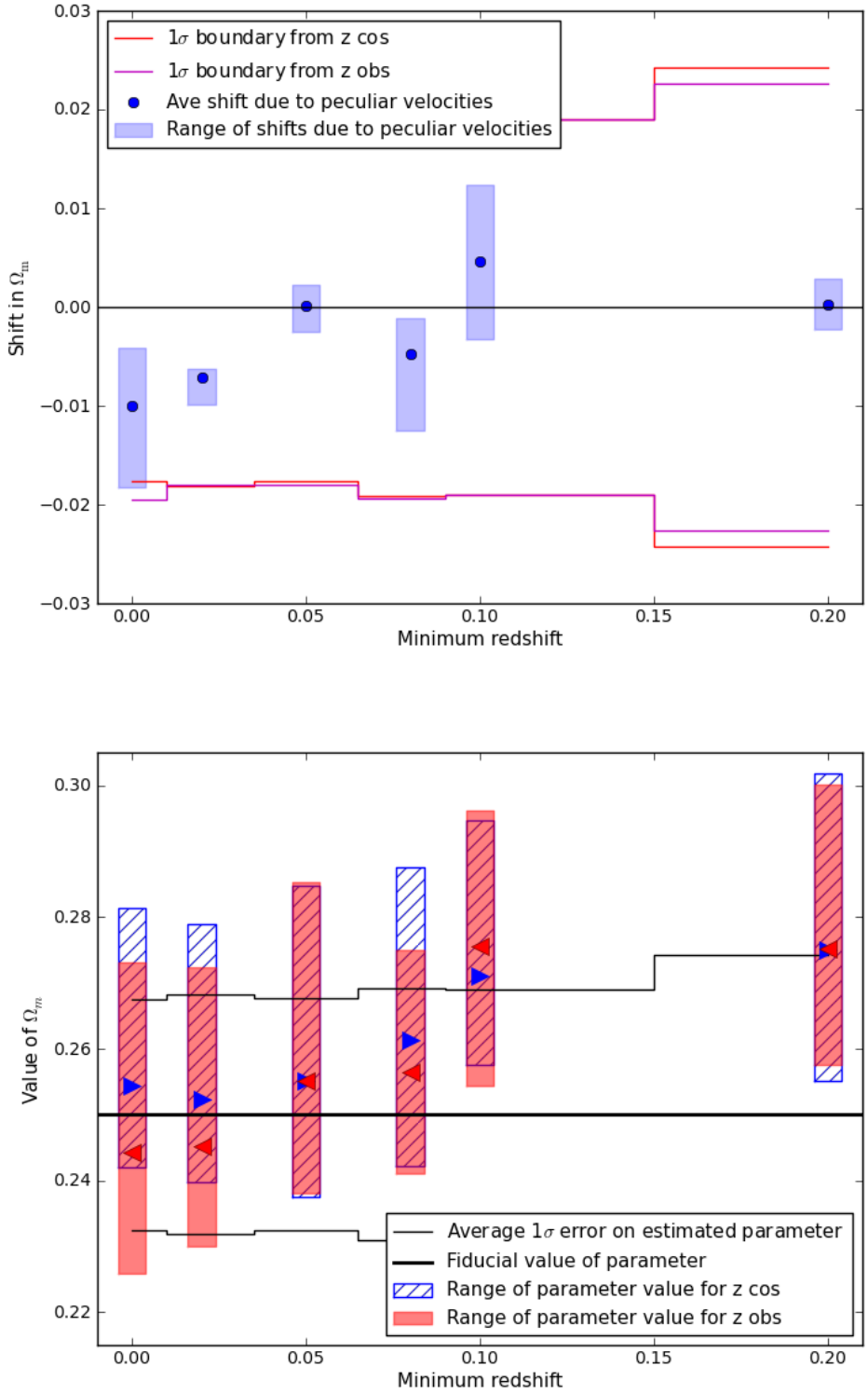

Figure 4.14: *Top:* Shifts in values of Ω_m calculated using observed and cosmological redshifts for various minimum redshift cuts. The cuts reduce the shift in the parameter value caused by peculiar velocities. *Bottom:* Estimated values for Ω_m calculated using observed redshifts (red, shaded bars) and cosmological redshifts (blue, hatched bars) for different minimum redshift cuts. The results are generally consistent with the fiducial value but appear to become less accurate as the minimum allowed redshift increases to $z = 0.1$ and above.

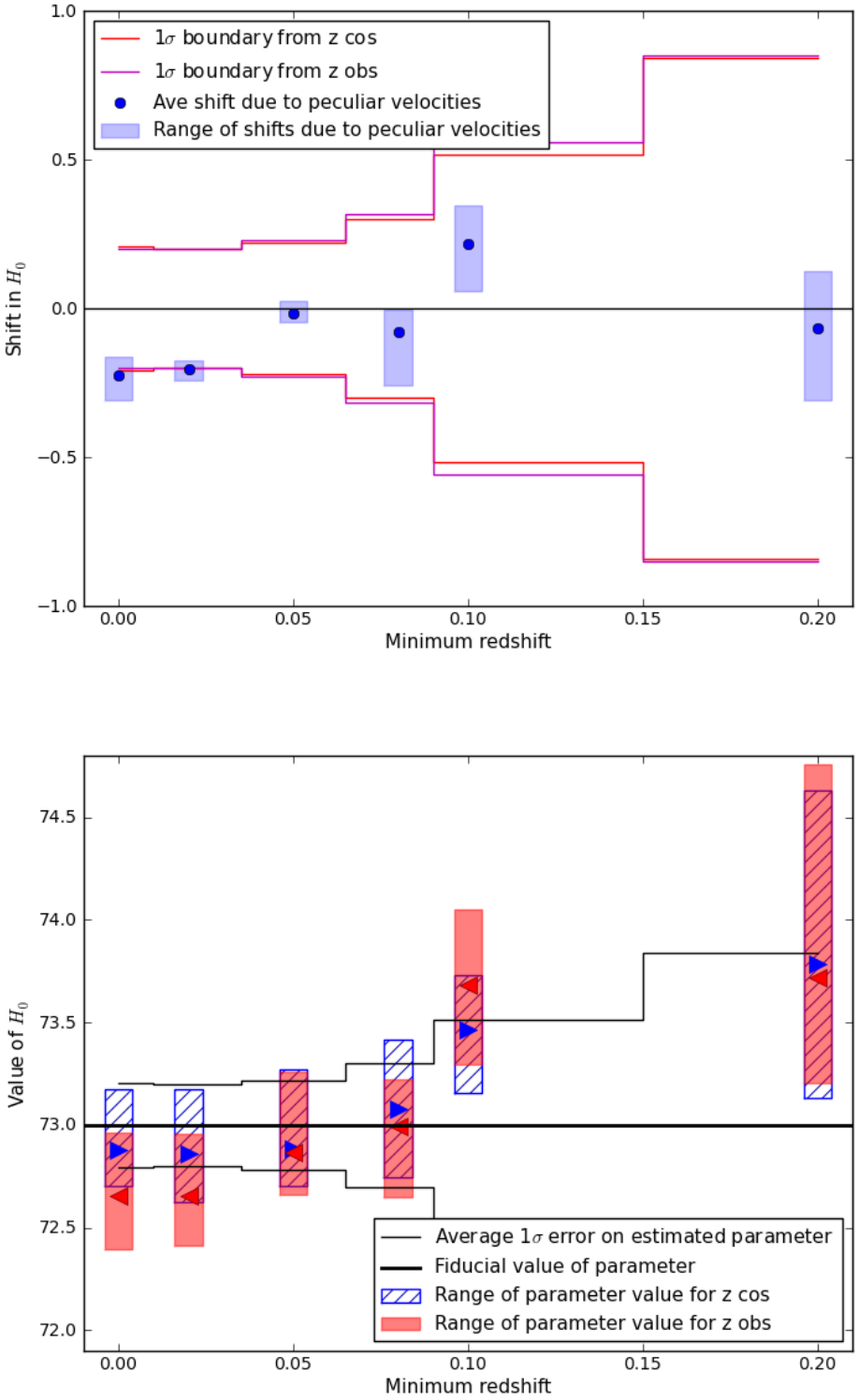

Figure 4.15: *Top:* Shifts in values of H_0 calculated using observed and cosmological redshifts for various minimum redshift cuts. Cuts at $z = 0.05$ and above noticeably improve the average shift in H_0. *Bottom:* Estimated values for H_0 calculated using observed redshifts (red, shaded bars) and cosmological redshifts (blue, hatched bars). Once again, it appears that as the minimum allowed redshift increases, the accuracy of the estimated values is negatively affected.

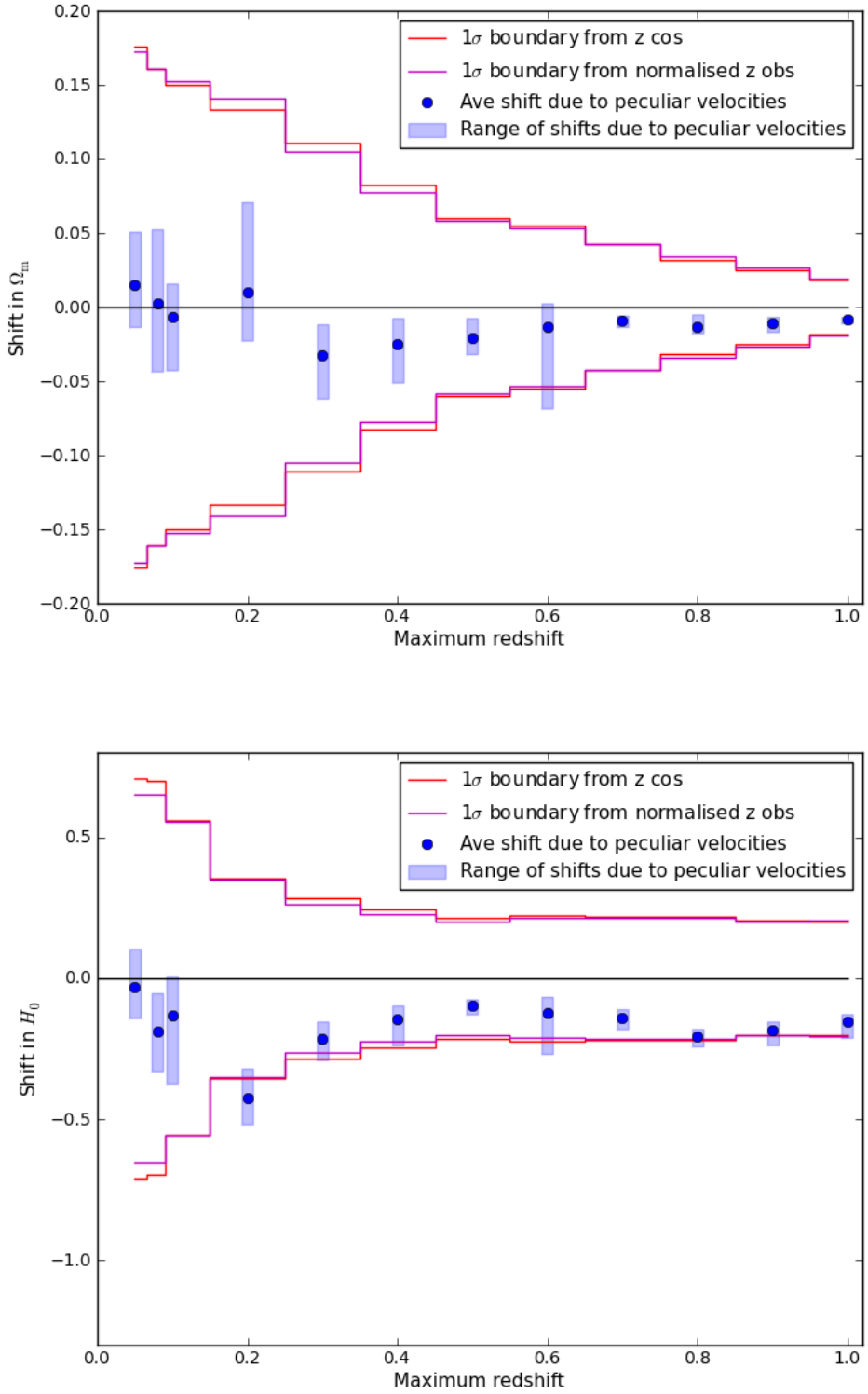

Figure 4.16: Shifts in calculated values of Ω_m *(top)* and H_0 *(bottom)* for various maximum redshift cuts and using normalised observed redshifts (i.e. where the difference between observed and cosmological redshifts is reduced by the average difference in the dataset). The normalising of the observed redshifts has very little effect on Ω_m and does not improve the shifts in H_0 significantly, which suggests that the data is not biased.

As calculated when using the standard observed redshifts, the shifts in the parameters still do not appear to approach zero. In fact, for Ω_m the shifts look remarkably similar to the ones in Figure 4.12. The shifts in H_0 are different to those in Figure 4.13 but not systematically so, and there is still a shift of $\sim 1\sigma$ out to redshift $z = 1$. From this we can conclude that there is not a global bias in the observed redshift data.

A more likely explanation for the apparent bias in the shifts of Ω_m and H_0 is that the low redshift SNIa, which are most correlated, result in an incorrect estimate of H_0. The value of H_0 is determined by the low redshift objects and therefore increasing the maximum redshift and adding more high redshift SNIa does not remove the bias created by the correlations in the peculiar velocities. The bias in H_0 then propagates to Ω_m and results in a bias on this parameter too.

4.3.5 Parameter Estimation using Exact Distance Modulus

In addition to the peculiar velocities affecting the resulting cosmology, the scatter that is added to the distance modulus data will cause variations in the estimated parameters from one CosmoMC run to the next. To isolate the impact of the peculiar velocities we compute the parameters using exact distance modulus data calculated from cosmological redshifts of the SNIa. The errors on the distance modulus data are kept the same as before. The resulting shifts and estimated values for Ω_m and H_0 are shown in Figures 4.17 and 4.18.

Removing the scatter from the distance modulus data has almost no effect on the shifts in the estimated values of Ω_m and H_0 when calculated using observed redshifts compared with cosmological redshifts. This is expected since the shifts are due to the differences in the observed and cosmological redshifts resulting from peculiar velocities.

The effect of removing the scatter is clearly visible in the bottom panels of Figures 4.17 and 4.18 which plot the estimated values of Ω_m and H_0 calculated using observed and cosmological redshifts. There is much less spread in the estimated parameter values, particularly when using cosmological redshifts. Using only very nearby SNIa (up to $z = 0.1$), Ω_m is overestimated by about 1σ as before, and H_0 is underestimated as before although to a lesser degree. For both parameters, once the maximum redshift reaches $z = 0.5$ the estimated values are almost exact when using cosmological redshift. The estimates using observed redshifts are shifted as before: for Ω_m to higher values initially and then to lower values from a maximum redshift of $z = 0.3$ upwards, and for H_0 to lower parameter values even for the full SNIa datasets.

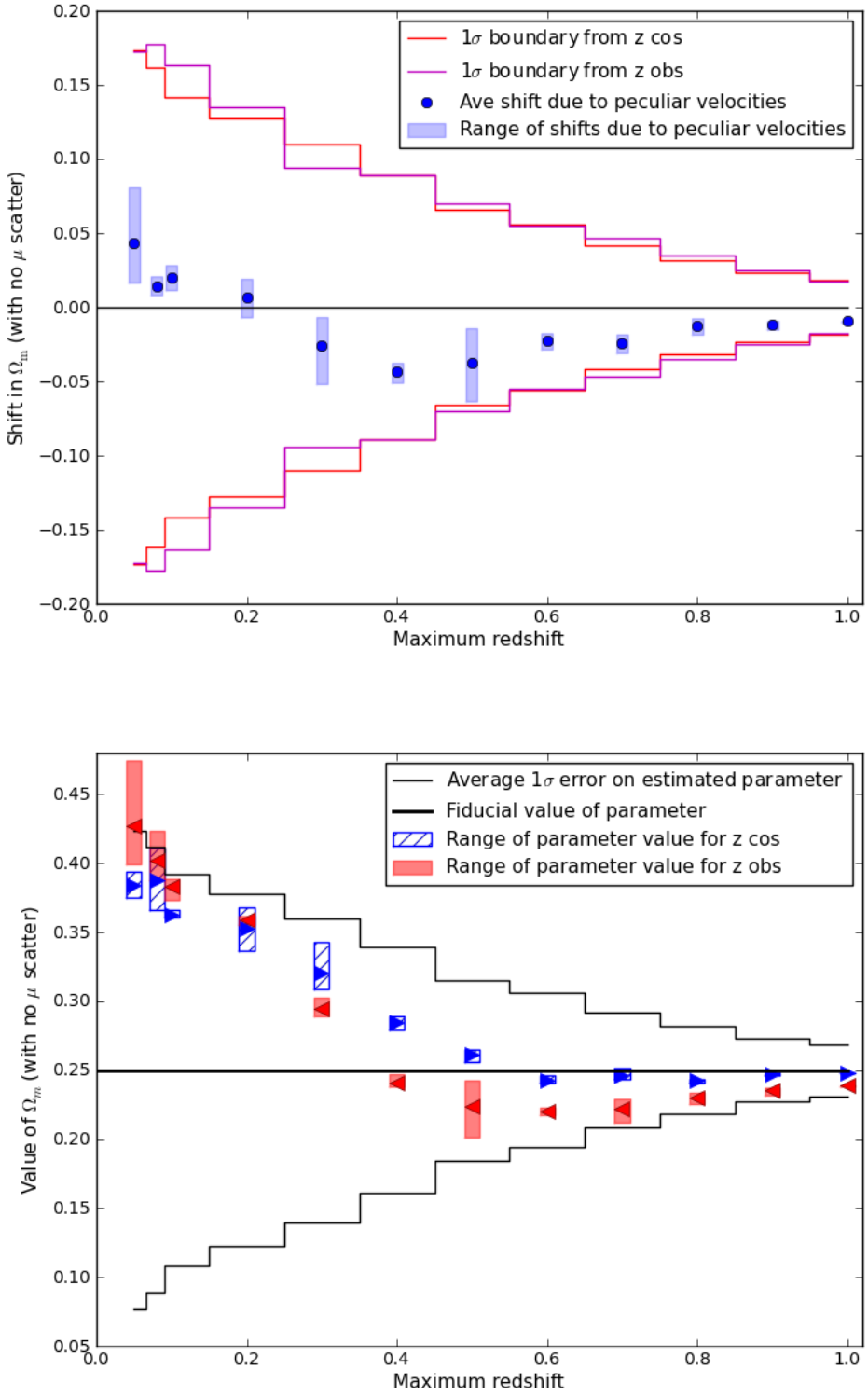

Figure 4.17: Shifts *(top)* and estimated values *(bottom)* for Ω_m for SNIa with exact distance modulus data and various maximum redshift cuts. The shifts are almost unchanged compared with the case where there is scatter on the distance modulus. The estimated values using cosmological redshifts are close to exact for maximum redshifts above $z = 0.5$ Using only low redshift SNIa, Ω_m is $\sim 1\sigma$ from the fiducial value even when using perfect redshift data.

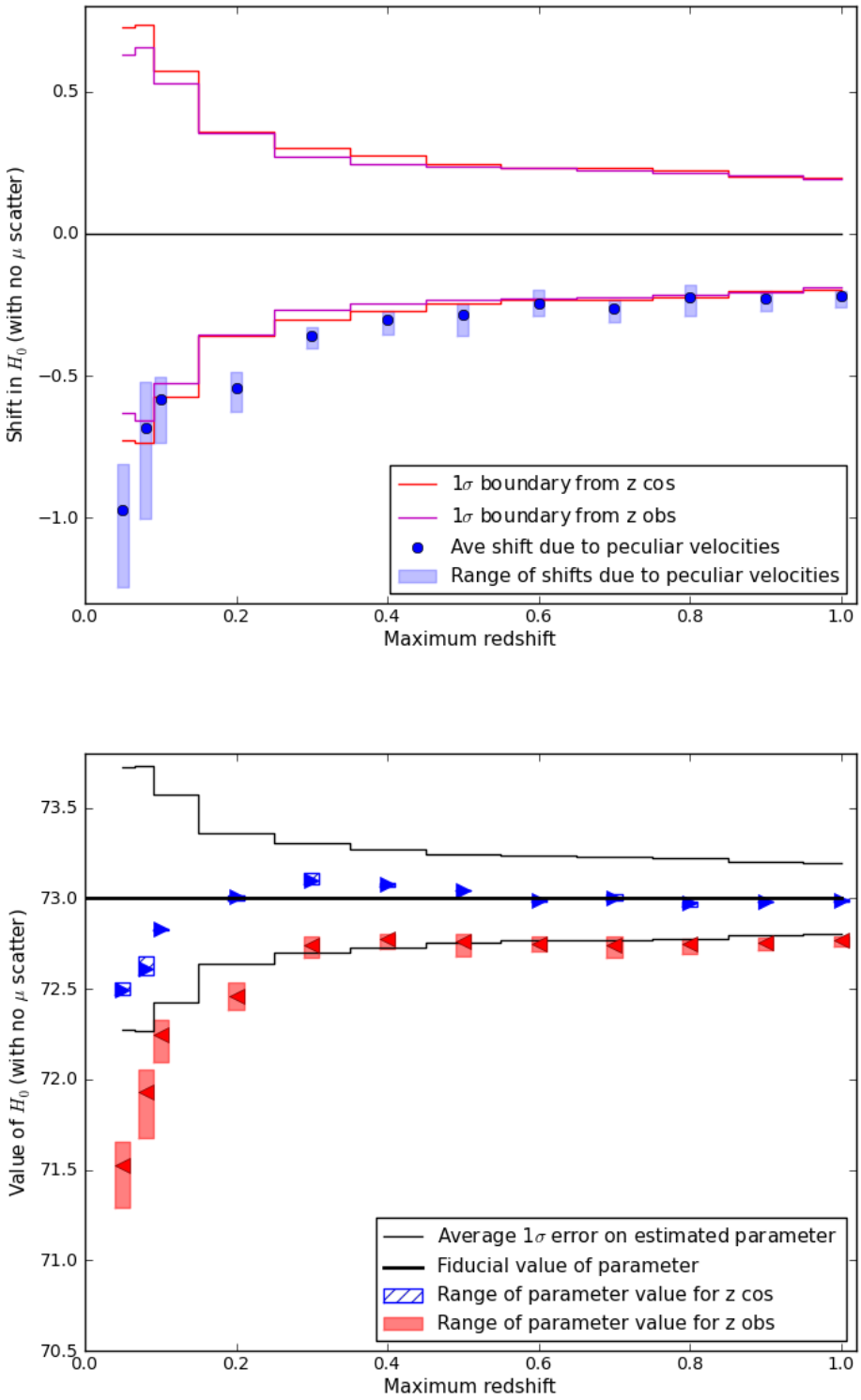

Figure 4.18: Shifts *(top)* and estimated values *(bottom)* for H_0 for SNIa with exact distance modulus data and various maximum redshift cuts. As for Ω_m the shifts in H_0 are unchanged. The estimated values are improved by about 1σ in all cases, making the estimates using cosmological redshifts almost exact for redshifts above $z = 0.5$ and estimates using observed redshifts approximately 1σ from the fiducial values.

Chapter 5

Conclusion

In this work we investigated the impact of peculiar velocities on the estimation of cosmological parameters using SNIa. We first created simulated SNIa data which includes information about the peculiar velocities of the host galaxies. SNIa were painted onto mock galaxy surveys, created by Kitzbichler and White (2007), using the supernova rates from Mannucci et al. (2005) that are based on the colour and mass of galaxies. For the mock galaxy surveys, Kitzbichler and White (2007) defined an observer and created a catalogue of the galaxies on that observer's backwards light cone for a field of view of 2 square degrees. The galaxies themselves were simulated by De Lucia and Blaizot (2007) using a semi-analytic model for galaxy formation applied to the output of the Millennium (N-body) Dark Matter Simulation.

Running CosmoMC for approximately 24 weeks (4000 hours) of CPU time, we estimated the cosmological parameters using our simulated SNIa, first fitting the data using the true cosmological redshifts and then with the observed redshifts. The redshifts differ because of the radial components of the host galaxy peculiar velocities which contaminate the observed redshifts. The comparison of the parameter estimates from the two different redshifts provides a measure of the impact of peculiar velocities.

Where the peculiar velocities are random and uncorrelated they have little effect on the parameters, and an uncertainty was added to the distance modulus error bars to account for these. However, where peculiar velocities are correlated, they may introduce a bias to the Hubble diagram and consequently bias the estimated parameters. It is the effects of the correlated peculiar velocities that we investigated. Since the peculiar velocities are due to gravitational interactions of SNIa host galaxies with their local environments, SNIa that are close together are more likely to be correlated. As a result, observations of SNIa at low redshift, which probe a smaller volume, are likely to be more correlated than observations at higher redshifts.

This chapter summarises the key findings of this work and possible extensions to it that could be explored in future.

5.1 Simulating SNIa Data

We successfully generated SNIa data for a simulated deep survey (similar to the SNLegacy Survey) with six different pointings of a 2 square degree field out to redshift $z = 1$. We also created a simulated wide survey (like SNFactory) which approximates a shallow survey up to $z = 0.1$ and spans 1200 square degrees in the sky. Because of the small field of view of the mock galaxy surveys, peculiar velocities of the SNIa in the wide survey are overcorrelated and therefore the results provide upper bounds on the effect of peculiar velocity correlations. However, plotting the simulated SNIa on the Hubble diagram shows them to be a good approximation of observed SNIa, in terms of redshift distribution and scatter, by the similarity of the Hubble diagrams. We considered the most optimistic case in terms of the error on μ, by assuming perfect photometric data, which also corresponds to an upper bound of the effects of the peculiar velocities. These simulated data can be used in investigating how actual SNIa observations would be impacted by effects such as peculiar velocities.

5.2 Reducing Correlations

We showed (in Section 4.2) that combining observations from different parts of the sky significantly reduces the correlations in the peculiar velocities of galaxies and therefore, of SNIa. This is expected since the peculiar velocities are related to local environments and therefore SNIa with large angular separations are unlikely to be correlated.

In future SNIa surveys this should be an important consideration when designing observing strategies as multiple observations from spatially separate regions will reduce the correlations in peculiar velocities and therefore their effect on cosmological parameter estimation.

5.3 The Impact of Peculiar Velocities

Even as an upper bound, due to overcorrelation in the low redshift SNIa data, the shifts in parameter estimates that are caused by peculiar velocities are not generally statistically significant. For Ω_m the values calculated using observed redshifts are less than 1σ from those obtained using cosmological redshifts, and for H_0 the shifts are approximately equal to the 1σ errors.

Despite the shifts being small, the results do show a systematic and marginally measurable effect caused by the peculiar velocities and they suggest interesting relationships between the SNIa data and the estimated parameters.

- Removing the low redshift SNIa, which are likely to be the most correlated, from the data is effective in reducing the shifts in parameters, however, if the cutoff redshift is too high then the accuracy of the estimated values may be compromised. From these data the optimal minimum redshift cut appears to be at $z = 0.05$.

- Even in the case of perfect distance modulus measurements, when using observed redshifts, the parameter estimates can be out by more than 1σ when only SNIa at low redshifts are used.

- In the case of H_0, where there is scatter on the distance modulus data, the estimates consistently underestimate the fiducial value, by $\sim 2\sigma$ in the case of observed redshifts and $\sim 1\sigma$ in the case of cosmological redshifts.

In general the shifts in parameter estimates due to correlations in the peculiar velocities are typically around 1σ or less, with H_0 slightly more biased than Ω_m. In specific cases, where only low redshift (below $z = 0.08$) data is used the shift can be up to 3σ. Since H_0 is determined by low redshift data, it is not surprising that it is more affected by the correlations which occur primarily at low redshift. Actual SNIa surveys, both existing and planned, will have SNIa data to redshifts of least $z = 0.1$ and in almost all cases to much higher redshifts, therefore the extreme case of parameter estimation with only very low redshifts is not very relevant to reality.

Combining the 1σ shift with standard sample variance, means that, in general, peculiar velocity correlations can cause a shift in the recovered cosmological parameters of up to 2σ. This suggests that future surveys will have to deal with the correlations in SNIa peculiar velocities in order to ensure unbiased parameter estimates.

5.4 Future Work

In future, there are a number of things that could be done to extend this work. Perhaps the most important one would be to create simulated data for a wide shallow SNIa survey with the appropriate correlations in the peculiar velocities. This would give a more accurate idea of the peculiar velocity effect and not just an upper bound as in this case. For this it would be necessary to construct a wide mock galaxy survey looking back along an observer's past light cone for a large area in the sky. The supernova could then be painted onto this new mock galaxy survey according to SNIa rates. The field of view achievable without causing overcorrelation of peculiar velocities may be limited by the size of the simulation box.

In addition to simulating a more accurate low redshift survey, another possible extension would be to simulate a SNIa survey to intermediate redshifts like SDSS.

It would also be interesting to generate SNIa data using different SNIa rates for comparison. The various simulated datasets could also be compared to observational data, particularly from future surveys which will be comparable in number, to evaluate the accuracy of the rates and help to refine them.

The CosmoMC parameter estimation could be done with additional parameters varied, such as Ω_k and perhaps also including the other cosmological datasets available in CosmoMC (e.g. CMB data, baryon acoustic oscillations, data from clusters, HST etc).

There will be substantially more observational SNIa data available from future SNIa surveys such as the Dark Energy Survey (DES), Pan Starrs and LSST. This work suggests that

in future the effects of correlated peculiar velocities will need to be considered, particularly as we collect more and more SNIa data and refine our understanding of these standardisable candles.

With knowledge of the galaxy distribution, we could map the density field of the dark matter and use it to estimate the peculiar velocities of the galaxies (Eisenstein et al. 2007). Then, using these, the SNIa redshifts could be corrected prior to running the parameter estimation to improve the accuracy. Using simulated SNIa we could test the level of accuracy possible in recovering the peculiar velocities and evaluate the effect of correcting the SNIa on the accuracy of the estimated parameters.

Appendix A

Derivation: An Expression for the Peculiar Velocity Field

To compute the density perturbation δ defined in section 1.3 and the peculiar velocity field $\mathbf{v}$ we use linear perturbation theory.

Using comoving coordinates and assuming negligible pressure so that $\dot{\rho}_0 = -3\rho_0\dot{a}/a$, the mass conservation equation can be written as (Peebles 1993):

$$\frac{\partial\delta}{\partial t} + \frac{1}{a} \bigtriangledown \cdot[(1+\delta)\mathbf{v}] = 0 \tag{A.1}$$

We can remove the unperturbed part of Poisson's equation to get:

$$\bigtriangledown^2\phi = 4\pi G\rho_0 a^2\delta \tag{A.2}$$

and using this and the Euler equation of motion, and removing the background where $\mathbf{v} = 0 = \phi$ we get:

$$\frac{\partial\mathbf{v}}{\partial t} + \frac{\dot{a}}{a}\mathbf{v} + \frac{1}{a}(\mathbf{v}\cdot\bigtriangledown)\mathbf{v} = -\frac{1}{a}\bigtriangledown\phi \tag{A.3}$$

Then we use linear perturbation theory. Perturbations are assumed to be small in comparison to the background and therefore terms of second order and higher are negligible and can be ignored. Under these assumptions equations A.1 and A.3 become:

$$\frac{\partial\delta}{\partial t} + \frac{1}{a} \bigtriangledown \cdot\mathbf{v} = 0 \tag{A.4}$$

$$\frac{\partial\mathbf{v}}{\partial t} + \frac{\dot{a}}{a}\mathbf{v} + \frac{1}{a}\bigtriangledown\phi = 0 \tag{A.5}$$

Taking the time derivative of equation A.4, subtracting it from the divergence of equation A.5 and substituting Poisson's equation (equation A.2) we get:

$$\frac{\partial^2\delta}{\partial t^2} + \frac{2\dot{a}}{a}\frac{\partial\delta}{\partial t} = 4\pi G\rho_0\delta \tag{A.6}$$

which describes the time evolution of the density perturbation δ in the mass distribution. The solution to this equation is of the form:

$$\delta = A(\mathbf{x})D_1(t) + B(\mathbf{x})D_2(t) \tag{A.7}$$

where $\mathbf{x}$ is comoving position.

Assuming that one of the solutions representing the growing mode dominates the expression becomes (Peebles 1993):

$$\delta = A(\mathbf{x})D(t) \tag{A.8}$$

and then equation A.4 can be written as:

$$\bigtriangledown \cdot \mathbf{v} = -a\frac{\partial \delta}{\partial t} = a\delta\frac{\dot{D}}{D} \tag{A.9}$$

Solving this we get:

$$\mathbf{v}(\mathbf{x}) = a\frac{fH}{4\pi}\int \frac{\mathbf{y}-\mathbf{x}}{|\mathbf{y}-\mathbf{x}|^3}\delta(\mathbf{y})d^3y \tag{A.10}$$

where f is the dimensionless velocity factor:

$$f = \frac{a}{\dot{a}}\frac{\dot{D}}{D} = \frac{1}{H}\frac{\dot{D}}{D} \tag{A.11}$$

This velocity equation is in comoving coordinates, as indicated by the presence of a on the right hand side. This means that Hubble expansion is accounted for and the velocity $\mathbf{v}$ refers to the peculiar velocity only

Taking it a step further we can use Poisson's equation and using $\mathbf{g} = -\bigtriangledown\phi/a$ we can write the peculiar velocity as:

$$\mathbf{v} = \frac{fH}{4\pi G\rho_0}\mathbf{g} = \frac{2}{3}\frac{f}{\Omega H}\mathbf{g} \tag{A.12}$$

where $\mathbf{g}$ is the peculiar gravitational acceleration (Peebles 1993).

Note on the growing mode

The growing mode D_1 or D is given by (Strauss and Willick 1995) as:

$$D_1(t) = \frac{\dot{a}}{a}\int \dot{a}^{-3}\mathrm{da} \tag{A.13}$$

The solutions for the growing mode D_1 depend on the total density parameter. A large value of Ω gives rise to faster growth and where $\Omega < 1$ expansion dominates over gravitational attraction and clustering freezes out. For the special case of a flat, matter dominated universe where $\Omega = 1$ and $a(t) \propto t^{2/3}$ we get:

$$D_1(t) = t^{2/3} \tag{A.14}$$

Appendix B

Comparison of Observed and Simulated Hubble diagrams

Figures B.1 and B.2 show respectively a Hubble diagram from Kessler et al. (2009) and a Hubble diagram constructed using simulated SNIa over the same scale for comparison purposes. These two Hubble diagrams display comparable scatter and a similar shape which confirms that the simulated SNIa are realistic and that the cosmology underlying the Millennium Simulation is close to what we observe.

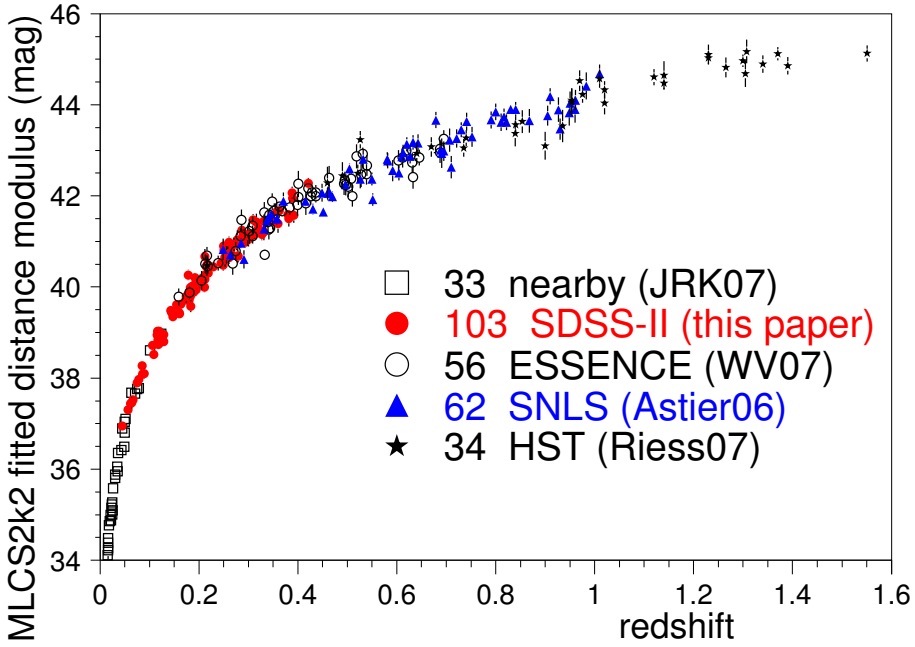

Figure B.1: Hubble diagram by Kessler et al. (2009) showing 288 SNIa from the samples listed on the plot. This plot is a reproduction of Figure 1.6

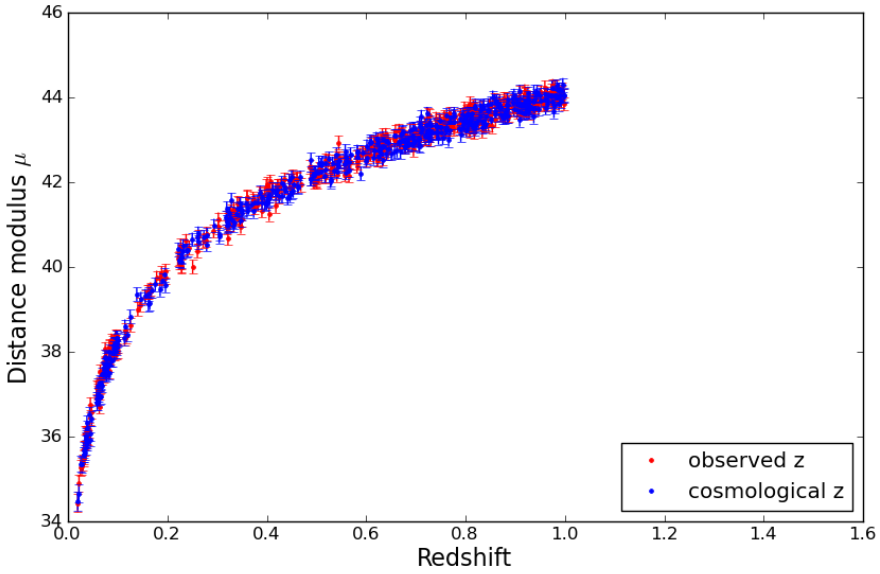

Figure B.2: Hubble diagram constructed using a random sample of simulated SNIa plotted over the same redshift and distance modulus ranges as Figure B.1 to facilitate comparison of the plots.

Appendix C

Additional Figures for Parameter Estimation with Normalised Observed Redshifts

The figures in this Appendix correspond to parameter estimation using normalised observed redshifts, as explained in Section 4.3.4.

In addition to the shifts in Ω_m and H_0 that can be seen in Figure 4.16, we compared the estimated values of the parameters for these CosmoMC runs with the fiducial values. Figure C.1 shows the ranges of estimated values for the Ω_m and H_0 calculated using normalised observed redshifts and various maximum redshift cuts.

We also performed the parameter estimation for SNIa datasets with various minimum redshifts and using the normalised observed redshift data. Figures C.2 and C.3 show the calculated shifts in Ω_m and H_0 respectively (top panels) and the estimated values for these parameters (bottom panels).

As discussed in Section 4.3.4, the normalised redshifts do not result in a significant improvement in the parameter estimates or in the shifts which indicates that the observed redshifts do not contain a global bias.

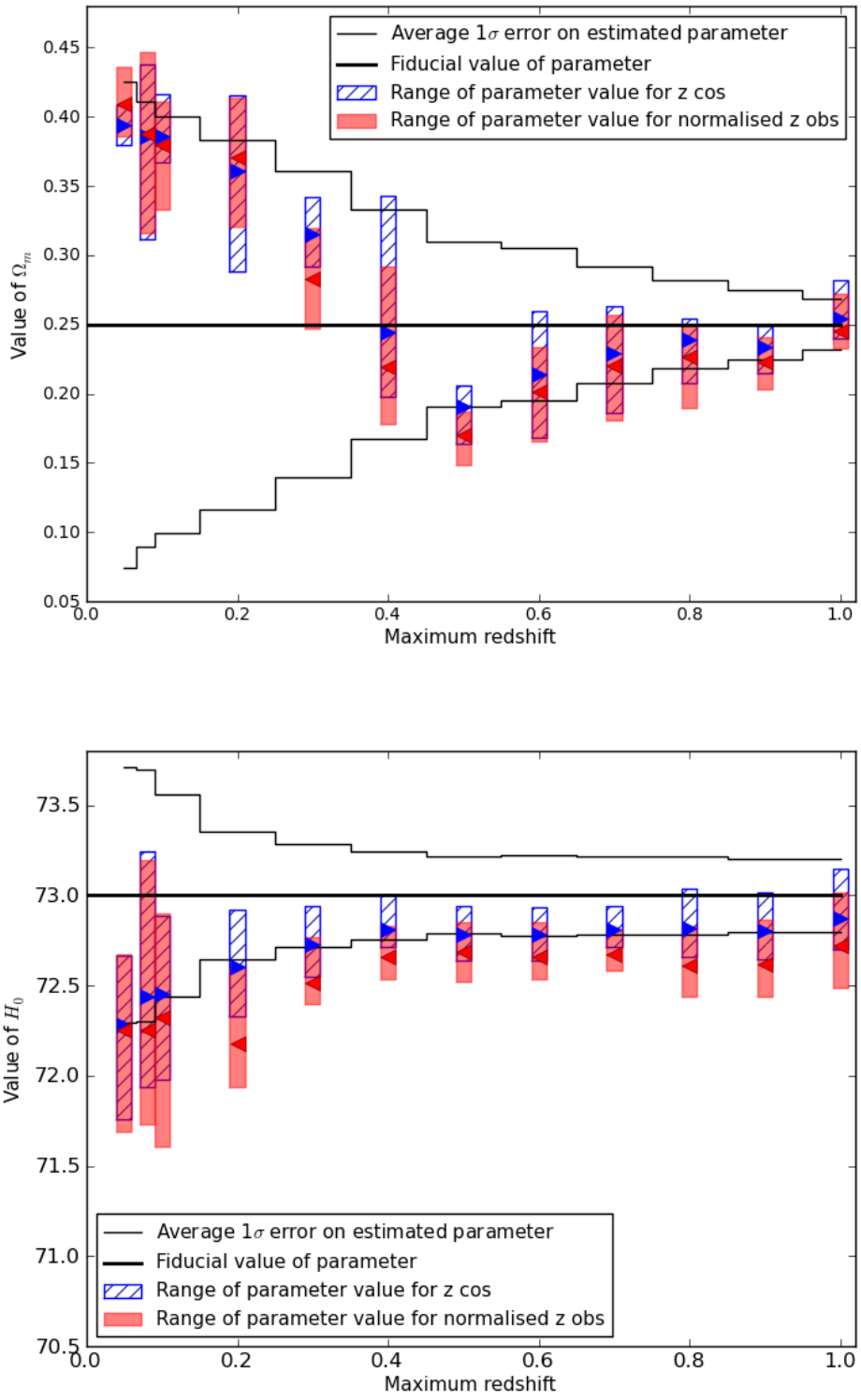

Figure C.1: Range of Ω_m *(top)* and H_0 *(bottom)* estimates calculated using observed redshifts (red, shaded bars) and cosmological redshifts (blue, hatched bars) for various maximum redshift cuts in the SNIa data using normalised observed redshifts.

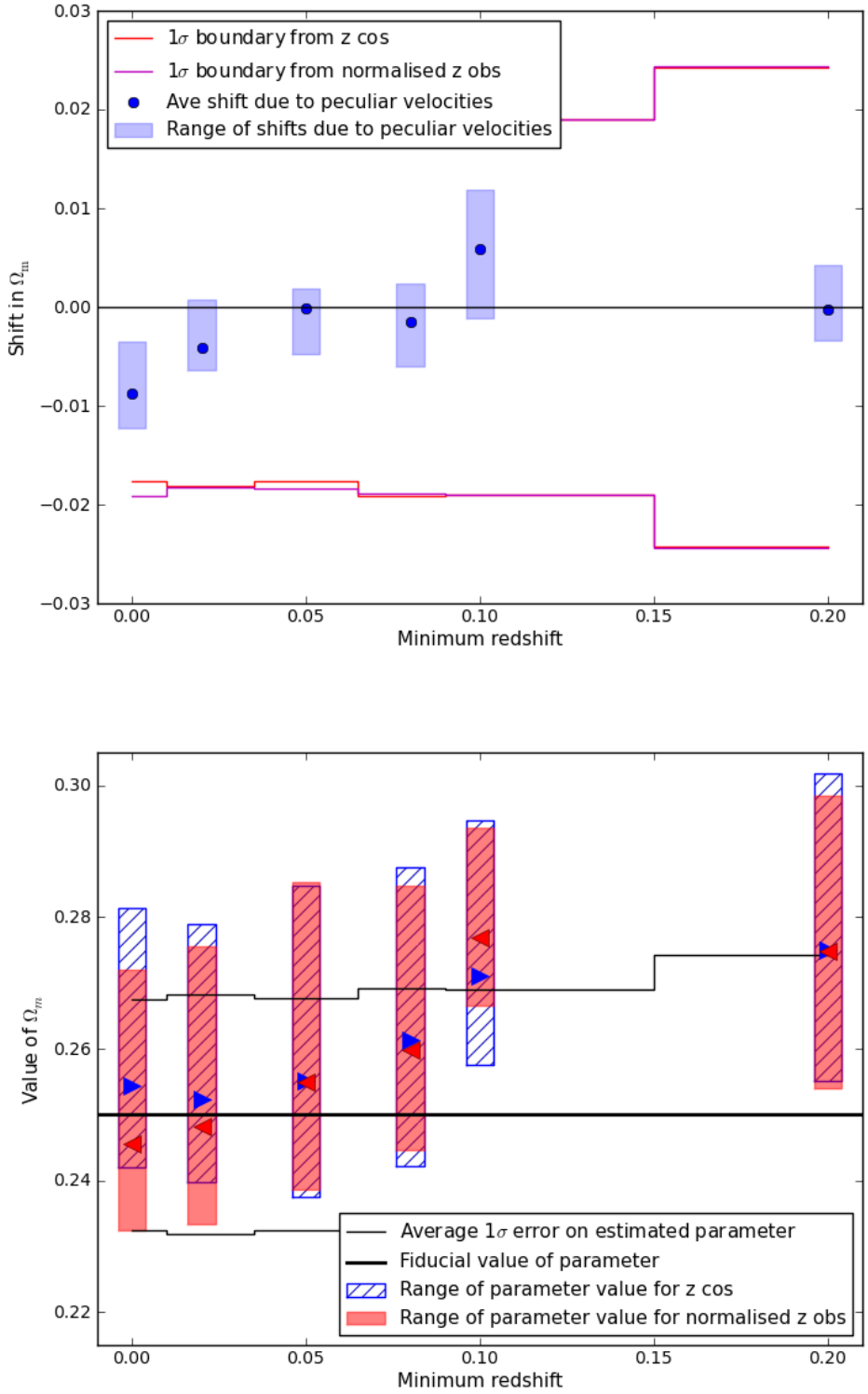

Figure C.2: Shifts *(top)* and estimated values *(bottom)* for Ω_m using normalised observed redshifts for various minimum redshift cuts. The results do not show a marked improvement on those calculated with the unaltered observed redshifts, suggesting that there is no bias in the data.

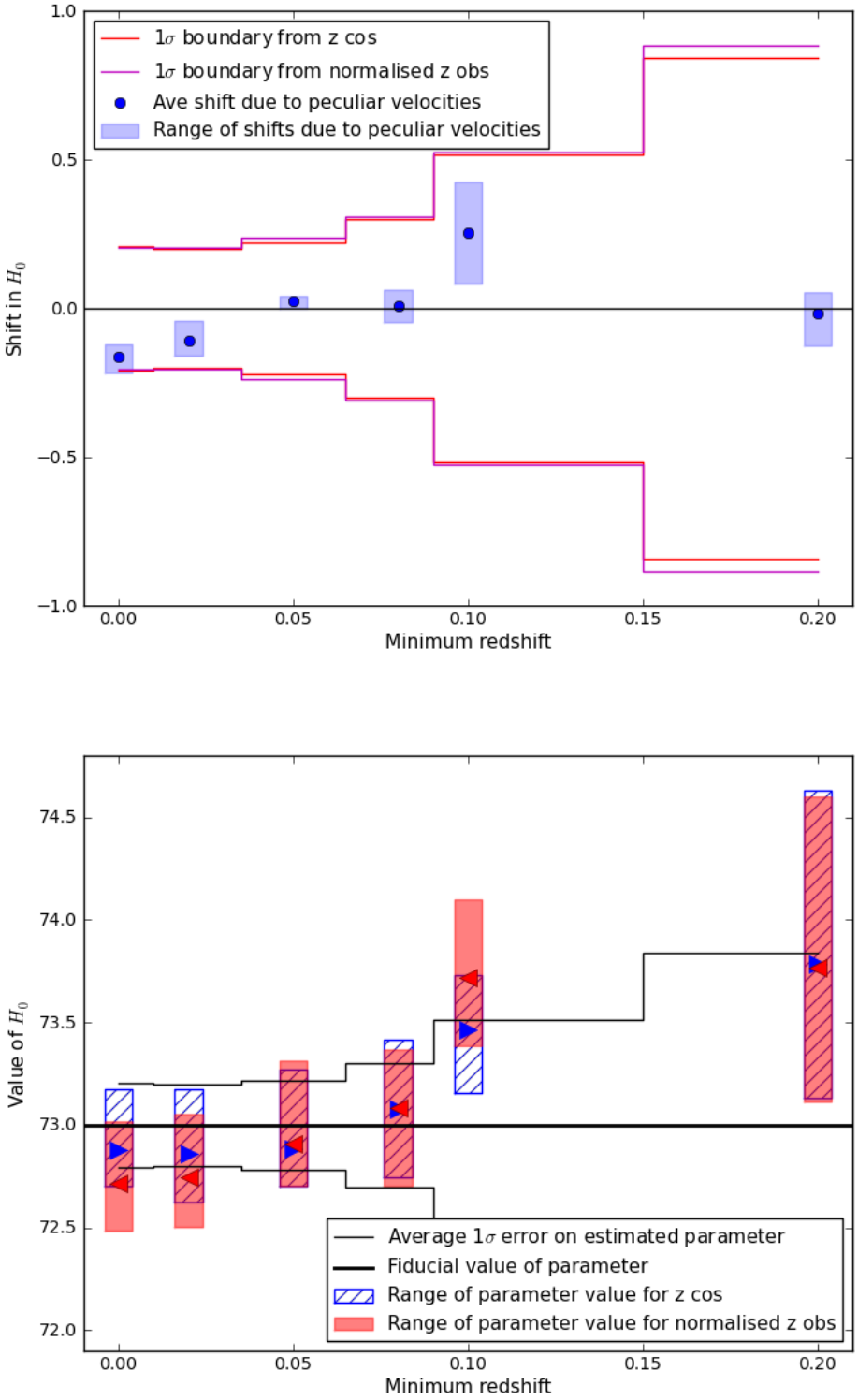

Figure C.3: Shifts *(top)* and estimated values *(bottom)* for H_0 using normalised observed redshifts for various minimum redshift cuts.

Appendix D

Additional Figures for Parameter Estimation with Exact Distance Modulus Data

In Section 4.3.5, the results of the parameter estimation using exact distance modulus data are shown for SNIa datasets with varying maximum redshift cuts imposed. Here, in this Appendix, we provide the results for SNIa datasets with various minimum redshifts and using the exact distance modulus data.

Figure D.1 shows the results of the calculated shifts and estimated values for Ω_m, and those for H_0 are shown in Figure D.2. In both cases, the results are computed using exact distance modulus data with no scatter applied.

As seen and discussed in Section 4.3.5, removing the scatter on the distance modulus data has no effect on the size of the shifts in Ω_m and H_0 that are due to the correlated peculiar velocities. It does, however, result in estimated parameter values, particularly when using cosmological redshifts, that are closer to the fiducial values.

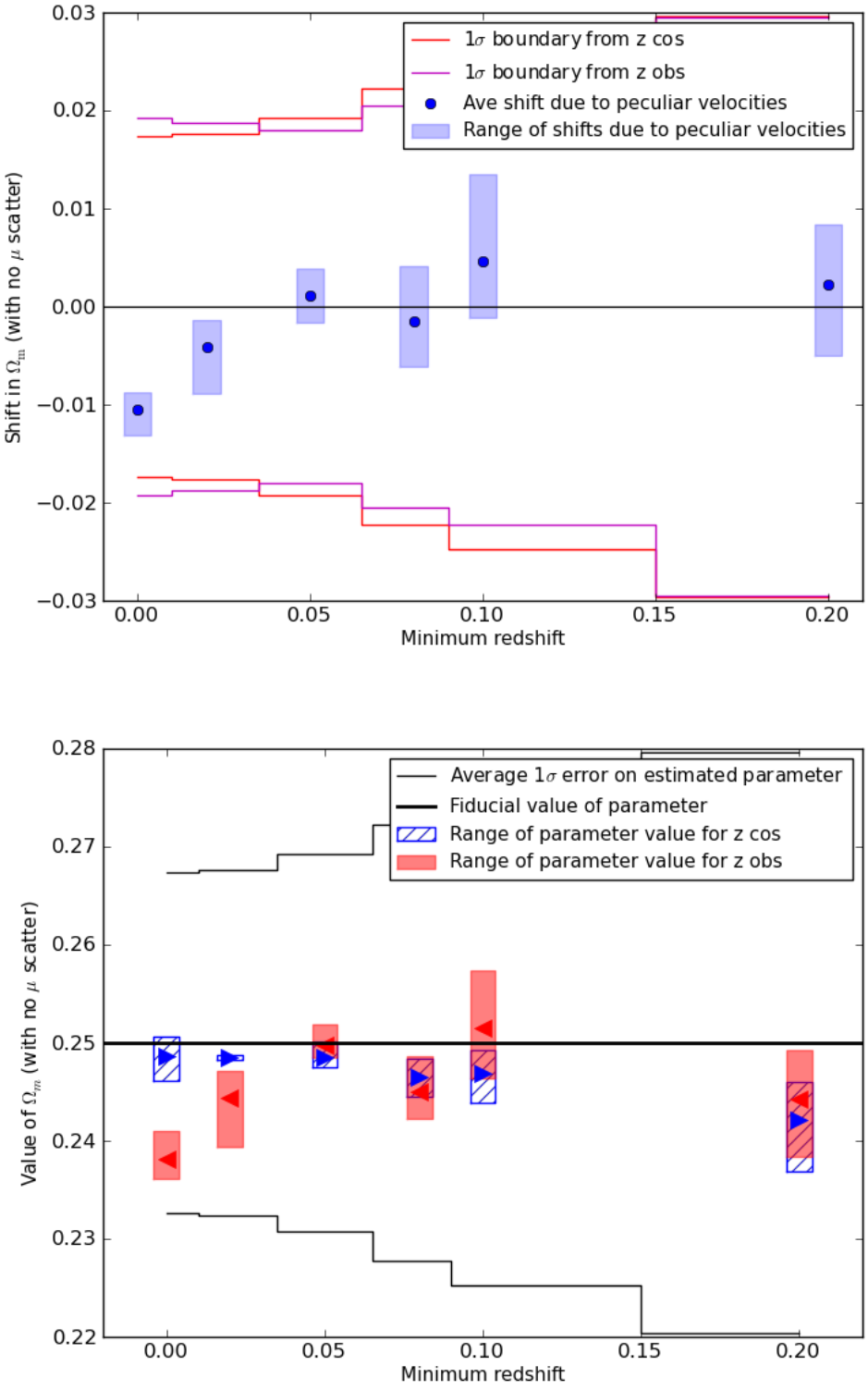

Figure D.1: Shifts *(top)* and estimated values *(bottom)* for Ω_m for SNIa datasets with accurate distance modulus data and various minimum redshift cuts imposed. The shifts are not affected by the removal of the scatter on the distance modulus, however, the estimated values appear to be closer to the fiducial value.

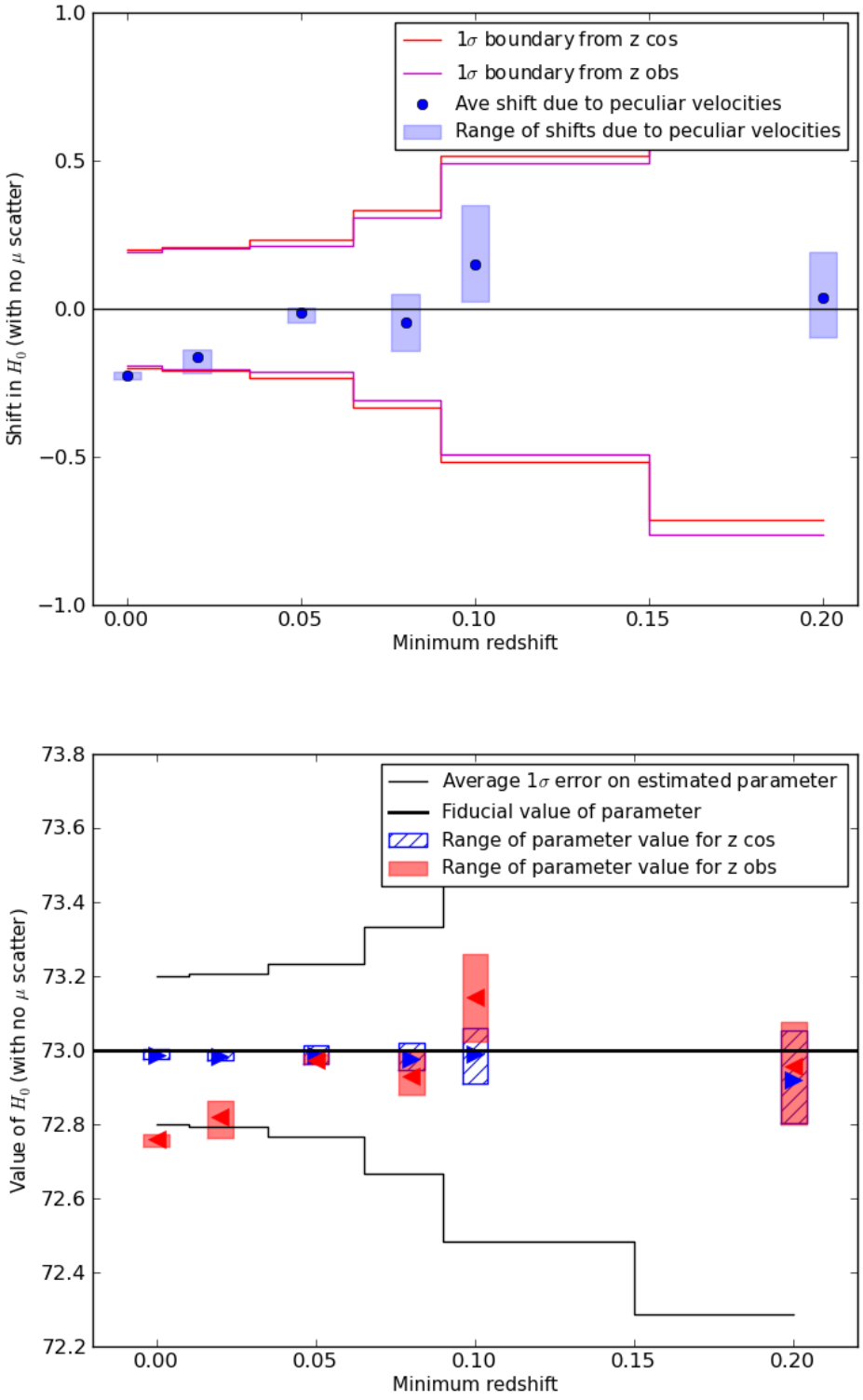

Figure D.2: Shifts *(top)* and estimated values *(bottom)* for H_0 for SNIa datasets with accurate distance modulus data and various minimum redshift cuts imposed. The shifts due to correlated peculiar velocities are unaffected by the lack of scatter on the distance modulus data.

Appendix E

Parameter Estimation Using SNIa Samples of Various Sizes

To investigate the impact of the number of supernovae on the peculiar velocity effect, we generate SNIa datasets containing 200, 600, 1000, 2000 and 4000 SNIa. They are randomly drawn from the full SNIa catalogues which are also used and represent the upper bound on the size of SNIa samples that we can study. The number of SNIa in the three realisations varies slightly (see Section 4.1) but is approximated to 8800 in all cases for plotting purposes.

This appendix contains the results for the calculated shifts in Ω_m and H_0 as well as the estimated values of these parameters. We also computed the shifts and estimated values for these datasets with normalised observed redshifts, as in Section 4.3.4, and with exact distance modulus data as in Section 4.3.5.

These SNIa datasets are constructed by randomly selecting the given number of SNIa from the full catalogue of SNIa in each realisation. As a result of the shape of the mock galaxy surveys, there are many more objects at high redshift than at low redshift since the volume probed at high redshift is much greater. The smaller random samples are, therefore, likely to contain predominantly high redshift supernova where the peculiar velocity correlations are substantially reduced. This means that the peculiar velocity effect is likely to be underestimated when using the small samples of SNIa.

Figures E.1 and E.2 show the shifts and estimated values for the parameters for SNIa datasets of various sizes. The shifts for the SNIa datasets containing 200, 600 and 1000 SNIa are small, which is probably due to the selection effect explained above. As expected, the estimates values of Ω_m and H_0 approach the fiducial value as more SNIa are added.

The shifts in the parameters do not approach zero for the larger datasets, and therefore, as discussed in Section 4.3.4 we investigated the possibility of a global bias in the observed redshift data. We normalised the observed redshifts according to the average change in redshift for each SNIa sample. The results of the parameter estimation using the normalised observed redshifts are shown in Figures E.3 and E.4. As in Section 4.3.4 the results suggest that the observed redshift data is not biased since there is very little change from Figures

E.1 and E.2.

Finally, as in Section 4.3.5, we estimated the parameters using the exact distance modulus data with no scatter applied for the SNIa datasets containing different numbers of SNIa. The results are presented in Figure E.5 and E.6. These results show the same relationship as discussed in Section 4.3.5 where the shifts in parameters are unaffected by removing the scatter but the estimated values, particularly those calculated using the cosmological redshifts, are closer to the fiducial values.

All of the results we obtain by estimating the parameters for SNIa samples of different sizes support the conclusions laid out in Chapter 5.

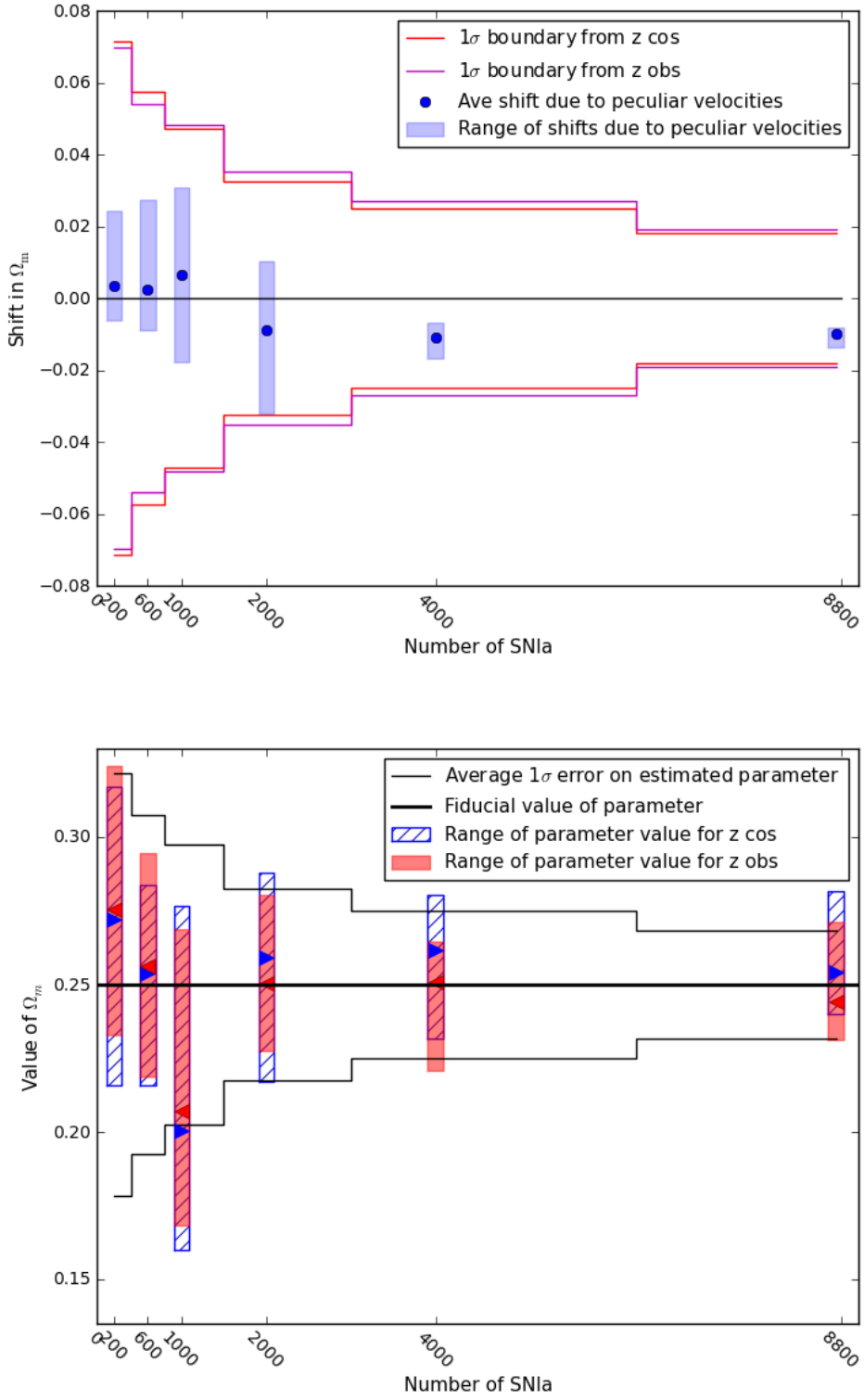

Figure E.1: Shifts *(top)* due to correlated peculiar velocities and estimated values *(bottom)* for Ω_m for different numbers of randomly selected SNIa.

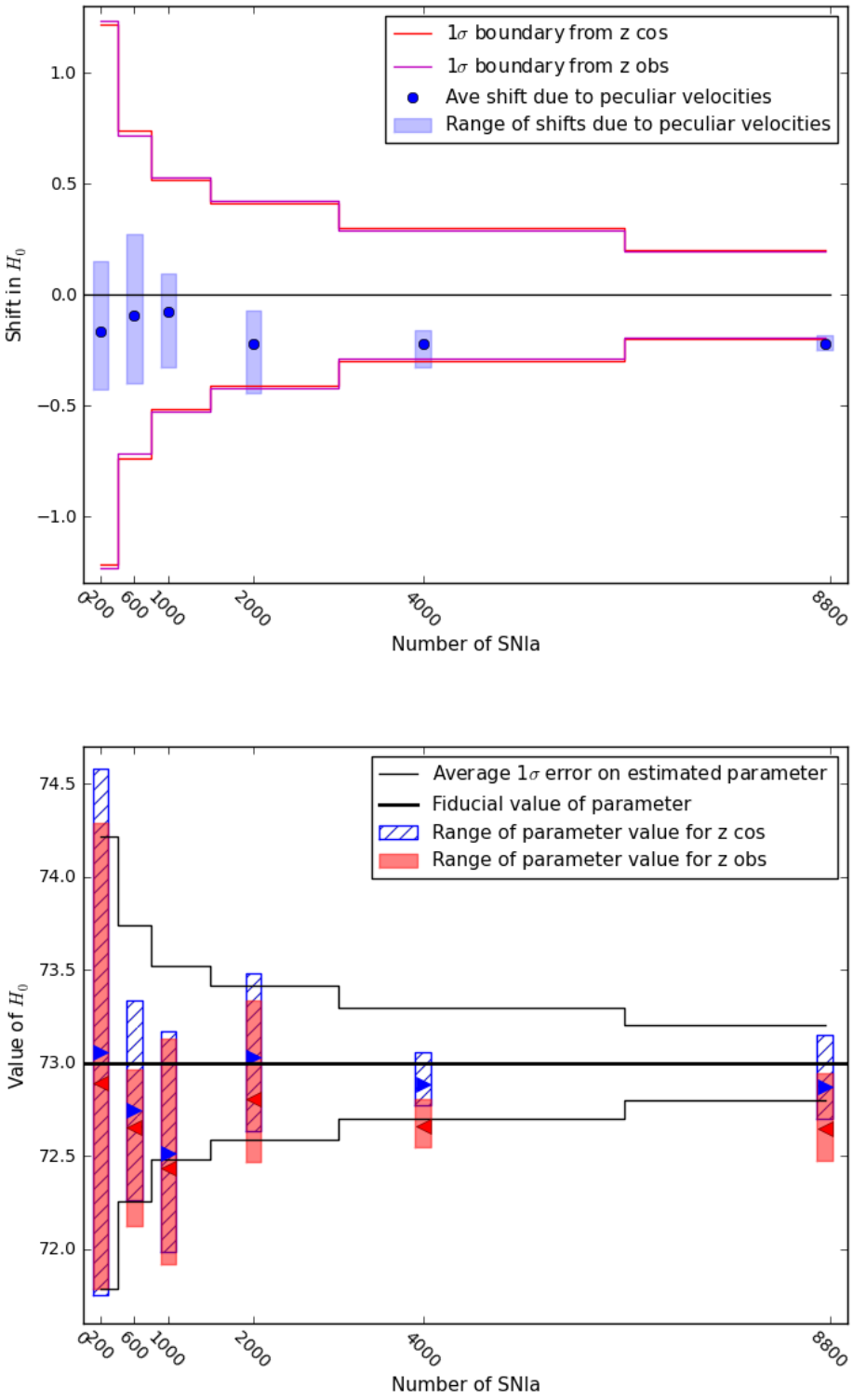

Figure E.2: Shifts *(top)* due to correlated peculiar velocities and estimated values *(bottom)* for H_0 for different numbers of randomly selected SNIa.

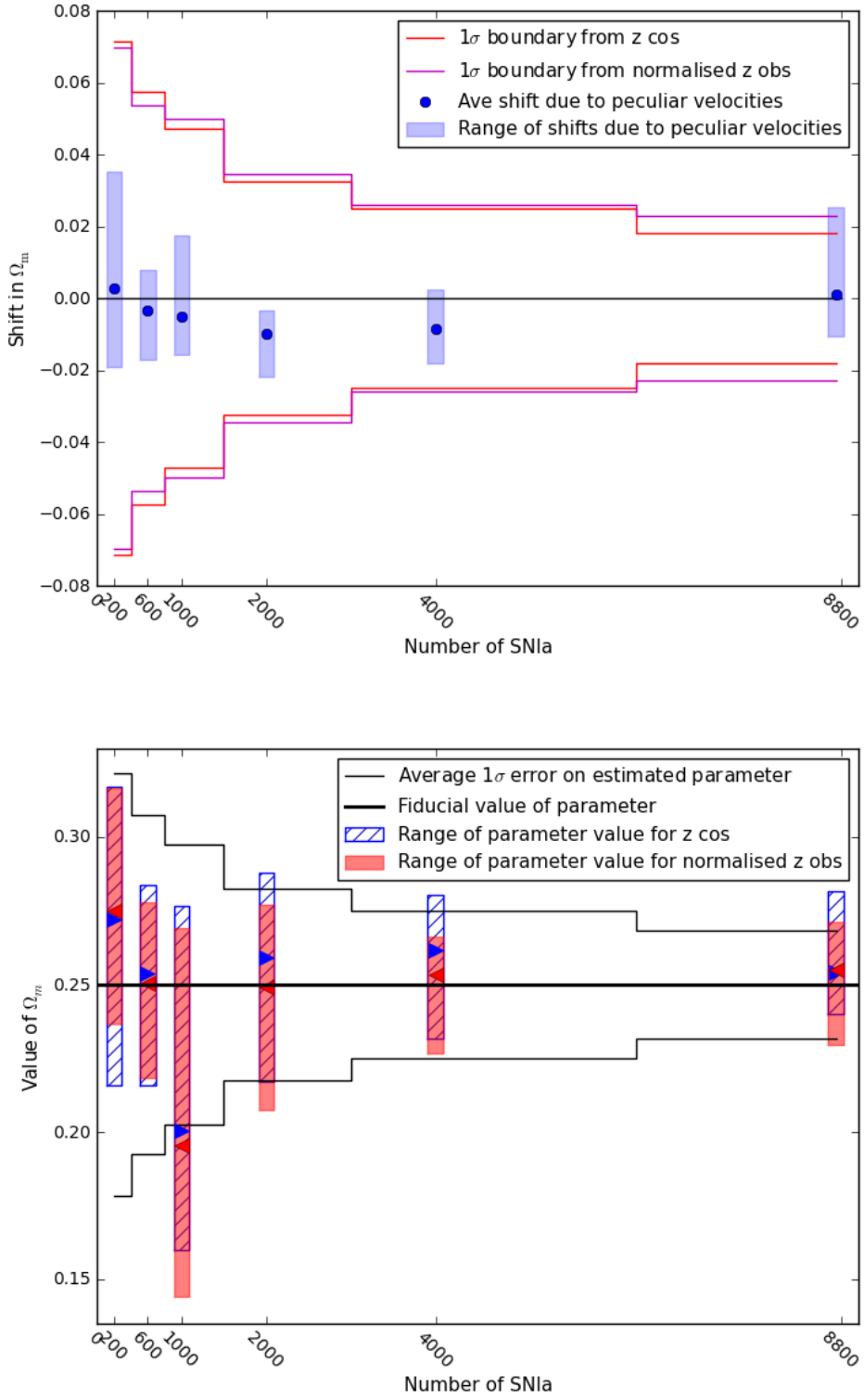

Figure E.3: Shifts *(top)* due to correlated peculiar velocities and estimated values *(bottom)* for Ω_m using normalised observed redshifts for different numbers of randomly selected SNIa.

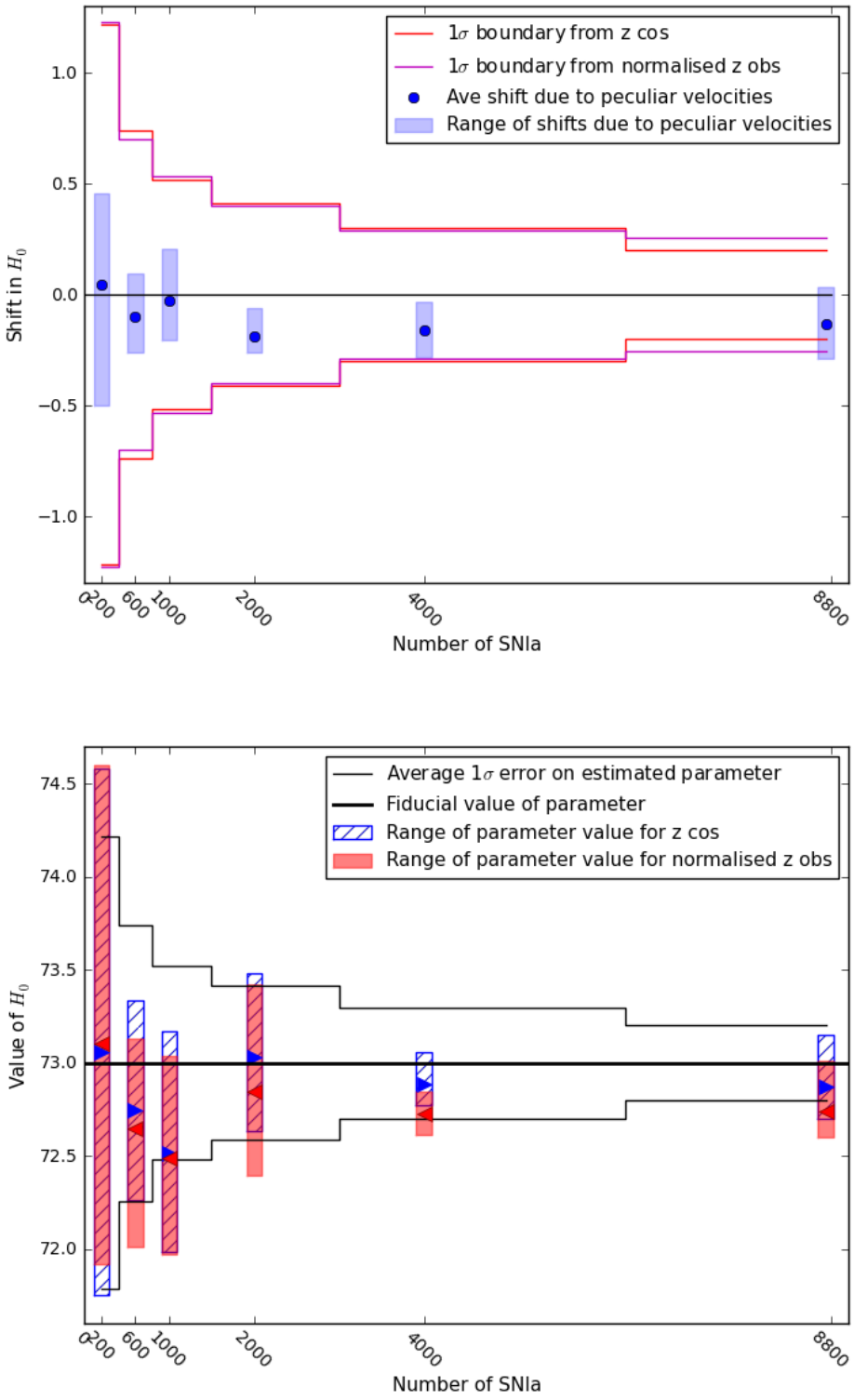

Figure E.4: Shifts *(top)* due to correlated peculiar velocities and estimated values *(bottom)* for H_0 using normalised observed redshifts for different numbers of randomly selected SNIa.

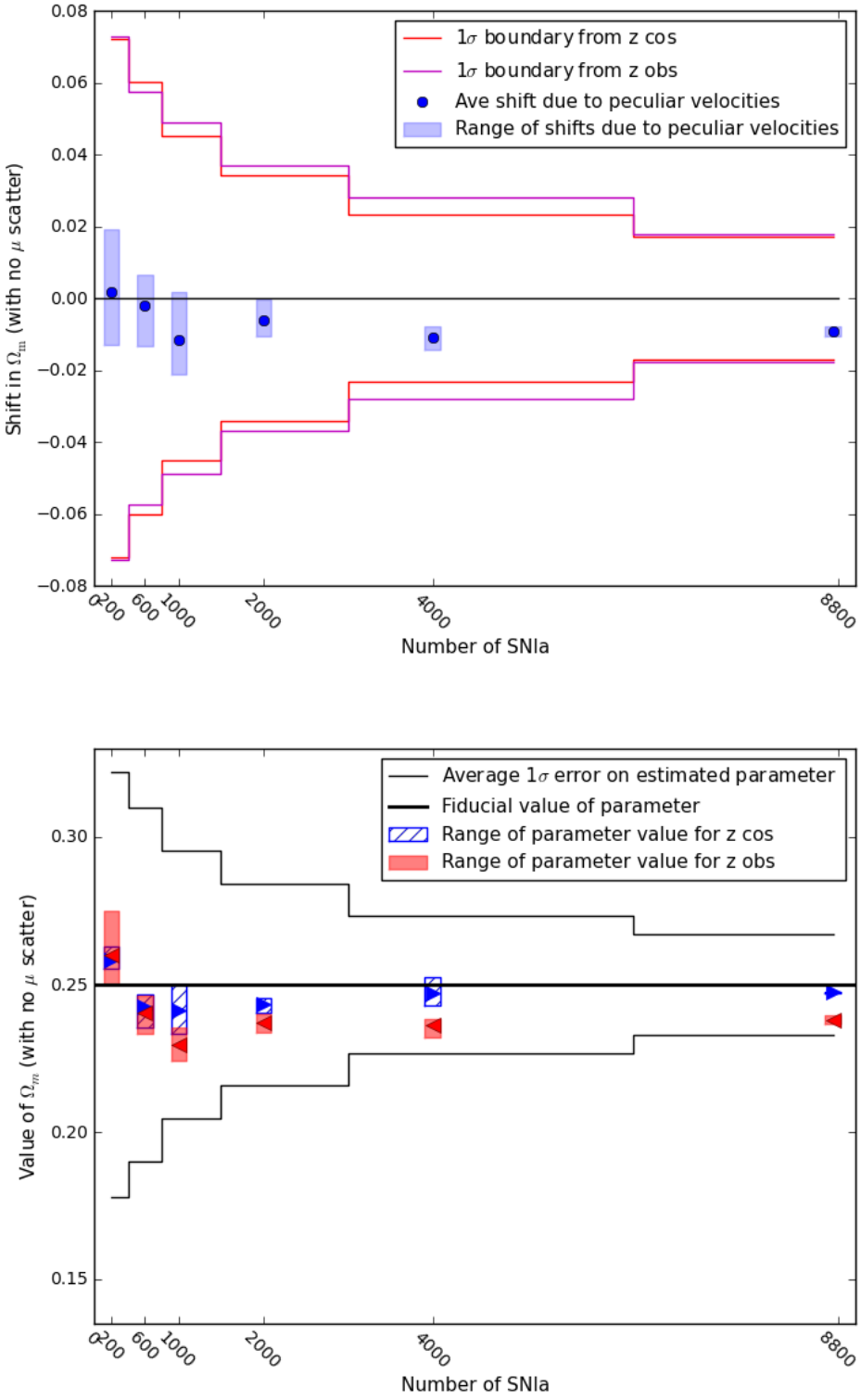

Figure E.5: Shifts *(top)* due to correlated peculiar velocities and estimated values *(bottom)* for Ω_m using exact distance modulus data for different numbers of randomly selected SNIa.

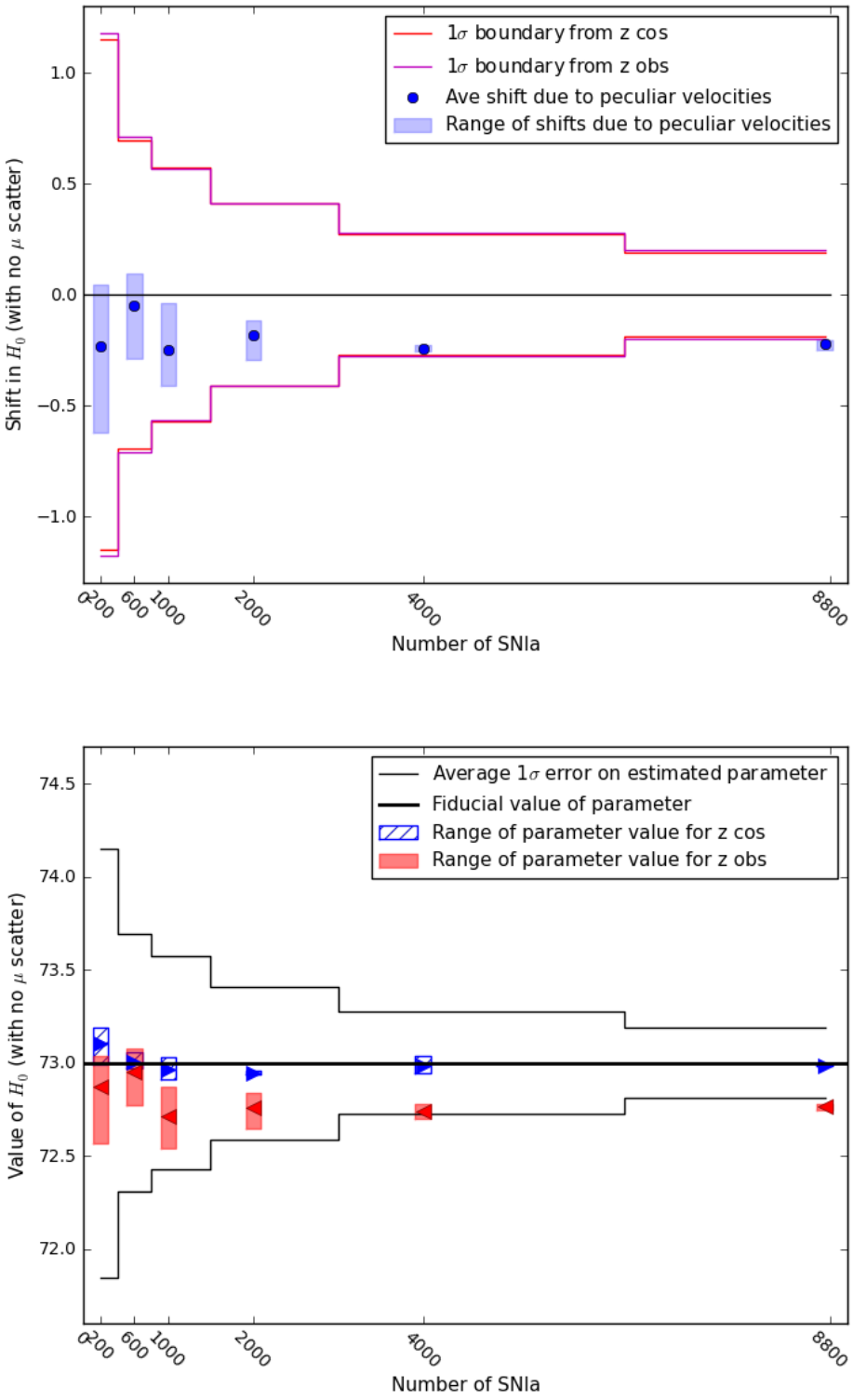

Figure E.6: Shifts *(top)* due to correlated peculiar velocities and estimated values *(bottom)* for H_0 using exact distance modulus data for different numbers of randomly selected SNIa.

Appendix F

Results Tables

This appendix contains the data presented in the figures in Section 4.3 and in Appendices C, D and E in table format. The data are based on the results for the parameter estimation using CosmoMC for various scenarios and SNIa datasets. We calculated the shifts in Ω_m and H_0 caused by peculiar velocities, and compare the estimated values of these parameters to the fiducial values of $\Omega_m = 0.25$ and $H_0 = 73$ that underly the Millennium Simulation.

The results are shown for parameter estimation using:

- simulated SNIa data with no alterations,
- simulated SNIa with normalised observed redshifts (see Section 4.3.4), and
- simulated SNIa with exact distance modulus data (see Section 4.3.5).

For each of these types of data, the parameter estimation results are shown for various maximum and minimum redshifts, which are discussed in the main results section (Section 4.3), and for SNIa samples of different sizes (see Appendix E). Where the exact distance modulus data is used, there are only three versions of each scenario as opposed to the six in the other cases. This is because in the other cases, the six version are created by adding two different random scatters to the distance modulus data for each SNIa realisation, which is not possible when no scatter is added. There are no shifts that are exactly equal to zero, however, due to rounding, shifts less that 0.0005 appear in the tables as 0.0.

The tables presented here are:

- Table F.1: Shifts in Ω_m
- Table F.2: Estimated values of Ω_m
- Table F.3: Shifts in H_0
- Table F.4: Estimated values of H_0

Table F.1: Shifts in Ω_m caused by correlated peculiar velocities calculated from simulated SNIa data with various maximum and minimum redshift cuts and for SNIa samples of different sizes. The shifts are calculated with the standard simulated data, with normalised observed redshifts and with exact distance modulus data.

Data	Cut	z or N	Shifts in Ω_m for each run						Ave
			1	2	3	4	5	6	
Standard SNIa data	Max redshift	0.05	-0.003	0.012	0.005	0.012	0.033	0.023	0.014
		0.08	0.008	0.011	0.026	0.029	-0.001	0.055	0.022
		0.1	-0.02	0.026	0.044	0.014	0.033	0.011	0.018
		0.2	0.024	-0.008	0.06	0.015	-0.005	0.016	0.017
		0.3	-0.014	-0.001	-0.016	-0.017	-0.021	-0.054	-0.02
		0.4	-0.025	-0.011	-0.028	0.023	-0.072	-0.062	-0.029
		0.5	-0.029	-0.007	-0.016	-0.045	-0.043	-0.003	-0.024
		0.6	-0.024	-0.009	-0.024	-0.006	0.004	-0.061	-0.02
		0.7	-0.017	-0.024	-0.013	-0.021	-0.014	-0.01	-0.017
		0.8	-0.008	-0.019	-0.017	-0.011	-0.009	-0.017	-0.014
		0.9	-0.009	-0.013	-0.017	-0.012	-0.016	-0.013	-0.013
		1.0	-0.009	-0.014	-0.008	-0.009	-0.01	-0.009	-0.01
	Min redshift	0.0	-0.004	-0.007	-0.018	-0.005	-0.008	-0.018	-0.01
		0.02	-0.006	-0.007	-0.01	-0.006	-0.007	-0.007	-0.007
		0.05	-0.0	-0.003	0.002	0.001	0.001	0.0	0.0
		0.08	-0.002	-0.005	-0.002	-0.001	-0.012	-0.005	-0.005
		0.1	0.006	0.007	0.012	-0.003	0.002	0.004	0.005
		0.2	0.003	-0.002	0.002	0.003	-0.002	-0.002	0.0
	Sample size	200	-0.006	-0.003	-0.004	0.001	0.007	0.024	0.003
		600	0.005	-0.008	-0.007	0.027	0.007	-0.009	0.002
		1000	-0.008	-0.018	0.008	0.031	0.001	0.026	0.007
		2000	-0.006	-0.008	-0.008	0.01	-0.032	-0.009	-0.009
		4000	-0.007	-0.011	-0.008	-0.014	-0.017	-0.008	-0.011
		8800	-0.009	-0.014	-0.008	-0.009	-0.01	-0.009	-0.01
Using normalised observed z	Max redshift	0.05	0.01	0.01	-0.006	0.051	-0.013	0.039	0.015
		0.08	-0.044	0.004	0.052	0.002	-0.019	0.019	0.002
		0.1	-0.042	-0.01	-0.006	-0.012	0.015	0.014	-0.007
		0.2	0.071	-0.002	0.032	-0.023	-0.011	-0.007	0.01
		0.3	-0.012	-0.02	-0.029	-0.026	-0.047	-0.061	-0.033
		0.4	-0.007	-0.02	-0.016	-0.019	-0.038	-0.051	-0.025
		0.5	-0.032	-0.015	-0.025	-0.007	-0.024	-0.022	-0.021
		0.6	0.001	-0.003	0.003	-0.008	-0.002	-0.068	-0.013
		0.7	-0.012	-0.006	-0.006	-0.014	-0.005	-0.013	-0.009
		0.8	-0.005	-0.018	-0.014	-0.009	-0.016	-0.017	-0.013

Using normalised observed z		0.9	-0.008	-0.012	-0.017	-0.007	-0.007	-0.015	-0.011
		1.0	-0.007	-0.01	-0.011	-0.007	-0.01	-0.007	-0.008
	Min redshift	0.0	-0.003	-0.006	-0.012	-0.009	-0.01	-0.012	-0.009
		0.02	-0.005	0.001	-0.006	-0.005	-0.003	-0.006	-0.004
		0.05	0.002	-0.005	-0.001	0.002	0.001	0.001	-0.0
		0.08	-0.001	-0.002	0.0	0.002	-0.003	-0.006	-0.001
		0.1	0.006	0.004	0.009	0.012	-0.001	0.006	0.006
		0.2	-0.001	-0.001	0.0	-0.001	-0.003	0.004	-0.0
	Sample size	200	0.0	0.008	0.0	-0.008	-0.019	0.035	0.003
		600	0.008	-0.009	-0.0	0.006	-0.007	-0.017	-0.003
		1000	-0.008	-0.01	-0.016	-0.009	0.017	-0.005	-0.005
		2000	-0.006	-0.008	-0.011	-0.01	-0.022	-0.004	-0.01
		4000	-0.008	-0.005	0.002	-0.018	-0.014	-0.007	-0.008
		8800	-0.01	0.025	0.02	-0.011	-0.011	-0.008	0.001
Using exact distance modulus data	Max redshift	0.05	0.08	0.017	0.033				0.043
		0.08	0.021	0.008	0.013				0.014
		0.1	0.021	0.028	0.012				0.02
		0.2	0.006	0.019	-0.007				0.006
		0.3	-0.006	-0.051	-0.02				-0.026
		0.4	-0.041	-0.038	-0.051				-0.043
		0.5	-0.035	-0.014	-0.064				-0.038
		0.6	-0.018	-0.022	-0.028				-0.023
		0.7	-0.019	-0.022	-0.031				-0.024
		0.8	-0.011	-0.007	-0.018				-0.012
		0.9	-0.011	-0.009	-0.015				-0.012
		1.0	-0.009	-0.009	-0.01				-0.009
	Min redshift	0.0	-0.01	-0.009	-0.013				-0.01
		0.02	-0.001	-0.002	-0.009				-0.004
		0.05	-0.002	0.001	0.004				0.001
		0.08	-0.003	-0.006	0.004				-0.002
		0.1	0.014	-0.001	0.001				0.005
		0.2	0.003	0.008	-0.005				0.002
	Sample size	200	0.019	-0.013	-0.001				0.002
		600	0.001	0.007	-0.013				-0.002
		1000	-0.021	0.002	-0.015				-0.012
		2000	-0.01	-0.0	-0.008				-0.006
		4000	-0.01	-0.014	-0.008				-0.011
		8800	-0.008	-0.011	-0.01				-0.009

Table F.2: Estimated values of Ω_m using cosmological and observed redshifts calculated from simulated SNIa data with various maximum and minimum redshift cuts and for SNIa samples of different sizes. The parameters are estimated with the standard simulated data, with normalised observed redshifts and with exact distance modulus data.

Data	Cut	z or N	Redshift	Estimated Ω_m for each run						Ave	Ave - Fid
				1	2	3	4	5	6		
Standard SNIa data	Max redshift	0.05	cos	0.408	0.379	0.399	0.38	0.399	0.397	0.394	0.144
			obs	0.405	0.391	0.404	0.392	0.433	0.42	0.408	0.158
		0.08	cos	0.41	0.312	0.395	0.367	0.438	0.392	0.386	0.136
			obs	0.419	0.323	0.42	0.397	0.437	0.447	0.407	0.157
		0.1	cos	0.376	0.396	0.416	0.374	0.389	0.367	0.386	0.136
			obs	0.356	0.422	0.46	0.388	0.422	0.378	0.404	0.154
		0.2	cos	0.319	0.415	0.288	0.412	0.39	0.341	0.361	0.111
			obs	0.343	0.407	0.348	0.426	0.385	0.357	0.378	0.128
		0.3	cos	0.331	0.329	0.292	0.304	0.295	0.342	0.315	0.065
			obs	0.317	0.328	0.276	0.287	0.273	0.288	0.295	0.045
		0.4	cos	0.201	0.198	0.201	0.226	0.3	0.343	0.245	-0.005
			obs	0.177	0.187	0.173	0.25	0.228	0.281	0.216	-0.034
		0.5	cos	0.2	0.164	0.178	0.195	0.206	0.203	0.191	-0.059
			obs	0.171	0.157	0.162	0.149	0.163	0.2	0.167	-0.083
		0.6	cos	0.233	0.209	0.205	0.211	0.168	0.26	0.214	-0.036
			obs	0.209	0.2	0.181	0.204	0.172	0.199	0.194	-0.056
		0.7	cos	0.242	0.186	0.263	0.238	0.198	0.248	0.229	-0.021
			obs	0.225	0.162	0.251	0.217	0.184	0.237	0.213	-0.037
		0.8	cos	0.254	0.208	0.235	0.251	0.252	0.236	0.239	-0.011
			obs	0.246	0.189	0.219	0.24	0.242	0.219	0.226	-0.024

Standard SNIa data

Sample size	Min redshift										
		0.9									
200	cos	0.249	0.215	0.23	0.219	0.248	0.244	0.234	-0.016		
	obs	0.24	0.202	0.213	0.207	0.231	0.231	0.221	-0.029		
600	cos	0.264	0.246	0.243	0.24	0.282	0.249	0.254	0.004		
	obs	0.256	0.232	0.235	0.231	0.271	0.241	0.244	-0.006		
1000	cos	0.261	0.242	0.244	0.242	0.281	0.255	0.254	0.004		
	obs	0.257	0.235	0.226	0.237	0.273	0.237	0.244	-0.006		
2000	cos	0.263	0.242	0.24	0.241	0.279	0.249	0.252	0.002		
	obs	0.257	0.235	0.23	0.235	0.272	0.242	0.245	-0.005		
4000	cos	0.262	0.243	0.25	0.238	0.285	0.253	0.255	0.005		
	obs	0.262	0.241	0.252	0.238	0.285	0.253	0.255	0.005		
		0.0									
200	cos	0.261	0.242	0.244	0.242	0.281	0.255	0.254	0.004		
	obs	0.257	0.235	0.226	0.237	0.273	0.237	0.244	-0.006		
600	cos	0.263	0.242	0.24	0.241	0.279	0.249	0.252	0.002		
	obs	0.257	0.235	0.23	0.235	0.272	0.242	0.245	-0.005		
1000	cos	0.262	0.243	0.25	0.238	0.285	0.253	0.255	0.005		
	obs	0.262	0.241	0.252	0.238	0.285	0.253	0.255	0.005		
2000	cos	0.269	0.259	0.256	0.242	0.288	0.253	0.261	0.011		
	obs	0.267	0.254	0.254	0.241	0.275	0.248	0.257	0.007		
4000	cos	0.283	0.27	0.257	0.258	0.295	0.263	0.271	0.021		
	obs	0.288	0.278	0.27	0.254	0.296	0.267	0.276	0.026		
		0.1									
200	cos	0.294	0.273	0.26	0.255	0.302	0.266	0.275	0.025		
	obs	0.297	0.271	0.261	0.258	0.3	0.264	0.275	0.025		
600	cos	0.26	0.309	0.236	0.296	0.317	0.216	0.272	0.022		
	obs	0.253	0.306	0.233	0.297	0.324	0.24	0.276	0.026		
1000	cos	0.216	0.227	0.278	0.267	0.251	0.284	0.254	0.004		
	obs	0.22	0.219	0.271	0.295	0.258	0.275	0.256	0.006		
2000	cos	0.277	0.231	0.16	0.176	0.192	0.167	0.2	-0.05		
	obs	0.269	0.213	0.168	0.207	0.193	0.192	0.207	-0.043		
4000	cos	0.249	0.276	0.288	0.217	0.263	0.263	0.259	0.009		
	obs	0.243	0.268	0.28	0.227	0.23	0.254	0.25	0.0		
		0.2									
200	cos	0.266	0.232	0.253	0.266	0.28	0.272	0.262	0.012		
	obs	0.259	0.221	0.245	0.252	0.264	0.264	0.251	0.001		

Using normalised observed z

Max redshift											
8800	cos	0.264	0.246	0.243	0.24	0.282	0.249	0.254	0.004		
	obs	0.256	0.232	0.235	0.231	0.271	0.241	0.244	-0.006		
0.05	cos	0.408	0.379	0.399	0.38	0.399	0.397	0.394	0.144		
	obs	0.418	0.389	0.393	0.431	0.386	0.436	0.409	0.159		
0.08	cos	0.41	0.312	0.395	0.367	0.438	0.392	0.386	0.136		
	obs	0.367	0.316	0.447	0.369	0.419	0.411	0.388	0.138		
0.1	cos	0.376	0.396	0.416	0.374	0.389	0.367	0.386	0.136		
	obs	0.333	0.385	0.411	0.362	0.404	0.381	0.379	0.129		
0.2	cos	0.319	0.415	0.288	0.412	0.39	0.341	0.361	0.111		
	obs	0.39	0.413	0.32	0.389	0.379	0.334	0.371	0.121		
0.3	cos	0.331	0.329	0.292	0.304	0.295	0.342	0.315	0.065		
	obs	0.319	0.308	0.263	0.278	0.247	0.281	0.283	0.033		
0.4	cos	0.201	0.198	0.201	0.226	0.3	0.343	0.245	-0.005		
	obs	0.194	0.178	0.185	0.207	0.262	0.292	0.22	-0.03		
0.5	cos	0.2	0.164	0.178	0.195	0.206	0.203	0.191	-0.059		
	obs	0.169	0.149	0.153	0.187	0.181	0.181	0.17	-0.08		
0.6	cos	0.233	0.209	0.205	0.211	0.168	0.26	0.214	-0.036		
	obs	0.233	0.207	0.208	0.203	0.166	0.192	0.201	-0.049		
0.7	cos	0.242	0.186	0.263	0.238	0.198	0.248	0.229	-0.021		
	obs	0.231	0.181	0.257	0.224	0.192	0.234	0.22	-0.03		
0.8	cos	0.254	0.208	0.235	0.251	0.252	0.236	0.239	-0.011		
	obs	0.249	0.19	0.221	0.242	0.236	0.219	0.226	-0.024		
0.9	cos	0.249	0.215	0.23	0.219	0.248	0.244	0.234	-0.016		
	obs	0.24	0.203	0.213	0.212	0.24	0.229	0.223	-0.027		
1.0	cos	0.264	0.246	0.243	0.24	0.282	0.249	0.254	0.004		
	obs	0.258	0.236	0.232	0.233	0.272	0.243	0.246	-0.004		

Using normalised observed z

Min redshift	Sample size										
0.0	cos	0.261	0.242	0.244	0.242	0.281	0.255	0.254	0.004		
	obs	0.258	0.236	0.232	0.233	0.272	0.243	0.246	-0.004		
0.02	cos	0.263	0.242	0.24	0.241	0.279	0.249	0.252	0.002		
	obs	0.259	0.243	0.233	0.236	0.276	0.243	0.248	-0.002		
0.05	cos	0.262	0.243	0.25	0.238	0.285	0.253	0.255	0.005		
	obs	0.264	0.239	0.249	0.239	0.285	0.254	0.255	0.005		
0.08	cos	0.269	0.259	0.256	0.242	0.288	0.253	0.261	0.011		
	obs	0.268	0.257	0.257	0.245	0.285	0.247	0.26	0.01		
0.1	cos	0.283	0.27	0.257	0.258	0.295	0.263	0.271	0.021		
	obs	0.289	0.274	0.266	0.269	0.294	0.269	0.277	0.027		
0.2	cos	0.294	0.273	0.26	0.255	0.302	0.266	0.275	0.025		
	obs	0.293	0.273	0.26	0.254	0.298	0.27	0.275	0.025		
200	cos	0.26	0.309	0.236	0.296	0.317	0.216	0.272	0.022		
	obs	0.26	0.317	0.237	0.288	0.298	0.251	0.275	0.025		
600	cos	0.216	0.227	0.278	0.267	0.251	0.284	0.254	0.004		
	obs	0.223	0.218	0.278	0.273	0.244	0.266	0.251	0.001		
1000	cos	0.277	0.231	0.16	0.176	0.192	0.167	0.2	-0.05		
	obs	0.269	0.221	0.144	0.167	0.209	0.162	0.195	-0.055		
2000	cos	0.249	0.276	0.288	0.217	0.263	0.263	0.259	0.009		
	obs	0.243	0.268	0.277	0.208	0.241	0.259	0.249	-0.001		
4000	cos	0.266	0.232	0.253	0.266	0.28	0.272	0.262	0.012		
	obs	0.258	0.227	0.255	0.248	0.266	0.265	0.253	0.003		
8800	cos	0.264	0.246	0.243	0.24	0.282	0.249	0.254	0.004		
	obs	0.254	0.271	0.263	0.229	0.271	0.242	0.255	0.005		

Using exact distance modulus data

Max redshift								
0.05	cos	0.394	0.382	0.375		0.384	0.134	
	obs	0.474	0.399	0.408		0.427	0.177	
0.08	cos	0.366	0.387	0.411		0.388	0.138	
	obs	0.388	0.395	0.423		0.402	0.152	
0.1	cos	0.366	0.361	0.362		0.363	0.113	
	obs	0.387	0.389	0.373		0.383	0.133	
0.2	cos	0.353	0.336	0.368		0.353	0.103	
	obs	0.359	0.356	0.361		0.359	0.109	
0.3	cos	0.309	0.343	0.31		0.321	0.071	
	obs	0.303	0.292	0.29		0.295	0.045	
0.4	cos	0.28	0.284	0.289		0.284	0.034	
	obs	0.238	0.247	0.238		0.241	-0.009	
0.5	cos	0.263	0.256	0.265		0.261	0.011	
	obs	0.228	0.242	0.201		0.224	-0.026	
0.6	cos	0.241	0.242	0.246		0.243	-0.007	
	obs	0.223	0.22	0.218		0.22	-0.03	
0.7	cos	0.243	0.251	0.243		0.246	-0.004	
	obs	0.224	0.229	0.212		0.222	-0.028	
0.8	cos	0.243	0.241	0.243		0.242	-0.008	
	obs	0.232	0.234	0.225		0.23	-0.02	
0.9	cos	0.248	0.246	0.247		0.247	-0.003	
	obs	0.237	0.237	0.232		0.235	-0.015	
1.0	cos	0.248	0.248	0.248		0.248	-0.002	
	obs	0.239	0.239	0.238		0.239	-0.011	

Using exact distance modulus data

Min redshift	Sample size							
0.0	cos	0.251	0.246	0.249		0.249	-0.001	
	obs	0.241	0.237	0.236		0.238	-0.012	
0.02	cos	0.248	0.249	0.248		0.248	-0.002	
	obs	0.247	0.247	0.239		0.244	-0.006	
0.05	cos	0.25	0.248	0.248		0.249	-0.001	
	obs	0.248	0.249	0.252		0.25	-0.0	
0.08	cos	0.247	0.248	0.244		0.247	-0.003	
	obs	0.244	0.242	0.249		0.245	-0.005	
0.1	cos	0.244	0.248	0.249		0.247	-0.003	
	obs	0.257	0.246	0.251		0.252	0.002	
0.2	cos	0.246	0.237	0.243		0.242	-0.008	
	obs	0.249	0.245	0.238		0.244	-0.006	
200	cos	0.256	0.263	0.256		0.258	0.008	
	obs	0.275	0.25	0.255		0.26	0.01	
600	cos	0.245	0.235	0.247		0.243	-0.007	
	obs	0.246	0.242	0.233		0.241	-0.009	
1000	cos	0.25	0.234	0.24		0.241	-0.009	
	obs	0.229	0.235	0.224		0.23	-0.02	
2000	cos	0.244	0.24	0.245		0.243	-0.007	
	obs	0.234	0.24	0.238		0.237	-0.013	
4000	cos	0.243	0.253	0.246		0.247	-0.003	
	obs	0.232	0.238	0.238		0.236	-0.014	
8800	cos	0.248	0.247	0.247		0.247	-0.003	
	obs	0.24	0.237	0.238		0.238	-0.012	

Table F.3: Shifts in H_0 caused by correlated peculiar velocities calculated from simulated SNIa data with various maximum and minimum redshift cuts and for SNIa samples of different sizes. The shifts are calculated with the standard simulated data, with normalised observed redshifts and with exact distance modulus data.

Data	Cut	z or N	Shifts in H_0 for each run						Ave
			1	2	3	4	5	6	
Standard SNIa data	Max redshift	0.05	-0.966	-0.945	-1.011	-0.953	-0.842	-1.029	-0.958
		0.08	-0.63	-0.579	-0.948	-0.612	-0.527	-0.732	-0.671
		0.1	-0.408	-0.54	-0.74	-0.37	-0.31	-0.815	-0.531
		0.2	-0.492	-0.532	-0.597	-0.55	-0.47	-0.601	-0.54
		0.3	-0.331	-0.266	-0.42	-0.287	-0.328	-0.416	-0.341
		0.4	-0.244	-0.218	-0.311	-0.173	-0.305	-0.375	-0.271
		0.5	-0.222	-0.188	-0.228	-0.212	-0.198	-0.238	-0.215
		0.6	-0.251	-0.19	-0.252	-0.166	-0.154	-0.353	-0.228
		0.7	-0.213	-0.223	-0.299	-0.221	-0.22	-0.261	-0.239
		0.8	-0.203	-0.214	-0.257	-0.218	-0.21	-0.262	-0.227
		0.9	-0.23	-0.203	-0.274	-0.217	-0.232	-0.289	-0.241
		1.0	-0.233	-0.237	-0.224	-0.181	-0.205	-0.252	-0.222
	Min redshift	0.0	-0.176	-0.201	-0.306	-0.161	-0.212	-0.287	-0.224
		0.02	-0.195	-0.177	-0.211	-0.189	-0.22	-0.243	-0.206
		0.05	-0.043	-0.003	0.026	-0.045	-0.012	-0.02	-0.016
		0.08	-0.02	-0.067	-0.031	-0.004	-0.26	-0.097	-0.08
		0.1	0.324	0.311	0.348	0.058	0.193	0.069	0.217
		0.2	0.126	-0.053	-0.033	0.073	-0.307	-0.203	-0.066
	Sample size	200	-0.426	-0.292	0.033	0.151	-0.357	-0.103	-0.165
		600	0.139	-0.039	-0.39	0.27	-0.137	-0.402	-0.093
		1000	-0.33	-0.158	-0.027	0.028	0.095	-0.065	-0.076
		2000	-0.144	-0.303	-0.168	-0.07	-0.444	-0.218	-0.224
		4000	-0.163	-0.16	-0.223	-0.261	-0.327	-0.214	-0.225
		8800	-0.233	-0.237	-0.224	-0.181	-0.205	-0.252	-0.222
Using normalised observed z	Max redshift	0.05	-0.121	0.007	-0.068	0.024	-0.142	0.105	-0.032
		0.08	-0.169	-0.051	-0.33	-0.142	-0.153	-0.275	-0.187
		0.1	0.01	-0.053	-0.374	-0.025	-0.124	-0.23	-0.133
		0.2	-0.319	-0.394	-0.51	-0.401	-0.4	-0.517	-0.423
		0.3	-0.237	-0.152	-0.222	-0.218	-0.172	-0.29	-0.215
		0.4	-0.095	-0.11	-0.163	-0.103	-0.172	-0.237	-0.147
		0.5	-0.087	-0.076	-0.118	-0.077	-0.103	-0.128	-0.098
		0.6	-0.081	-0.121	-0.097	-0.067	-0.116	-0.268	-0.125
		0.7	-0.126	-0.115	-0.172	-0.132	-0.112	-0.178	-0.139
		0.8	-0.179	-0.181	-0.217	-0.196	-0.215	-0.24	-0.205

Using normalised observed z		0.9	-0.18	-0.153	-0.211	-0.159	-0.153	-0.239	-0.182
		1.0	-0.157	-0.135	-0.212	-0.129	-0.133	-0.156	-0.154
	Min redshift	0.0	-0.12	-0.121	-0.217	-0.142	-0.161	-0.202	-0.161
		0.02	-0.096	-0.04	-0.123	-0.12	-0.12	-0.16	-0.11
		0.05	0.03	0.012	0.039	0.0	0.041	0.027	0.025
		0.08	0.027	-0.01	0.064	0.063	-0.048	-0.046	0.008
		0.1	0.367	0.214	0.274	0.423	0.084	0.159	0.253
		0.2	-0.032	0.056	-0.036	-0.016	-0.125	0.055	-0.016
	Sample size	200	-0.047	0.017	0.166	0.457	-0.498	0.179	0.046
		600	0.041	-0.016	-0.202	0.096	-0.252	-0.263	-0.1
		1000	-0.205	-0.024	-0.122	-0.017	0.207	-0.006	-0.028
		2000	-0.06	-0.239	-0.24	-0.178	-0.261	-0.149	-0.188
		4000	-0.166	-0.032	-0.071	-0.282	-0.217	-0.195	-0.161
		8800	-0.29	0.031	-0.1	-0.127	-0.136	-0.167	-0.132
Using exact distance modulus data	Max redshift	0.05	-0.812	-0.864	-1.244				-0.973
		0.08	-0.529	-0.519	-1.004				-0.684
		0.1	-0.503	-0.513	-0.735				-0.584
		0.2	-0.517	-0.487	-0.628				-0.544
		0.3	-0.327	-0.35	-0.404				-0.36
		0.4	-0.272	-0.28	-0.354				-0.302
		0.5	-0.244	-0.247	-0.361				-0.284
		0.6	-0.198	-0.25	-0.287				-0.245
		0.7	-0.237	-0.233	-0.313				-0.261
		0.8	-0.202	-0.181	-0.29				-0.224
		0.9	-0.202	-0.213	-0.272				-0.229
		1.0	-0.202	-0.201	-0.257				-0.22
	Min redshift	0.0	-0.232	-0.213	-0.236				-0.227
		0.02	-0.138	-0.136	-0.216				-0.163
		0.05	-0.046	-0.002	0.006				-0.014
		0.08	-0.049	-0.141	0.048				-0.047
		0.1	0.349	0.023	0.082				0.151
		0.2	0.022	0.191	-0.098				0.039
	Sample size	200	0.046	-0.62	-0.119				-0.231
		600	0.097	0.037	-0.286				-0.051
		1000	-0.303	-0.04	-0.413				-0.252
		2000	-0.295	-0.117	-0.142				-0.185
		4000	-0.246	-0.257	-0.227				-0.244
		8800	-0.208	-0.21	-0.252				-0.223

Table F.4: Estimated values of H_0 using cosmological and observed redshifts calculated from simulated SNIa data with various maximum and minimum redshift cuts and for SNIa samples of different sizes. The parameters are estimated with the standard simulated data, with normalised observed redshifts and with exact distance modulus data.

Data	Cut	z or N	Redshift	Estimated H_0 for each run						Ave	Ave - Fid
				1	2	3	4	5	6		
Standard SNIa data	Max redshift	0.05	cos	72.55	72.664	71.758	72.507	72.073	72.145	72.283	-0.717
			obs	71.584	71.72	70.747	71.554	71.231	71.116	71.325	-1.675
		0.08	cos	72.532	73.246	72.064	72.784	71.938	72.064	72.438	-0.562
			obs	71.902	72.667	71.116	72.172	71.411	71.332	71.767	-1.233
		0.1	cos	72.887	72.44	71.981	72.496	72.21	72.693	72.451	-0.549
			obs	72.479	71.9	71.241	72.126	71.9	71.878	71.921	-1.079
		0.2	cos	72.919	72.328	72.6	72.346	72.612	72.819	72.604	-0.396
			obs	72.427	71.796	72.003	71.797	72.142	72.219	72.064	-0.936
		0.3	cos	72.762	72.547	72.618	72.66	72.942	72.833	72.727	-0.273
			obs	72.431	72.282	72.198	72.373	72.614	72.417	72.386	-0.614
		0.4	cos	72.911	72.739	72.716	72.714	73.002	72.77	72.809	-0.191
			obs	72.667	72.521	72.405	72.541	72.697	72.395	72.538	-0.462
		0.5	cos	72.938	72.748	72.639	72.747	72.931	72.689	72.782	-0.218
			obs	72.715	72.56	72.411	72.535	72.732	72.451	72.567	-0.433
		0.6	cos	72.933	72.733	72.637	72.705	72.898	72.8	72.784	-0.216
			obs	72.682	72.542	72.385	72.539	72.744	72.447	72.556	-0.444
		0.7	cos	72.939	72.714	72.776	72.754	72.924	72.759	72.811	-0.189
			obs	72.726	72.492	72.477	72.533	72.704	72.498	72.572	-0.428
		0.8	cos	72.967	72.731	72.659	72.777	73.038	72.721	72.815	-0.185
			obs	72.764	72.518	72.403	72.559	72.828	72.458	72.588	-0.412

Standard SNIa data

Min redshift		Sample size									
0.9	cos	72.94	72.733	72.647	72.681	73.019	72.783	72.801	-0.199		
	obs	72.71	72.53	72.373	72.464	72.787	72.495	72.56	-0.44		
1.0	cos	73.012	72.861	72.697	72.746	73.149	72.766	72.872	-0.128		
	obs	72.779	72.624	72.473	72.565	72.944	72.514	72.65	-0.35		
0.0	cos	72.974	72.847	72.703	72.759	73.177	72.812	72.879	-0.121		
	obs	72.798	72.647	72.397	72.598	72.965	72.525	72.655	-0.345		
0.02	cos	72.99	72.822	72.626	72.776	73.175	72.761	72.858	-0.142		
	obs	72.795	72.645	72.415	72.587	72.955	72.519	72.653	-0.347		
0.05	cos	72.943	72.797	72.815	72.705	73.27	72.78	72.885	-0.115		
	obs	72.9	72.794	72.841	72.66	73.258	72.76	72.869	-0.131		
0.08	cos	73.125	73.287	73.033	72.846	73.419	72.747	73.076	0.076		
	obs	73.105	73.22	73.002	72.842	73.159	72.65	72.996	-0.004		
0.1	cos	73.73	73.729	73.156	73.279	73.68	73.227	73.467	0.467		
	obs	74.054	74.04	73.504	73.336	73.873	73.296	73.684	0.684		
0.2	cos	74.631	73.841	73.342	73.131	74.247	73.525	73.786	0.786		
	obs	74.757	73.788	73.309	73.203	73.94	73.322	73.72	0.72		
200	cos	73.607	74.581	71.75	72.47	72.628	73.32	73.059	0.059		
	obs	73.181	74.29	71.783	72.621	72.272	73.216	72.894	-0.106		
600	cos	72.263	72.74	73.335	72.692	72.261	73.205	72.749	-0.251		
	obs	72.402	72.701	72.945	72.962	72.124	72.804	72.656	-0.344		
1000	cos	73.167	72.079	73.158	71.987	72.352	72.338	72.514	-0.486		
	obs	72.837	71.921	73.131	72.015	72.447	72.273	72.437	-0.563		
2000	cos	73.481	73.14	72.637	72.748	73.048	73.128	73.03	0.03		
	obs	73.338	72.836	72.468	72.678	72.604	72.91	72.806	-0.194		
4000	cos	72.972	72.773	72.771	72.933	73.06	72.808	72.886	-0.114		
	obs	72.809	72.613	72.548	72.672	72.733	72.594	72.662	-0.338		

Using normalised observed z

Max redshift

8800	cos	73.012	72.861	72.697	72.746	73.149	72.766	72.872	-0.128
	obs	72.779	72.624	72.473	72.565	72.944	72.514	72.65	-0.35
0.05	cos	72.55	72.664	71.758	72.507	72.073	72.145	72.283	-0.717
	obs	72.429	72.671	71.69	72.531	71.931	72.25	72.25	-0.75
0.08	cos	72.532	73.246	72.064	72.784	71.938	72.064	72.438	-0.562
	obs	72.363	73.195	71.734	72.643	71.785	71.789	72.251	-0.749
0.1	cos	72.887	72.44	71.981	72.496	72.21	72.693	72.451	-0.549
	obs	72.897	72.387	71.607	72.471	72.086	72.463	72.319	-0.681
0.2	cos	72.919	72.328	72.6	72.346	72.612	72.819	72.604	-0.396
	obs	72.599	71.934	72.091	71.946	72.212	72.302	72.181	-0.819
0.3	cos	72.762	72.547	72.618	72.66	72.942	72.833	72.727	-0.273
	obs	72.524	72.395	72.396	72.442	72.77	72.543	72.512	-0.488
0.4	cos	72.911	72.739	72.716	72.714	73.002	72.77	72.809	-0.191
	obs	72.816	72.629	72.553	72.611	72.83	72.533	72.662	-0.338
0.5	cos	72.938	72.748	72.639	72.747	72.931	72.689	72.782	-0.218
	obs	72.85	72.672	72.521	72.67	72.828	72.561	72.684	-0.316
0.6	cos	72.933	72.733	72.637	72.705	72.898	72.8	72.784	-0.216
	obs	72.852	72.611	72.54	72.638	72.782	72.532	72.659	-0.341
0.7	cos	72.939	72.714	72.776	72.754	72.924	72.759	72.811	-0.189
	obs	72.813	72.599	72.604	72.622	72.813	72.581	72.672	-0.328
0.8	cos	72.967	72.731	72.659	72.777	73.038	72.721	72.815	-0.185
	obs	72.788	72.55	72.442	72.581	72.822	72.481	72.611	-0.389
0.9	cos	72.94	72.733	72.647	72.681	73.019	72.783	72.801	-0.199
	obs	72.76	72.58	72.435	72.522	72.866	72.544	72.618	-0.382
1.0	cos	73.012	72.861	72.697	72.746	73.149	72.766	72.872	-0.128
	obs	72.855	72.726	72.486	72.617	73.016	72.61	72.718	-0.282

Using normalised observed z

Min redshift	Sample size										
0.0	cos	72.974	72.847	72.703	72.759	73.177	72.812	72.879	-0.121		
	obs	72.855	72.726	72.486	72.617	73.016	72.61	72.718	-0.282		
0.02	cos	72.99	72.822	72.626	72.776	73.175	72.761	72.858	-0.142		
	obs	72.894	72.782	72.503	72.656	73.055	72.601	72.749	-0.251		
0.05	cos	72.943	72.797	72.815	72.705	73.27	72.78	72.885	-0.115		
	obs	72.974	72.809	72.854	72.705	73.311	72.808	72.91	-0.09		
0.08	cos	73.125	73.287	73.033	72.846	73.419	72.747	73.076	0.076		
	obs	73.152	73.277	73.097	72.909	73.371	72.701	73.085	0.085		
0.1	cos	73.73	73.729	73.156	73.279	73.68	73.227	73.467	0.467		
	obs	74.097	73.943	73.43	73.702	73.764	73.386	73.72	0.72		
0.2	cos	74.631	73.841	73.342	73.131	74.247	73.525	73.786	0.786		
	obs	74.599	73.897	73.306	73.115	74.122	73.58	73.77	0.77		
	200	cos	73.607	74.581	71.75	72.47	72.628	73.32	73.059	0.059	
		obs	73.56	74.598	71.916	72.927	72.131	73.499	73.105	0.105	
	600	cos	72.263	72.74	73.335	72.692	72.261	73.205	72.749	-0.251	
		obs	72.304	72.724	73.132	72.788	72.008	72.942	72.65	-0.35	
	1000	cos	73.167	72.079	73.158	71.987	72.352	72.338	72.514	-0.486	
		obs	72.963	72.054	73.036	71.97	72.559	72.332	72.486	-0.514	
	2000	cos	73.481	73.14	72.637	72.748	73.048	73.128	73.03	0.03	
		obs	73.421	72.901	72.396	72.57	72.787	72.979	72.842	-0.158	
	4000	cos	72.972	72.773	72.771	72.933	73.06	72.808	72.886	-0.114	
		obs	72.805	72.741	72.7	72.652	72.843	72.612	72.725	-0.275	
	8800	cos	73.012	72.861	72.697	72.746	73.149	72.766	72.872	-0.128	
		obs	72.722	72.892	72.598	72.619	73.012	72.599	72.74	-0.26	

Using exact distance modulus data

Max redshift

0.05	cos	72.468	72.486	72.536		72.497	-0.503
	obs	71.656	71.622	71.292		71.524	-1.476
0.08	cos	72.583	72.576	72.68		72.613	-0.387
	obs	72.054	72.057	71.676		71.929	-1.071
0.1	cos	72.831	72.825	72.828		72.828	-0.172
	obs	72.328	72.312	72.093		72.244	-0.756
0.2	cos	72.987	73.019	73.013		73.006	0.006
	obs	72.471	72.532	72.384		72.462	-0.538
0.3	cos	73.087	73.14	73.076		73.101	0.101
	obs	72.76	72.79	72.672		72.741	-0.259
0.4	cos	73.067	73.085	73.077		73.076	0.076
	obs	72.796	72.805	72.723		72.775	-0.225
0.5	cos	73.041	73.047	73.042		73.043	0.043
	obs	72.797	72.8	72.68		72.759	-0.241
0.6	cos	72.985	72.989	72.996		72.99	-0.01
	obs	72.787	72.739	72.709		72.745	-0.255
0.7	cos	72.992	73.022	72.988		73.001	0.001
	obs	72.754	72.79	72.675		72.739	-0.261
0.8	cos	72.978	72.957	72.982		72.972	-0.028
	obs	72.776	72.775	72.692		72.748	-0.252
0.9	cos	72.985	72.984	72.984		72.984	-0.016
	obs	72.783	72.77	72.712		72.755	-0.245
1.0	cos	72.992	72.982	72.991		72.989	-0.011
	obs	72.791	72.781	72.734		72.768	-0.232

Using exact distance modulus data

Min redshift	Sample size							
0.0	cos	73.002	72.986	72.977		72.988	-0.012	
	obs	72.77	72.774	72.741		72.761	-0.239	
0.02	cos	72.973	72.998	72.981		72.984	-0.016	
	obs	72.835	72.862	72.765		72.821	-0.179	
0.05	cos	73.012	72.964	72.985		72.987	-0.013	
	obs	72.966	72.962	72.991		72.973	-0.027	
0.08	cos	72.965	73.021	72.947		72.978	-0.022	
	obs	72.916	72.881	72.996		72.931	-0.069	
0.1	cos	72.911	73.0	73.06		72.99	-0.01	
	obs	73.26	73.023	73.142		73.142	0.142	
0.2	cos	73.054	72.805	72.897		72.919	-0.081	
	obs	73.077	72.996	72.8		72.957	-0.043	
200	cos	72.991	73.187	73.13		73.103	0.103	
	obs	73.037	72.567	73.012		72.872	-0.128	
600	cos	72.977	72.972	73.06		73.003	0.003	
	obs	73.074	73.009	72.774		72.952	-0.048	
1000	cos	73.032	72.913	72.956		72.967	-0.033	
	obs	72.729	72.874	72.543		72.715	-0.285	
2000	cos	72.945	72.956	72.939		72.946	-0.054	
	obs	72.65	72.838	72.797		72.762	-0.238	
4000	cos	72.945	73.036	72.964		72.982	-0.019	
	obs	72.698	72.779	72.736		72.738	-0.262	
8800	cos	72.984	72.983	72.994		72.987	-0.013	
	obs	72.776	72.773	72.743		72.764	-0.236	

Bibliography

G. Aldering, G. Adam, P. Antilogus, P. Astier, R. Bacon, S. Bongard, C. Bonnaud, Y. Copin, D. Hardin, F. Henault, D. A. Howell, J.-P. Lemonnier, J.-M. Levy, S. C. Loken, P. E. Nugent, R. Pain, A. Pecontal, E. Pecontal, S. Perlmutter, R. M. Quimby, K. Schahmaneche, G. Smadja, and W. M. Wood-Vasey. Overview of the Nearby Supernova Factory. In J. A. Tyson & S. Wolff, editor, *Society of Photo-Optical Instrumentation Engineers (SPIE) Conference Series*, volume 4836 of *Society of Photo-Optical Instrumentation Engineers (SPIE) Conference Series*, pages 61–72, December 2002. doi: 10.1117/12.458107.

G. Bruzual and S. Charlot. Stellar population synthesis at the resolution of 2003. MNRAS, 344:1000–1028, October 2003. doi: 10.1046/j.1365-8711.2003.06897.x.

F. J. Castander. The Sloan Digital Sky Survey. Ap&SS, 263:91–94, June 1998. doi: 10.1023/A:1002196414003.

G. Chabrier. Galactic Stellar and Substellar Initial Mass Function. PASP, 115:763–795, July 2003. doi: 10.1086/376392.

C. Clarkson, B. Bassett, and T. H.-C. Lu. A General Test of the Copernican Principle. *Physical Review Letters*, 101(1):011301–+, July 2008. doi: 10.1103/PhysRevLett.101.011301.

M. Colless, G. Dalton, S. Maddox, W. Sutherland, P. Norberg, S. Cole, J. Bland-Hawthorn, T. Bridges, R. Cannon, C. Collins, W. Couch, N. Cross, K. Deeley, R. De Propris, S. P. Driver, G. Efstathiou, R. S. Ellis, C. S. Frenk, K. Glazebrook, C. Jackson, O. Lahav, I. Lewis, S. Lumsden, D. Madgwick, J. A. Peacock, B. A. Peterson, I. Price, M. Seaborne, and K. Taylor. The 2dF Galaxy Redshift Survey: spectra and redshifts. MNRAS, 328:1039–1063, December 2001. doi: 10.1046/j.1365-8711.2001.04902.x.

D. J. Croton, V. Springel, S. D. M. White, G. De Lucia, C. S. Frenk, L. Gao, A. Jenkins, G. Kauffmann, J. F. Navarro, and N. Yoshida. The many lives of active galactic nuclei: cooling flows, black holes and the luminosities and colours of galaxies. MNRAS, 365:11–28, January 2006. doi: 10.1111/j.1365-2966.2005.09675.x.

T. M Davis, L. Hui, J. A Frieman, T. Haugbølle, R. Kessler, B. Sinclair, J. Sollerman, B. Bassett, J. Marriner, E. Mörtsell, R. C Nichol, M. W Richmond, M. Sako, and D. P

Schneider. The effect of peculiar velocities on supernova cosmology. *ArXiv e-prints*, December 2010.

G. De Lucia and J. Blaizot. The hierarchical formation of the brightest cluster galaxies. MNRAS, 375:2–14, February 2007. doi: 10.1111/j.1365-2966.2006.11287.x.

G. De Lucia, G. Kauffmann, and S. D. M. White. Chemical enrichment of the intracluster and intergalactic medium in a hierarchical galaxy formation model. MNRAS, 349:1101–1116, April 2004. doi: 10.1111/j.1365-2966.2004.07584.x.

Joanna Dunkley, Martin Bucher, Pedro G Ferreira, Kavilan Moodley, and Constantinos Skordis. Fast and reliable mcmc for cosmological parameter estimation. *Power*, 000 (February):12, 2004. URL `http://arxiv.org/abs/astro-ph/0405462`.

J Durbin and G S Watson. Testing for serial correlation in least squares regression.i. *Biometrika*, 37(3):409–428, 1950a. URL `http://eprints.ucl.ac.uk/18408/`.

J Durbin and G S Watson. Testing for serial correlation in least squares regression. ii. *Biometrika*, 37(3-4):409–428, 1950b. URL `http://www.ncbi.nlm.nih.gov/pubmed/14848121`.

J Durbin and G S Watson. Testing for serial correlation in least squares regression iii. *Biometrika*, 58(1):1–19, 1971. URL `http://www.jstor.org/stable/2332326?origin=crossref`.

D. J. Eisenstein, H.-J. Seo, E. Sirko, and D. N. Spergel. Improving Cosmological Distance Measurements by Reconstruction of the Baryon Acoustic Peak. ApJ, 664:675–679, August 2007. doi: 10.1086/518712.

A. V. Filippenko. Optical Spectra of Supernovae. ARA&A, 35:309–355, 1997. doi: 10.1146/annurev.astro.35.1.309.

A. Goobar and B. Leibundgut. Supernova cosmology: legacy and future. *ArXiv e-prints*, February 2011.

C. Gordon, K. Land, and A. Slosar. Cosmological Constraints from Type Ia Supernovae Peculiar Velocity Measurements. *Physical Review Letters*, 99(8):081301–+, August 2007. doi: 10.1103/PhysRevLett.99.081301.

Q. Guo, S. White, M. Boylan-Kolchin, G. De Lucia, G. Kauffmann, G. Lemson, C. Li, V. Springel, and S. Weinmann. From dwarf spheroidals to cD galaxies: simulating the galaxy population in a ΛCDM cosmology. MNRAS, pages 164–+, February 2011. doi: 10.1111/j.1365-2966.2010.18114.x.

M. Hamuy, M. M. Phillips, N. B. Suntzeff, R. A. Schommer, J. Maza, and R. Aviles. The Hubble Diagram of the Calan/Tololo Type IA Supernovae and the Value of HO. AJ, 112: 2398–+, December 1996. doi: 10.1086/118191.

A. Heavens. Statistical techniques in cosmology. *ArXiv e-prints*, June 2009.

David W. Hogg. Distance measures in cosmology. *ArXiv e-prints*, December 2000.

G. Kauffmann and M. Haehnelt. A unified model for the evolution of galaxies and quasars. MNRAS, 311:576–588, January 2000. doi: 10.1046/j.1365-8711.2000.03077.x.

R. Kessler, A. C. Becker, D. Cinabro, J. Vanderplas, J. A. Frieman, J. Marriner, T. M. Davis, B. Dilday, J. Holtzman, S. W. Jha, H. Lampeitl, M. Sako, M. Smith, C. Zheng, R. C. Nichol, B. Bassett, R. Bender, D. L. Depoy, M. Doi, E. Elson, A. V. Filippenko, R. J. Foley, P. M. Garnavich, U. Hopp, Y. Ihara, W. Ketzeback, W. Kollatschny, K. Konishi, J. L. Marshall, R. J. McMillan, G. Miknaitis, T. Morokuma, E. Mörtsell, K. Pan, J. L. Prieto, M. W. Richmond, A. G. Riess, R. Romani, D. P. Schneider, J. Sollerman, N. Takanashi, K. Tokita, K. van der Heyden, J. C. Wheeler, N. Yasuda, and D. York. First-Year Sloan Digital Sky Survey-II Supernova Results: Hubble Diagram and Cosmological Parameters. ApJS, 185:32–84, November 2009. doi: 10.1088/0067-0049/185/1/32.

A. Kim. Stretch-parameterized light curves for high redshift sn ia studies. In *Supernova Explosions: Their Causes and Consequences [Conference], Institute of Theoretical Physics, Santa Barbara*. LBNL Report LBNL–4422E, 1997.

Jaiseung Kim. Integrated markov chain monte carlo (mcmc) analysis of primordial non-gaussianity (f_nl) in the recent cmb data. *Journal of Cosmology and Astroparticle Physics*, 2011(04):018–018, 2010. URL `http://arxiv.org/abs/1009.0981`.

M. G. Kitzbichler and S. D. M. White. The high-redshift galaxy population in hierarchical galaxy formation models. MNRAS, 376:2–12, March 2007. doi: 10.1111/j.1365-2966.2007.11458.x.

E. Komatsu, J. Dunkley, M. R. Nolta, C. L. Bennett, B. Gold, G. Hinshaw, N. Jarosik, D. Larson, M. Limon, L. Page, D. N. Spergel, M. Halpern, R. S. Hill, A. Kogut, S. S. Meyer, G. S. Tucker, J. L. Weiland, E. Wollack, and E. L. Wright. Five-Year Wilkinson Microwave Anisotropy Probe Observations: Cosmological Interpretation. ApJS, 180:330–376, February 2009. doi: 10.1088/0067-0049/180/2/330.

E. Komatsu, K. M. Smith, J. Dunkley, C. L. Bennett, B. Gold, G. Hinshaw, N. Jarosik, D. Larson, M. R. Nolta, L. Page, D. N. Spergel, M. Halpern, R. S. Hill, A. Kogut, M. Limon, S. S. Meyer, N. Odegard, G. S. Tucker, J. L. Weiland, E. Wollack, and E. L. Wright. Seven-year Wilkinson Microwave Anisotropy Probe (WMAP) Observations: Cosmological Interpretation. ApJS, 192:18–+, February 2011. doi: 10.1088/0067-0049/192/2/18.

M. Kowalski, D. Rubin, G. Aldering, R. J. Agostinho, A. Amadon, R. Amanullah, C. Balland, K. Barbary, G. Blanc, P. J. Challis, A. Conley, N. V. Connolly, R. Covarrubias, K. S. Dawson, S. E. Deustua, R. Ellis, S. Fabbro, V. Fadeyev, X. Fan, B. Farris, G. Folatelli,

B. L. Frye, G. Garavini, E. L. Gates, L. Germany, G. Goldhaber, B. Goldman, A. Goobar, D. E. Groom, J. Haissinski, D. Hardin, I. Hook, S. Kent, A. G. Kim, R. A. Knop, C. Lidman, E. V. Linder, J. Mendez, J. Meyers, G. J. Miller, M. Moniez, A. M. Mourão, H. Newberg, S. Nobili, P. E. Nugent, R. Pain, O. Perdereau, S. Perlmutter, M. M. Phillips, V. Prasad, R. Quimby, N. Regnault, J. Rich, E. P. Rubenstein, P. Ruiz-Lapuente, F. D. Santos, B. E. Schaefer, R. A. Schommer, R. C. Smith, A. M. Soderberg, A. L. Spadafora, L.-G. Strolger, M. Strovink, N. B. Suntzeff, N. Suzuki, R. C. Thomas, N. A. Walton, L. Wang, W. M. Wood-Vasey, and J. L. Yun. Improved Cosmological Constraints from New, Old, and Combined Supernova Data Sets. ApJ, 686:749–778, October 2008. doi: 10.1086/589937.

R. H. Kramer. Cosmolopy - a cosmology package for python. http://roban.github.com/CosmoloPy/, 2011.

A. V. Kravtsov, O. Y. Gnedin, and A. A. Klypin. The Tumultuous Lives of Galactic Dwarfs and the Missing Satellites Problem. ApJ, 609:482–497, July 2004. doi: 10.1086/421322.

B. Leibundgut. Supernovae and cosmology. *General Relativity and Gravitation*, 40:221–248, February 2008. doi: 10.1007/s10714-007-0545-9.

A. Lewis and S. Bridle. Cosmological parameters from CMB and other data: A Monte Carlo approach. Phys. Rev. D, 66(10):103511–+, November 2002. doi: 10.1103/PhysRevD.66.103511.

A. Lewis, A. Challinor, and A. Lasenby. Efficient Computation of Cosmic Microwave Background Anisotropies in Closed Friedmann-Robertson-Walker Models. ApJ, 538:473–476, August 2000. doi: 10.1086/309179.

F. Mannucci, M. Della Valle, N. Panagia, E. Cappellaro, G. Cresci, R. Maiolino, A. Petrosian, and M. Turatto. The supernova rate per unit mass. A&A, 433:807–814, April 2005. doi: 10.1051/0004-6361:20041411.

J. B. Oke and J. E. Gunn. Secondary standard stars for absolute spectrophotometry. ApJ, 266:713–717, March 1983. doi: 10.1086/160817.

John A. Peacock. *Cosmological Physics*. Cambridge University Press, 1999. ISBN 0-521-42270-1.

P.J.E. Peebles. *Principles of Physical Cosmology*. Princeton Series in Physics. Princeton University Press, 1993. ISBN 0-691-01933-9.

Will J Percival. Markov chain reconstruction of the 2df galaxy redshift survey real-space power spectrum. *Monthly Notices of the Royal Astronomical Society*, 356(3):1168–1176, 2005. URL `http://doi.wiley.com/10.1111/j.1365-2966.2011.18245.x`.

S. Perlmutter, G. Aldering, B. J. Boyle, P. G. Castro, W. J. Couch, S. Deustua, S. Fabbro, R. S. Ellis, A. V. Filippenko, A. Fruchter, G. Goldhaber, A. Goobar, D. E. Groom, I. M.

Hook, M. Irwin, A. G. Kim, M. Y. Kim, R. A. Knop, J. C. Lee, T. Matheson, R. G. McMahon, H. J. M. Newberg, C. Lidman, P. Nugent, N. J. Nunes, R. Pain, N. Panagia, C. R. Pennypacker, R. Quimby, P. Ruiz-Lapuente, B. Schaefer, N. Walton, and The Supernova Cosmology Project. Measurements of Omega and Lambda from 42 High-Redshift Supernovae. In J. Paul, T. Montmerle, & E. Aubourg, editor, *19th Texas Symposium on Relativistic Astrophysics and Cosmology*, December 1998.

M. M. Phillips. The absolute magnitudes of Type IA supernovae. ApJ, 413:L105–L108, August 1993. doi: 10.1086/186970.

C. Quercellini, L. Amendola, A. Balbi, P. Cabella, and M. Quartin. Real-time Cosmology. *ArXiv e-prints*, November 2010.

High Resolution, Forest Spectra, Jochen Weller, and Martin G Haehnelt. Wmap 7 constraints on oscillations in the primordial power spectrum. *Society*, 16(February):14, 2007. URL `http://arxiv.org/abs/1109.5264`.

A. G. Riess, A. V. Filippenko, P. Challis, A. Clocchiatti, A. Diercks, P. M. Garnavich, R. L. Gilliland, C. J. Hogan, S. Jha, R. P. Kirshner, B. Leibundgut, M. M. Phillips, D. Reiss, B. P. Schmidt, R. A. Schommer, R. C. Smith, J. Spyromilio, C. Stubbs, N. B. Suntzeff, and J. Tonry. Observational Evidence from Supernovae for an Accelerating Universe and a Cosmological Constant. AJ, 116:1009–1038, September 1998. doi: 10.1086/300499.

A. Slosar and M. Hobson. An improved Markov-chain Monte Carlo sampler for the estimation of cosmological parameters from CMB data. *ArXiv Astrophysics e-prints*, July 2003.

R. S. Somerville, J. R. Primack, and S. M. Faber. The nature of high-redshift galaxies. MNRAS, 320:504–528, February 2001. doi: 10.1046/j.1365-8711.2001.03975.x.

V. Springel. The cosmological simulation code GADGET-2. MNRAS, 364:1105–1134, December 2005. doi: 10.1111/j.1365-2966.2005.09655.x.

V. Springel, S. D. M. White, G. Tormen, and G. Kauffmann. Populating a cluster of galaxies - I. Results at [formmu2]z=0. MNRAS, 328:726–750, December 2001. doi: 10.1046/j.1365-8711.2001.04912.x.

V. Springel, S. D. M. White, A. Jenkins, C. S. Frenk, N. Yoshida, L. Gao, J. Navarro, R. Thacker, D. Croton, J. Helly, J. A. Peacock, S. Cole, P. Thomas, H. Couchman, A. Evrard, J. Colberg, and F. Pearce. Simulations of the formation, evolution and clustering of galaxies and quasars. Nature, 435:629–636, June 2005. doi: 10.1038/nature03597.

M. A. Strauss and J. A. Willick. The density and peculiar velocity fields of nearby galaxies. Phys. Rep., 261:271–431, 1995. doi: 10.1016/0370-1573(95)00013-7.

M. Sullivan and C. Balland. The Supernova Legacy Survey. *The Messenger*, 133:42–47, September 2008.

J. R. Thorstensen, G. A. Wegner, R. Hamwey, F. Boley, M. J. Geller, J. P. Huchra, M. J. Kurtz, and R. K. McMahan. Redshifts for a sample of fainter galaxies in the first CfA survey slice. AJ, 98:1143–1147, October 1989. doi: 10.1086/115203.

S. Weinberg. *Gravitation and Cosmology: Principles and Applications of the General Theory of Relativity*. July 1972.